Chemical Science

ROYAL SOCIETY OF CHEMISTRY

REVIEW

View Article Online
View Journal | View Issue

Cite this: *Chem. Sci.*, 2026, **17**, 6848

Nanotechnology engineering of polyanionic $Na_3V_2(PO_4)_2F_3$ cathodes toward high-performance sodium-ion batteries

Jiahao Chen,[a] Xingjie Wu,[b] Zhiyong Luo,[b] Xinxian Ren,[b] Junhao Chen,[b] Minjie Chen,[a] Chunliu Xu,*[a] Yao Xiao *[c] and Weiqing Yang *[a]

Polyanionic $Na_3V_2(PO_4)_2F_3$ (NVPF) cathodes enable a high operating voltage for sodium-ion batteries (SIBs) by virtue of the valence-electron decoupling properties from vanadium metal transition-metal redox centers and polyanionic groups. However, the low intrinsic conductivity and restricted ion diffusion kinetics have led to undesirable electrochemical performance, thereby limiting the further application of NVPF cathodes. The appropriate nanotechnologies can address the intrinsic deficiencies of materials and serve as a key strategy to break through performance bottlenecks. Herein, we summarize the recent progress made to improve the comprehensive performance of NVPF-based cathode materials from the perspective of nanoengineering, typically including nanoarchitecture, nanoscale surface modification and nanostructure tuning to clarify the structural properties, electrochemical behavior and their interplay. Moreover, the remaining challenges and future suggestions for the design of higher-performance NVPF cathodes towards practical SIBs are presented. The current review provides profound insights into the structure–performance relationship and valuable guidance to develop polyanionic NVPF cathodes for practical SIBs toward commercialization.

Received 26th December 2025
Accepted 26th February 2026

DOI: 10.1039/d5sc10141g

rsc.li/chemical-science

1 Introduction

Lithium-ion batteries (LIBs), the most commercially popular clean energy storage device today, have been widely used in electric vehicles and portable/mobile electronic devices.[1–9] Nevertheless, LIBs face resource and cost pressures, safety and low-temperature performance deficiencies, fast-charge technology bottlenecks and other challenges, which greatly limit the further development.[7–14] Meanwhile, this also provides the opportunity for the research and application of other clean energy storage devices. Sodium-ion batteries (SIBs), as a result of invention at the same time as LIBs, have better resources and economy, a more outstanding wide temperature range and rate performance, and higher safety and stability.[15–25] Therefore, SIBs possess significant research potential to make up for the deficiencies in the intrinsic performance of LIBs, or even to replace some of the application scenarios of LIBs. SIBs are the same as LIBs as "rocking chair" secondary batteries, with core components including an anode (hard or soft carbon), electrolyte (sodium hexafluorophosphate ($NaPF_6$) as the main solute), separator (the same as that of LIBs), current collector (aluminum foil for lower cost), and cathode (Fig. 1).[16,26–35] It needs to be noted that due to the "barrel law", the cathode becomes the "short board" in the release of the performance of SIBs. The reason is that the cathode offers a lower specific capacity, and a larger percentage of mass fraction compared to the anode, which dominantly determines the key attributes of SIBs such as energy density, operating life and rate performance.[36] Also, the cathode provides more space than the anode to increase the operating voltage of the SIBs.[37,38] In addition, the cathode occupies the largest cost share among all the component parts of SIBs. Consequently, research on the cathode strongly influences the development trend of SIBs.

In the context of nanostructured and intercalated electrochemistry-based studies of SIBs, researchers are actively exploring various cathode materials for SIBs, including layered metal oxides (LMOs), Prussian blue analogs (PBAs), and polyanion compounds (PACs) (Fig. 2a).[37,39–42] Drawing inspiration from the successive development of cathode materials such as $LiCoO_2$, $LiNi_xCo_yMn_zO_2$, and $LiNi_xCo_yAl_zO_2$ in commercial LIBs, researchers hold equally high hopes for LMO cathode materials in SIBs. As one of the most promising industrialization cathodes, LMOs can be classified into P-type (trigonal prism coordination) and O-type (octahedral coordination) structures based on two crystallographic criteria, namely, the coordination geometry of sodium ions and the number of stacked layers of the crystal cell.[17]

[a]*Key Laboratory of Advanced Technologies of Materials (Ministry of Education), School of Materials Science and Engineering and Research Institute of Frontier Science, Southwest Jiaotong University, Chengdu, 610031, China. E-mail: chunliuxu@swjtu.edu.cn; wqyang@swjtu.edu.cn*

[b]*School of Chemistry, Southwest Jiaotong University, Chengdu, 610031, China*

[c]*College of Chemistry and Materials Engineering, Wenzhou University, Wenzhou, Zhejiang 325035, P. R. China. E-mail: xiaoyao@wzu.edu.cn*

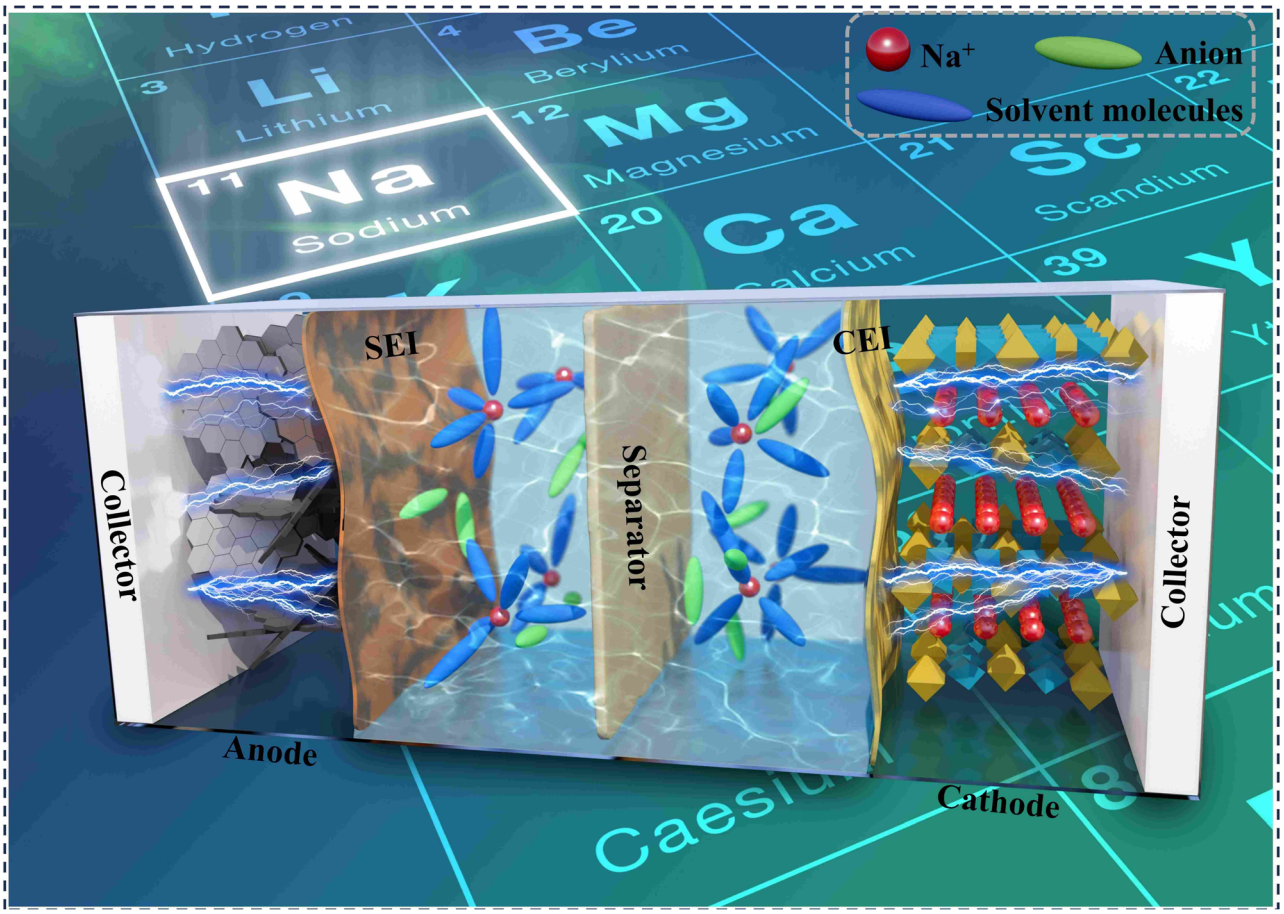

Fig. 1 Schematic diagram of the structure of a "rocking chair type" sodium-ion battery.

Specifically, the transition metal layer consists of transition metal octahedra connected to each other in a side-sharing manner, with sodium ions stored in the interlayer gap. The most extensively studied LMOs are primarily P2-type and O3-type, exhibiting ABBA and ABCABC arrangements respectively. Simultaneously, the P3-type and O2-type cathode materials feature ABBCCA and ABAC arrangements. LMO cathode materials typically provide the largest specific capacity (150–220 mAh g^{-1}) of the three. However, LMOs materials suffer from poor air stability and irreversible degradation of the lattice structure upon Na^+ extraction/insertion. Specifically, while the O3-type cathode possesses higher sodium ion content compared to the P2-type cathode material (resulting in higher initial charge–discharge capacity), sodium ions must traverse a small tetrahedron between two adjacent octahedra during migration. Consequently, the diffusion energy barrier is larger, leading to slower sodium ion transport kinetics. Furthermore, the transition of sodium ions through the narrow sodium layer more easily triggers complex phase transformation processes, leading to serious degradation of the LMO cathode structure. As a consequence, the specific capacity of the cathode material decreases rapidly during charge/discharge cycles, and the cycle life is restricted.

Furthermore, the PBAs which were originally used as dyes and had the lowest synthetic costs represent a class of polymers consisting of transition metals and cyanide-bridged ligands.[50,51] The chemical formula for PBAs can be represented as $Na_xM_A[-M_B(CN)_6]$, where M_A denotes 3d transition metals such as Fe, Co, and Ni (coordinating with N), and M_B predominantly consists of Fe and Mn (coordinating with C). The sodium content ranges from 0 to 2. Generally, a sodium content below 1 is considered Prussian blue, while a sodium content above 1 is considered Prussian white. Due to the three-dimensional open nano-framework possessed by the cyanide-based bridged cubic lattice in its core structure, the PBAs possesses abundant topological ion transport channels and are capable of high rate charging and discharging. Moreover, the transition metal redox pairs in the material undergo multi-electron reactions, enabling the reversible insertion and extraction of multiple sodium ions, thus contributing significantly to its high capacity. Meanwhile, the flexible tunability of the structure and components brings interesting material design ideas, such as high-entropy materials, which help improve the electrochemical performance of the cathode materials. Unfortunately, PBAs inevitably introduce crystalline water and vacancies during synthesis and operation, making it difficult for the cathode structure to achieve an ideal state. Crystalline water and vacancies also occupy sodium ion sites, hindering sodium ion transport, and may even induce electrolyte decomposition, ultimately leading to electrode

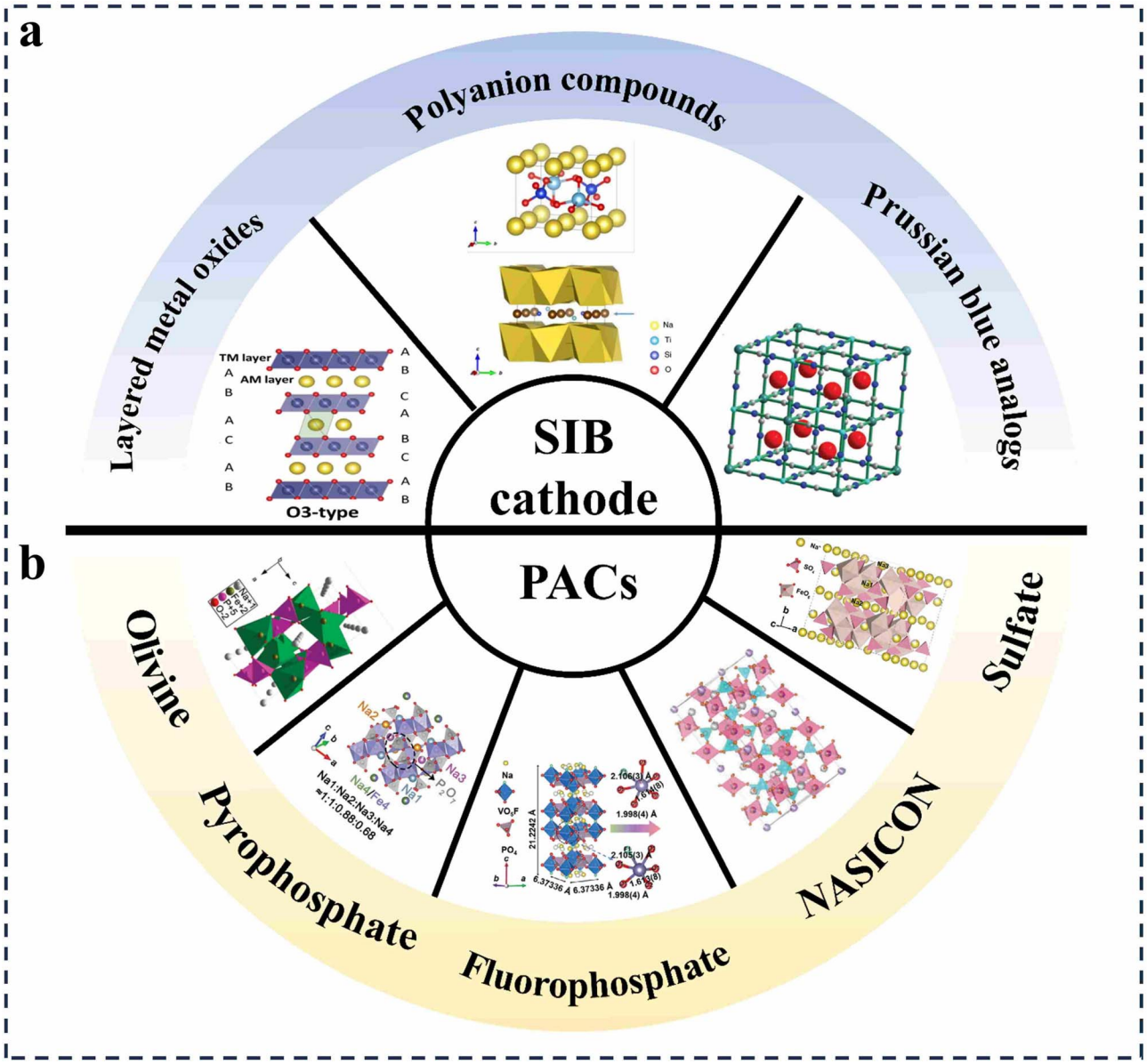

Fig. 2 (a) Classification of cathode materials for sodium-ion batteries.[39,40,43] Copyright 2025, Wiley-VCH. Copyright 2018, Wiley-VCH. Copyright 2021, Springer Nature. (b) Classification of poly-anion materials.[44–49] Copyright 2024, Wiley-VCH. Copyright 2024, Wiley-VCH. Copyright 2025, Wiley-VCH. Copyright 2024, KeAi Publishing Ltd. Copyright 2025, Wiley-VCH. Copyright 2010, American Chemical Society. Copyright 2024, Wiley-VCH.

structural collapse. Consequently, the electrochemical properties of PBA cathode materials, such as coulombic efficiency and cycling stability, undergo degradation. The toxicity potential associated with the thermal decomposition of cyanide has also become a necessary consideration for researchers.

PACs represent a class of substances formed by strong covalent bonding of polyanionic groups with transition metal ions.[52,53] Benefiting from the three-dimensional rigid skeleton resulting from the stable covalent bonding, PACs have the highest structural stability and intrinsic safety of the three. Typically, researchers categorize PACs into olivine, pyrophosphate, Na superionic conductor (NASICON), sulfate, and fluorophosphate type structures based on the crystal structure (Fig. 2b).[44–49] The achievements in $LiFePO_4$ cathode materials for LIBs have inspired researchers to focus extensively on $NaFePO_4$ materials with similar structures. The same olivine structure features a one-dimensional unidirectional ion transport channel along the [010] direction, formed by the shared corners between FeO_6 hexahedra and PO_4 tetrahedra. It belongs to the orthorhombic crystal system with the space group *Pmmb*. During the preparation of olivine-type $NaFePO_4$, the formation of the Maricite phase structure (electrochemically inert) occurs at temperatures between 500 and 600 °C, which is undesirable. Researchers therefore typically employ cation (Li/Na) exchange methods to indirectly synthesize olivine structures. Pyrophosphate-type structures are formed by $[P_2O_7]^{4-}$ polymers

linked to transition metal octahedra, creating two-dimensional or three-dimensional nanoframeworks. They primarily include tetragonal, triclinic, and monoclinic phases. Pyrophosphate cathodes achieve outstanding electrochemical performance due to their rich crystal structures, high physicochemical stability, and large ion channel dimensions. However, their relatively large molecular weight yields lower reversible specific capacity, limiting their potential for applied research. A NASICON structure consists of transition metal octahedra connected with $[PO_4]$ tetrahedra co-vertices, which endowed the cathode with high ionic diffusion rates and structural framework stability. The widely studied $Na_3V_2(PO_4)_3$ (NVP) material exhibits an operating voltage of 3.4 V and a theoretical capacity of 117 mAh g^{-1}. Following further modification through techniques such as nanotechnology engineering, its electrochemical performance has been significantly enhanced. The sulfate structure consists of FeO_6 octahedra connected with $[SO_4]$ tetrahedra co-vertices and forms a three-dimensional nano-framework under the strong SO_4^{2-} induced effect. Compared to other polyionic anion groups, SO_4^{2-} exhibits greater electronegativity, making it highly promising for high-voltage cathode design. Yet the poor air and water stability of sulfate cathodes limits their performance potential, presenting a challenge that researchers are eager to overcome. The fluorophosphate structure consists of $[V_2O_8F_3]$ double octahedra connected with $[PO_4]$ tetrahedra to form layered nano-tetragonal channels. In parallel, the synergistic reaction of multiple redox centers (*e.g.*, $V^{3+}/V^{4+}/V^{5+}$) buffers the localized stress of the nanolattice framework, which along with the strong covalent bonding maintains the stability of the crystal structure backbone. Furthermore, the multi-electron reactions inherent to the fluorophosphate structure effectively broaden the voltage platform of the cathode material. Consequently, the synergistic interplay of these properties endows fluorophosphate-based cathodes with enhanced rate performance, prolonged cycle life, and improved safety stability. Despite these favorable attributes, PACs still face inherent drawbacks, including poor electronic conductivity, limited specific capacity, and high cost in certain systems, which collectively hinder their practical implementation.

This paper reviews the progress of nanoengineering research on $Na_3V_2(PO_4)_2F_3$ (NVPF), and summarizes the multifaceted benefits of the modification means, especially from a nanoscale microscopic point of view of the analysis. Initially, we have summarized the basic properties (including the crystal structure, synthesis process, *etc.*) of the NVPF structure. Besides, the shortcomings and challenges of NVPF materials, especially the comprehensive nanoscale effects, are discussed in depth in light of the results from the investigation. To address the aforementioned prevalent challenges, the review offers a comprehensive categorization and progress of nano-engineered modification strategies. Finally, the future development prospects of NVPF materials are summarized, and an outlook for their further application is provided. This review will provide guidance for the nanoengineering design of NVPF materials and practical methods for the nanoengineering modification of NVPF cathode materials.

2 Overview of NVPF cathode materials

2.1 Structure and characteristics of NVPF

NVPF, the representative fluorophosphate structure cathode in SIBs, has a 3D nano-skeleton. The synthesis of a series of compounds adopting the $Na_3M_2(PO_4)_2F_3$ ($M = V^{3+}$, Ga^{3+}, Cr^{3+}, Al^{3+}, Fe^{3+}) structure was reported by Meins *et al.* for the first time by solid-phase or hydrothermal methods in 1999, and their crystal structures were systematically characterized.[54] The results show that NVPF has an orthorhombic crystal structure and belongs to the *Amam* space group. In simple terms, the crystal structure of NVPF corresponds to the replacement of one PO_4^{3-} in NVP with three F^-. The V_2O_{10} double octahedral unit in NVP crystals is replaced in NVPF by a $V_2O_8F_3$ double octahedral unit. This double octahedral unit connected by F atoms is alternately bridged with PO_4 tetrahedral units to form a stable nano-open structure in a corner-to-corner mode (Fig. 3a).[55] Additionally, recent studies indicate that the NVPF crystal structure contains three distinct sodium sites, which are arranged around the vanadium atom centers in a circular distribution.[56] The three distinct sodium sites denoted as Na(1) (4c) and Na(2) (8f), both form capped trigonal prisms oriented along the [010] and [100] directions relative to the bioctahedral center, along with Na(3) (8f) sites—smaller trigonal prisms aligned with the [110] direction. Each ring accommodates eight sodium sites, with Na(2) and Na(3) exhibiting partial occupancies of approximately 70% and 30%, respectively, due to their close proximity. This occupancy distribution reflects the greater stability of the larger Na(1) and Na(2) sites relative to the Na(3) site (Fig. 3b).

In addition, to deeply investigate the migration paths of Na^+ in the NVPF nanocrystal structure, Song *et al.* performed first-principles calculations based on the density functional theory (DFT) method.[57] As shown in Fig. 3c, the migration paths in the *x*, *y*, *z* directions were set, and the migration activation energy was calculated. Based on the analysis of the computational results, it is concluded that transport along the Na^+ channel consisting of two $[V_2O_8F_3]$ double octahedra and $[PO_4]$ tetrahedra (direction *y*) yields the lowest migratory activation energy, showing the most probable mode of Na^+ transport in NVPF nanocrystals. Analogously, Lin *et al.* also predicted three representative diffusion paths for Na^+ in NVPF nanostructures based on theoretical calculations (Fig. 3d).[58] Furthermore, the results also predicted the Na^+ diffusion paths between neighboring nanolattice layers.

NVPF nanocrystalline materials are also attractive because of their voltage tunability, which makes it possible to pursue cathode materials with higher energy densities. The intrinsic relationship between the energy density (E_d) and the intrinsic properties of the cathode material could be defined as follows.

$$E_d = C_s \times V = \frac{n \times F}{3.6 \times M_w} \times V = 26\,800 \times \frac{n}{M_w} \times V \quad (1)$$

Here, V is the average operating voltage (*vs.* Na^+/Na), M_w is the molecular weight (g mol^{-1}), n is the number of transferred

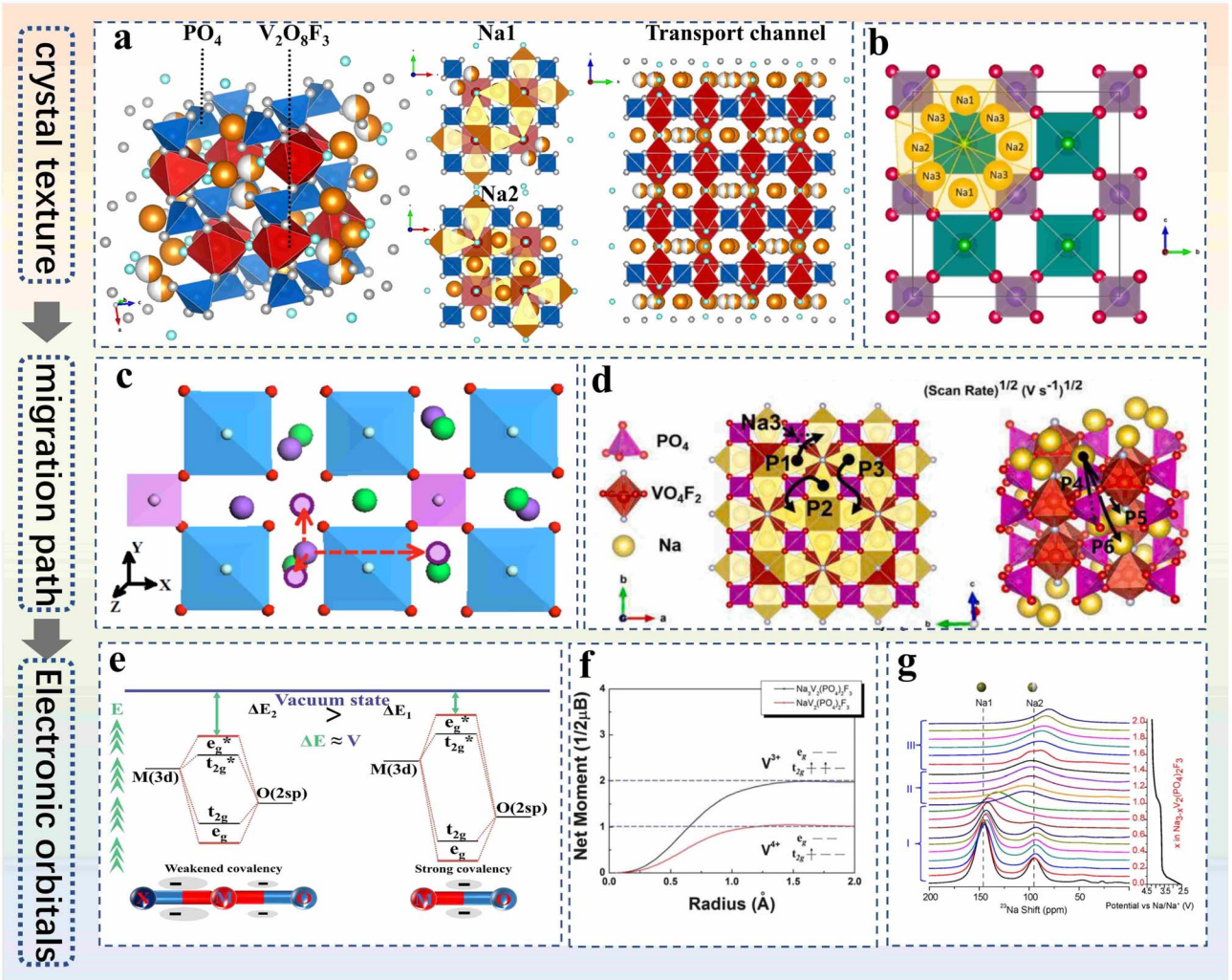

Fig. 3 (a) Schematic diagram of the NVPF crystal structure. (b) Arrangement of Na ions in the *ab*-plane of NVPF showing the presence of a ring-like configuration.[56] Copyright 2025, Royal Society of Chemistry. (c) The migration path of sodium ions.[57] Copyright 2014, American Chemical Society. (d) Different migration paths of Na^+ in the NVPF crystal structures.[58] Copyright 2023, Elsevier. (e) Schematic diagram of the reduction–oxidation potential of the material. (f) Schematic energy levels and occupied electrons of the 3d bands of vanadium ions of V^{3+} and V^{4+} are presented.[55] Copyright 2012, Royal Society of Chemistry. (g) *Ex situ* ^{23}Na NMR spectra of $Na_3V_2(PO_4)_2F_3$ electrodes at different states of charge.[59] Copyright 2014, American Chemical Society.

electrons, F is the Faraday constant, and C_s is the specific capacitance (mAh g^{-1}). The combination of high operating potential and multi-electron reactions thus underpins the enhanced performance of the cathode material. According to molecular orbital theory, covalent M–O interactions in NVPF nanomaterials induce energy level splitting, generating bonding (e_g and t_{2g}) and antibonding (e_{g^*} and t_{2g^*}) orbitals (Fig. 3e).[60,61] Moreover, the energy gap (ΔE) from the antibonding orbitals to the vacuum level scales proportionally with the redox potential of the material. Typically, the enhancement of M–O bond covalency leads to a more pronounced energy separation between these orbitals, which in turn leads to preferential electron occupation in the low-energy bonding orbitals. In contrast, the introduction of heteroatom X with high electronegativity weakens the M–O covalent bond by strengthening the M–O–X bond, which increases ΔE ultimately increasing the electrode redox potential. This phenomenon is known as the well-known induction effect of polyanionic compounds.

Thus, the presence of fluoride ions in NVPF nanomaterials elevates the working potential of NVPF. Since the electronegativity of fluorine (4.0) is higher than that of oxygen (3.44), when F^- substitutes O^{2-} in PO_4^{3-} to form a $[VO_5F]$ octahedron, the strong electron-absorbing capacity of F^- shifts the electron-cloud density of the V–O bond toward the F. Ultimately, it leads to a decrease in the electron cloud density around the vanadium atom, effectively increasing the energy level of the V^{3+}/V^{4+} redox pair.[62] In addition, the enhancement of the V–F bond, which has a higher percentage of ionic properties in NVPF, weakens the electron shielding effect of V^{3+}. This makes it easier for V^{3+} to oxidize to a higher valence state (V^{4+}/V^{5+}), that enhances the working potential of NVPF. Subsequently, after conducting relevant electrochemical performance tests, the

researchers reported NVPF with 3 pairs of distinct charging and discharging platforms (4.2/4.1 V, 3.7/3.6 V and 3.4/3.3 V). For the NVPF structure, only two Na^+ are involved in the charge/discharge process, while the third Na^+ in the nanostructure is electrochemically inert. If the electrochemical activity of the third Na^+ is activated, the new disordered "NVPF" phase will be formed.[63] Given the higher activity of Na2 compared to Na1, the charging/discharging plateaus at 3.7/3.6 V and 3.4/3.3 V correspond to a two-step Na^+ extraction process involving Na2, whereas the plateau at 4.2/4.1 V corresponds to a single-step extraction process involving Na1. Two redox potentials at 3.6 V and 4.2 V (*vs.* Na^+/Na) were identified, corresponding to the V^{3+}/V^{4+} redox couple and associated with a two-phase structural evolution. Moreover, the measured net spin moment provides additional evidence that the electrochemical activity of $Na_xV_2(PO_4)_2F_3$ (x is between 1 and 3) originates from the V^{3+}/V^{4+} redox process (Fig. 3f).[55] Hence, the nanostructure evolution of NVPF and the extraction/insertion process of sodium ions are described by using the chemical reaction equation.[64]

$$Na_3V_2^{3+}(PO_4)_2F_3 \leftrightarrow Na_2V^{3+}V^{4+}(PO_4)_2F_3 + Na^+ + e^- \quad (2)$$

$$Na_2V^{3+}V^{4+}(PO_4)_2F_3 \leftrightarrow NaV_2^{4+}(PO_4)_2F_3 + Na^+ + e^- \quad (3)$$

Besides, researchers further probed the local structural environment, dynamics, and electronic structure of the NVPF cathode using characterization techniques such as solid-state nuclear magnetic resonance (ssNMR). This provided insights into the extraction mechanism of Na in NVPF during electrode charging and discharging. Fig. 3g shows the ^{23}Na NMR spectrum of the NVPF material under different charge–discharge conditions.[59] High-resolution ^{23}Na and ^{31}P ssNMR spectroscopy, complemented by relaxation time measurements, enables the distinction of different Na and P sites. These techniques reveal the nonpreferential extraction of Na^+ from both the Na1 and Na2 sites, at least during the initial charging stage. As the population of Na vacancies increases, an increasingly fast Na1–Na2 two-site exchange motion is observed. Concurrently, electronic structural changes occur within the $V_2O_8F_3$ dimers that constitute the NASICON framework. The results provide insight into the evolution of the electrochemical profile and the underlying reasons for the good electrochemical performance of the $Na_3V_2(PO_4)_2F_3$ electrode. At the onset of Stage I, from $x =$ 0 to 0.6, Na1 and Na2 are removed at a ratio consistent with their relative occupancy in the structure, indicating minimal site preference for Na removal during this phase. This contradicts earlier reports suggesting that Na2 is less stable and is removed from the structure first.[65,66] The rate of Na^+ motion progressively accelerates with increasing Na extraction. When a total of 0.9 Na is removed (in Stage Ib), the two distinct Na1 and Na2 sites coalesce, corresponding to a Na1–Na2 two-site exchange rate of ~4.6 kHz. The electrochemical behavior in late Stage I ($x = 0.6$–1.0) differs markedly from that in early Stage I ($x = 0$–0.6). The later stage is characterized by a steeper potential increase, the occurrence of Na site coalescence, a more pronounced increase in T_1, and a noticeable jump in the ^{23}Na shift between 0.9 and 1.0 of x. The rapid reduction in intensity observed in other *in situ* ^{23}Na spectra during this stage is largely attributable to line broadening induced by enhanced Na^+ motion. The structural change in late Stage I ($x = 0.6$–1.0) may therefore originate from two intimately connected drivers. First, the high mobility of Na^+ between Na1 and Na2 sites helps to alleviate local framework distortions. Second, an associated structural distortion of the VO_4F_2 units presumably changes the relative t_{2g} orbital energies, leading to the preferential removal of electron density from a different orbital during this stage. Stage II resembles Stage I in several aspects. Notably, the Na hyperfine shift remains largely unaffected upon electron removal, indicating that the electrons are likely being extracted from the same orbital channels (tentatively the d_{xz}/d_{yz} orbitals) as in early Stage I. Stage III is marked by a splitting in the *ex situ* ^{23}Na resonances at $x = 1.5$, indicating two distinct local environments, one richer in V^{3+} (average oxidation state: $\sim V^{3.75+}$). Vanadium oxidation is reflected in progressively decreasing ^{23}Na shifts and increasing relaxation times. This electronic structure evolution coincides with a reduction in Na^+ mobility, as further indicated by the decrease in Na^+ diffusivity extracted from galvanostatic intermittent titration technique (GITT) data.

2.2 Synthesis methods of NVPF

Based on previous studies, the selection of the synthesis method and the control of the synthesis conditions are crucial for modulating the nanostructures of the electrode materials. Regarding NVPF, the typical synthesis methods are mainly divided into four types: including the solid-phase method,[67–69] sol–gel method,[70–74] hydrothermal/solvent-thermal route,[75–78] and others (spray drying strategy and electrospinning, *etc.*).[79–81]

The solid-phase method is a common method for synthesizing NVPF materials, which has a simple operation process for preparing electrode materials and a relatively low production cost. Solid-phase synthesis of NVPF typically employs sodium sources (*e.g.*, Na_2CO_3 and NaF), vanadium sources (*e.g.*, NH_4VO_3 and V_2O_5), phosphorus sources (*e.g.*, $NH_4H_2PO_4$), and fluorine sources (*e.g.*, NaF and NH_4F) as raw materials. After mechanical mixing, the mixture undergoes high-temperature sintering in an inert atmosphere, enabling nucleation and crystal growth through solid-phase diffusion of the reactants. The basic process flow for NVPF solid-phase synthesis includes raw material weighing and mixing, pre-sintering treatment, high-temperature sintering, and post-treatment. Basically, high-purity NVPF could be prepared directly by a solid-phase reaction. Meanwhile, nanoscale raw materials and higher calcination reaction temperatures are available to improve the product purity and synthetic preparation efficiency. Although the solid-phase method has gained wide acceptance in the synthesis of NVPFs, the shortcomings of the method are obvious. During high-temperature calcination, the particle size of NVPF nanomaterials increases, accompanied by a decrease in component homogeneity, which is detrimental to the electrochemical properties of NVPF. Consequently, the researchers attempted to optimize the solid-phase synthesis strategy and worked on obtaining NVPF with an ideal particle size distribution and homogeneous composition.

The sol–gel method is a low-temperature synthetic route that does not require further annealing treatment compared to the high-temperature synthesis conditions of the solid-phase method. Meanwhile, compared with the solid-phase method, the prepared nanomaterials have uniform particle size and component distribution. Specifically, the raw materials are usually dissolved and mixed in solutions. Citric acid is also added as a chelating agent, so that different transition metal ions are fully mixed with the carbon source to realize *in situ* carbon encapsulation synthesis. Furthermore, the gases generated from the thermal decomposition of citric acid promote the formation of porous structures, which ultimately significantly improves the electrochemical kinetics of the electrode materials. The core advantage of the sol–gel method lies in achieving atomic-level dispersion of precursors in the liquid phase, enabling high reactivity and uniformity. The lower reaction temperature also effectively minimizes fluorine volatilization, maintaining precise stoichiometric ratios. The ease of achieving *in situ* carbon coating and elemental doping is another significant advantage that should not be overlooked. The limitation of the sol–gel method is that it is not easy to achieve precise control of the morphology and structure of the sample. The manufacturing process is relatively complex and time-consuming. The reaction consumes large amounts of organic solvents, water, and energy, resulting in limited production capacity while potentially releasing harmful gases into the atmosphere.

Unlike the previous two, the solvent-thermal/hydrothermal method is a common and effective strategy capable of precisely controlling the morphology of NVPF. At normal temperature and pressure, the method allows for synthesis processes that cannot be accomplished under conventional conditions, increasing the reaction rate and yielding specific structures. To be specific, by adjusting the parameters during the reaction process, NVPF cathodes with various morphologies such as nanorods, nanocubes, and hollow microspheres could be obtained. Moreover, under autogenous pressure generated at reaction temperature, the products exhibit high crystallinity and purity. It also facilitates *in situ* composite formation with carbon materials, enabling superior electrochemical performance. It is noted that in liquid systems, the solvent type, feedstock concentration, surfactant type and pH are critical for the controlled preparation of the morphology of the synthesized nanocrystalline materials. Typically, the hydrothermal/solvothermal method uses only oxide powders as feedstock. Furthermore, although the method has a short drying time, and high water evaporation and heat transfer rates, it exhibits poor overall thermal efficiency and mediocre synthesis efficiency.

Spray drying and electrospinning methods, as auxiliary technologies for synthesizing NVPF cathode materials, are usually combined with solid-phase methods to incorporate new advantages into the traditional preparation methods. Spray drying is a continuous process with potential for large-scale preparation. The solvent is dispersed into micro-sized droplets by means of an atomizer, which further come into contact with hot gas and instantly evaporated to form NVPF material nanoparticles. The advantages of the spray-drying method lie in the homogeneity of the prepared nanoparticles and the flexibility of structural design, as well as the ability of continuous mass production. However, attention still needs to be paid to the loss of the fluorine element and the control of impurities during the preparation process.

Electrospinning is a classic technique for synthesizing one-dimensional nanostructured self-supporting electrode materials. Through the processes of electrostatic spinning and carbonization, the polymer solution is formed into a "Taylor cone" by using a high-voltage electrostatic field. When the charge repulsion exceeds the surface tension, the polymer jet is ejected. After stretching under an electric field and by solvent evaporation, it solidifies and coalesces into nanofibers with uniformly dispersed particles. The synthesis provides abundant active sites for NVPF nanomaterials by constructing carbon fiber long-range electronic pathways. It is also possible to prepare self-supported flexible electrodes in one step, bypassing conductive agent and binder addition and simplifying cathode production. Unfortunately, the electrospinning process needs to be carried out at high temperatures and pressures, and the environmental and equipment conditions for spinning affect the quality of the spinning. Moreover, the time-consuming feature of the electrospinning method is not well suited for high-efficiency practical applications.

2.3 Challenges of NVPF

NVPF with a fluorophosphate structure has been extensively studied and unique advantages have been demonstrated.[82] Yet, for further practical applications, NVPF still faces two major challenges, mainly including low intrinsic conductivity and irreversible structural evolution. Although the PO_4 tetrahedral unit can provide a stable backbone structure for the transport of sodium ions, electron transport is hindered by the insulating PO_4 units, which will seriously affect the electron migration in NVPF nanocrystals.[57] Under such conditions, the electronic conductivity of pure NVPF is as low as 10^{-9} to 10^{-12} S cm^{-1}, severely limiting its performance in practical applications such as high-rate charging. Also, numerous factors influence the irreversible structural evolution occurring in NVPF cathodes. The minor amount of H_2O present in the battery system during the charging and discharging process leads to the dissolution of ions and affects the electrochemical performance of NVPF cathodes. Liu *et al.* observed anisotropic changes in the lattice parameters of cycling NVPF electrodes during the charging process, suggesting the existence of ionic dissolution processes in the nanocrystalline structure of the cathode material.[83] Additionally, under high temperature conditions, the $[V_2O_8F_3]$ double octahedral structure was disrupted by the volatilization of fluorine, with some F^- sites being replaced by O_2^-. With further loss of fluorine, a heterogeneous $Na_3V_2(PO_4)_3$ phase forms, degrading electrochemical properties such as the working voltage plateau of the cathode. To compensate for the charge imbalance resulting from O_2^- replacing F^-, the transition metal V undergoes oxidation. This disrupts the structural ordering of the cathode and leads to irreversible structural evolution during electrochemical reaction. Li *et al.* further postulated a mechanism attributing capacity fade to fluorine

dissolution.[84] Corrosion at the current collector interface is caused by ion dissolution occurring in the NVPF electrode, which makes the NVPF electrode capacity decrease. The mechanism of NVPF based fluorinated solution driven degradation could be explained as follows.

$$Na_3V_2(PO_4)_2F_3 + xH_2O \rightarrow Na_3V_2(PO_4)_2F_{3-x} + xHF\uparrow \quad (4)$$

$$6HF + Al_2O_3 \rightarrow 2AlF_3 + 3H_2\uparrow \quad (5)$$

Recent studies have shown that the formation of the 3.3 V plateau in the charge–discharge curve of NVPF cathode materials may also be related to the loss of elemental fluorine.[85] It was found based on F and Na nuclear magnetic resonance (NMR) spectra that after the spin sidebands were subtracted, two resonance absorption peaks appeared in the spectra, which corresponded to the two F sites in the NVPF. Last but not least, to further increase the theoretical capacity of NVPF cathodes, researchers attempted to achieve reversible insertion/extraction of the third sodium ion by expanding the voltage window. Unfortunately, the excessive oxidation of transition metal elements triggered irreversible structural changes, sacrificing the excellent cycling stability of NVPF cathodes.

To address the above challenges, nanoengineering studies targeting the NVPF cathode material are essential. The aim of this paper is to explore emerging nanoengineering research for fluorophosphate structure NVPF cathode materials, investigating the interfacial and bulk behavior of NVPF at the

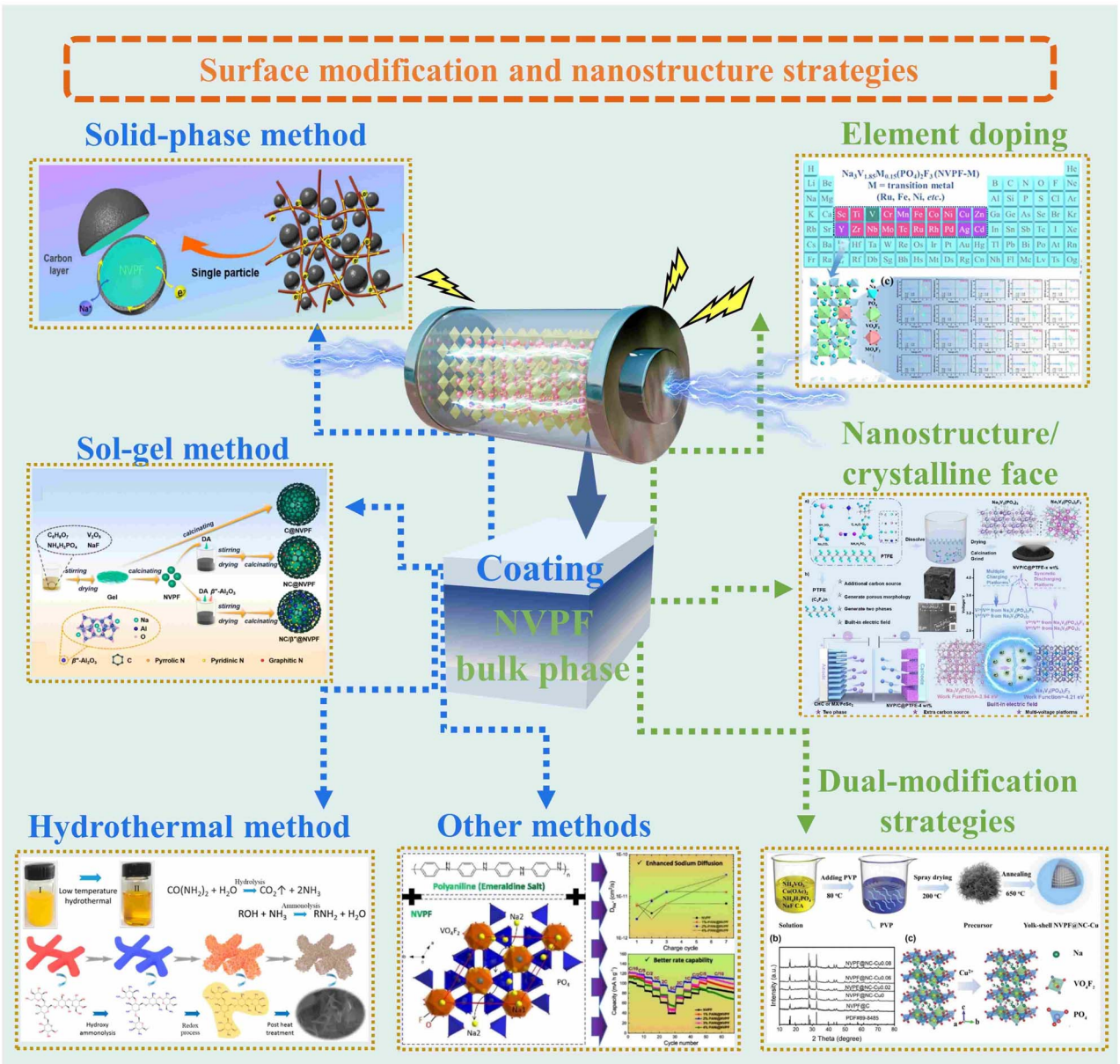

Fig. 4 The schematic diagram of the application and classification of nanoengineering in NVPF.[80,86–91] Copyright 2022, Wiley-VCH. Copyright 2024, American Chemical Society. Copyright 2022, American Chemical Society. Copyright 2025, Wiley-VCH. Copyright 2024, Royal Society of Chemistry. Copyright 2023, Wiley-VCH.

nanoscale and employing multiple synergistic strategies to address challenges. A detailed classification review based on different nanotechnology engineering approaches has been presented to summarize past research findings and provide a reference for future studies (Fig. 4).

3 Nanoscale surface modification

Taking into account the problems related to the poor intrinsic electronic conductivity and ion solubilization of NVFP, surface modification by nanoengineering is a common method used by researchers.[92] Wrapping a nanoscale conductive coating on the surface of the cathode material can optimize the electron transport ability and promote the co-diffusion between ions and electrons. Besides, the coating material with stability and mechanical robustness serves as an anticorrosion layer to avoid the side reaction of the electrolyte on the cathode. At the same time, it buffers the volume change of the cathode material when it undergoes ion exchange. The following review summarizes representative modification achievements in recent years and classifies them according to their preparation and processing methods (Table 1).

3.1 Solid-phase method

The solid-phase method as a common preparation process includes branches such as the high temperature solid state method and mechanochemical solid state method.[93–95] The advantages include the convenience of the method, lower energy consumption, better product purity and crystallinity, as well as low cost with potential for scale-up preparation.[96,120] A large number of nano-engineered surface modifications are therefore carried out based on the solid-state method. Gao *et al.* proposed a cathode material (NVPF@C@CNTs) prepared by the solid-state method.[86] The multidimensional carbon nanoframework is composed of amorphous carbon and carbon nanotubes with NVPF materials by cross-linking. This delicate design ensures that the NVPF@C@CNTs have a suitable particle size and shorten the sodium ion transfer pathway. The electron transfer network was further improved, resulting in enhanced charge transfer kinetics and superior cycling stability of the positive electrode. The *in situ* X-ray diffraction (XRD) method was used to reveal the charge/discharge mechanism of the NVPF@C@CNTs electrode at a current density of 0.5 C and a voltage of 2.5 to 4.3 V (Fig. 5a and b). When the NVPF@C@CNTs electrode is charged to 3.7 V, both the (220) and (222) peaks are shifted to a higher angle, while the (002) peak is shifted to a lower angle, which corresponds to a two-phase change from $Na_3V_2(PO_4)_2F_3$ to $Na_2V_2(PO_4)_2F_3$. When the voltage reaches 4.1 V, the positions of the three peaks change more distinctly, indicating that the sodium ions are extracted by conversion of sodium ions from $Na_2V_2(PO_4)_2F_3$ to $NaV_2(PO_4)_2F_3$. The exact opposite ion-exchange process is shown during discharge, with all diffraction peaks of the NVPF@C@CNTs electrode shifting back to the initial position with discharge to 2.5 V. These demonstrate that a single-phase solid solution reaction process occurs during both charging and discharging, and that the electrochemical behavior of the NVPF@C@CNTs electrodes is a rather reversible sodium ion extraction/insertion process, corroborating eqn (2) and (3) mentioned above. As a result, the NVPF@C@CNTs cathode shows excellent electrochemical performance, including excellent initial specific capacity (126.9 mAh g^{-1}) and cycling stability (93.9% capacity retention over 1000 cycles at 20 C) (Fig. 5c). In addition, the NVPF@C@CNTs//HC full cell achieves an energy density of 405.5 Wh kg^{-1} (based on the cathode mass) and delivers great cycling performance at high temperatures (50 °C).

Aiming at solving problems such as low energy density due to the intrinsically low compaction density of NVPF cathode materials, Song *et al.* used a high-temperature shock synthesis strategy to prepare high-pressure, solid-density NVPF materials with a uniform conductive network.[97] Owing to the unique preparation process, the precursors crystallize rapidly and form large, dense particles during the rapid heating process. Further enhancing the contact between the NVPF cathode and the carbon coating also reduces the occurrence of side reactions between the interface and the electrolyte. Ultimately, the formation of heterogeneous phases and the unnecessary loss of the F element are reduced during the preparation process, which ensures the stability of the NVPF cathode. For demonstrating the advantages offered by the high-temperature shock synthesis strategy, the authors investigated the structural evolution of NVPF in different synthesis processes. *In situ* XRD showed that although the different synthesis methods presented the same reaction path (Fig. 5d), however, the characteristic peak of NVP at 14° occurs using the conventional preparation method, which is closely related to the undesired loss of the F element. It was also found that the cathode material decomposes to produce minor amounts of V_2O_5 and Na_3VF_6 during the conventional preparation process (eqn (6) and (7)), which further weakens the electrochemical performance of the NVPF cathode.

$$2VPO_4 + 3NaF \rightarrow Na_3V_2(PO_4)_2F_3 \quad (6)$$

$$Na_3V_2(PO_4)_2F_3 \rightarrow Na_3V_2(PO_4)_3 + V_2O_3 + Na_3VF_6 + \text{others} \quad (7)$$

Ultimately, the modified batteries achieve excellent electrochemical performance over an ultra-wide temperature range (−45–55 °C). Also, this energy-saving and efficient preparation strategy extends the efficient preparation technology of the cathode material. Gu *et al.* utilized agarose as a novel carbon precursor to achieve a highly uniform carbon coating on NVPF nano-positive materials.[92] Not only was the electronic conductivity of the cathode material improved and the Na^+ migration path of the NVPF nanomaterials shortened, the discharge/charge plateau of the battery was also surprisingly modulated for the first time by carbon nano-surface engineering, which led to the improvement of the energy density and average voltage. Test results show that when the applied voltage is 3.75 V, a two-phase transition from $Na_3V_2(PO_4)_2F_3$ to $Na_2V_2(PO_4)_2F_3$ is demonstrated with the extraction of sodium ions at the full occupied position (corresponding to the diffraction peaks of (222) and (220), and to the new diffraction peaks formed by the

Table 1 The summarization of electrochemical performance of NVPF-based cathodes based on nanoscale surface modification

Material	Preparation method	Electrolyte	Electrochemical performances (discharge capacity, current density, cycles, and capacity retention)	Ref.
NVPF/C	Solid-phase	1 M $NaClO_4$ in EC/DMC/EMC (1 : 1 : 1) with 2 wt% FEC	103 mAh g^{-1}, 0.2 C, 500, 91.9%	69
NVPF@C	Solid-phase	1 M $NaClO_4$ in PC with 5 vol% FEC	115.9 mAh g^{-1}, 0.1 C, 200	92
Gl-NVPF	Solid-phase	1 M $NaClO_4$ in PC with 5 wt% FEC	122 mAh g^{-1}, 0.1 C, 1000, 83.2%	93
C-NVPF	Solid-phase	1 M $NaClO_4$ in EC/DEC (1 : 1)	110.6 mAh g^{-1}, 0.1 C, 2000, 54%	94
NVPF@rGO	Solid-phase	1 M $NaClO_4$ in EC/PC (1 : 1) with 5 wt% FEC	123 mAh g^{-1}, 0.5 C, 5000, 64%	95
NVPF@C-90	Solid-phase	1 M $NaPF_6$ in EC/DMC (1 : 1) with 2 wt% FEC	123 mAh g^{-1}, 0.05 C, 100, 96%	96
NVPF@C@CNTs	Solid-phase	1 M $NaClO_4$ in PC	126.9 mAh g^{-1}, 1 C, 1000, 93.9%	86
HTS-NVPF	Solid-phase	1 M $NaClO_4$ in EC/PC (1 : 1) with 5 wt% FEC	116.8 mAh g^{-1}, 0.1 C, 1000, 84.2%	97
NVPF-microwave	Solid-phase	1 M $NaClO_4$ in EC/DEC (1 : 1)	127.41 mAh g^{-1}, 0.1 C, 500, 95.19%	67
NVPF-NC	Solid-phase	1 M $NaClO_4$ in EC/PC (1 : 1) with 5 wt% FEC	107.7 mAh g^{-1}, 30 C, 2500, 84.8%	98
NVPF@C@CMC	Sol–gel	1 M $NaClO_4$ in EC/DMC/EMC (1 : 1 : 1) with 5 vol% FEC	125.8 mAh g^{-1}, 0.2 C, 500, 74%	99
NVPF@NC	Sol–gel	1 M $NaClO_4$ in EC/PC (1 : 1) with 5 wt% FEC	120.3 mAh g^{-1}, 0.1 C, 500, 72.7%	100
NVPF-PCNB-20	Sol–gel	1 M $NaClO_4$ in PC with 5 wt% FEC	109 mAh g^{-1}, 0.5 C, 750, 92.8%	101
NVPF@C-PTFEc	Sol–gel	1 M $NaClO_4$ in EC/DMC/EMC (1 : 1 : 1) with 2 vol% FEC	125.7 mAh g^{-1}, 0.1 C, 500, 85.3%	102
NVPF@NSC-15	Sol–gel	1 M $NaClO_4$ in EC/DMC (1 : 1) with 5 wt% FEC	126.3 mAh g^{-1}, 0.2 C, 100, 99.5%	103
NC/C@NVPF	Sol–gel	1 M $NaClO_4$ in EC/DMC/EMC (1 : 1 : 1) with 2 vol% FEC	125.7 mAh g^{-1}, 0.2 C, 1500, 89.8%	104
HM-NVPF@CN	Sol–gel	1 M $NaClO_4$ in PC	70 mAh g^{-1}, 20 C, 2000, 80%	105
C-NVPF	Sol–gel	1 M $NaClO_4$ in EC/PC (1 : 1)	126 mAh g^{-1}, 0.1 C, 500, 70%	106
NVPF@C-10PVP	Hydrothermal	1 M $NaClO_4$ in EC/DMC (1 : 1) with 5 wt% FEC	127.8 mAh g^{-1}, 0.2 C, 100, 82.8%	107
NVPF@C/CNTs	Hydrothermal	1 M $NaClO_4$ in PC with 5 wt% FEC	107 mAh g^{-1}, 0.2 C, 500	108
NVPF-gel/rGO	Hydrothermal	1 M $NaClO_4$ in PC/EC (1 : 1) with 5 wt% FEC	125.1 mAh g^{-1}, 0.2 C, 200, 86.4%	109
MW-NVPF@C	Hydrothermal	1 M $NaClO_4$ in EC/PC (1 : 1) with 5 wt% FEC	109 mAh g^{-1}, 0.1 C, 100, 100%	110
NVPF@C@rGO	Hydrothermal	1 M $NaClO_4$ in EC/DEC (1 : 1) with 5 wt% FEC	64 mAh g^{-1}, 100 C, 700, 98.3%	111
NVPF@rGO/CNT	Hydrothermal	1 M $NaPF_6$ in DGDME	101 mAh g^{-1}, 60 C, 6000, 88.4%	112
NVPF/C-NS	Hydrothermal	1 M $NaClO_4$ in EC/PC (1 : 1) with 5 wt% FEC	93 mAh g^{-1}, 60 C, 500, 93%	88
PANI@NVPF	Other	1 M $NaClO_4$ in PC/FEC (95 : 5 vol%)	125 mAh g^{-1}, 0.1 C, 70%	91
NVPF self-standing cathode	Other	1 M $NaClO_4$ in K1/EC/PC (1 : 3 : 6) with 2 vol% FEC	101.8 mAh g^{-1}, 0.2 C, 400, 98.3%	113
NVPF@C-4	Other	1 M $NaClO_4$ in EC/DMC (1 : 1) with 5 wt% FEC	121.5 mAh g^{-1}, 0.1 C, 1000, 90.1%	114
$Na_3V_2(PO_4)_2F_3$/C	Other	1 M $LiPF_6$ in EC/DMC (1 : 1)	125 mAh g^{-1}, 0.1 C, 80, 78.23%	115
NVPF/CNTs	Other	1 M $NaClO_4$ in EC/PC (1 : 1) with 5 wt% FEC	127.7 mAh g^{-1}, 0.1 A g^{-1}, 20 000, 92.1%	116
$Na_3V_2(PO_4)_2F_3$/Co/N-PC	Other	1 M $NaClO_4$ in EC/PC (1 : 1) with 5 wt% FEC	126.66 mAh g^{-1}, 0.1 C, 100, 91.84%	117
NVPF@C/CC	Other	1 M $NaClO_4$ in EC/DMC (1 : 1)	77.6 mAh g^{-1}, 30 C, 2000, 83.8%	118
NVPF-18	Other	1 M $NaPF_6$ in EC/PC (1 : 1) with 5 vol% FEC	74.7 mAh g^{-1}, 30 C, 3000, 82.8%	119
NVPF-4%P	Solid-phase	1 M $NaClO_4$ in EC/DMC (1 : 1) with 5 vol% FEC	119 mAh g^{-1}, 0.5 C, 500, 82.1%	120

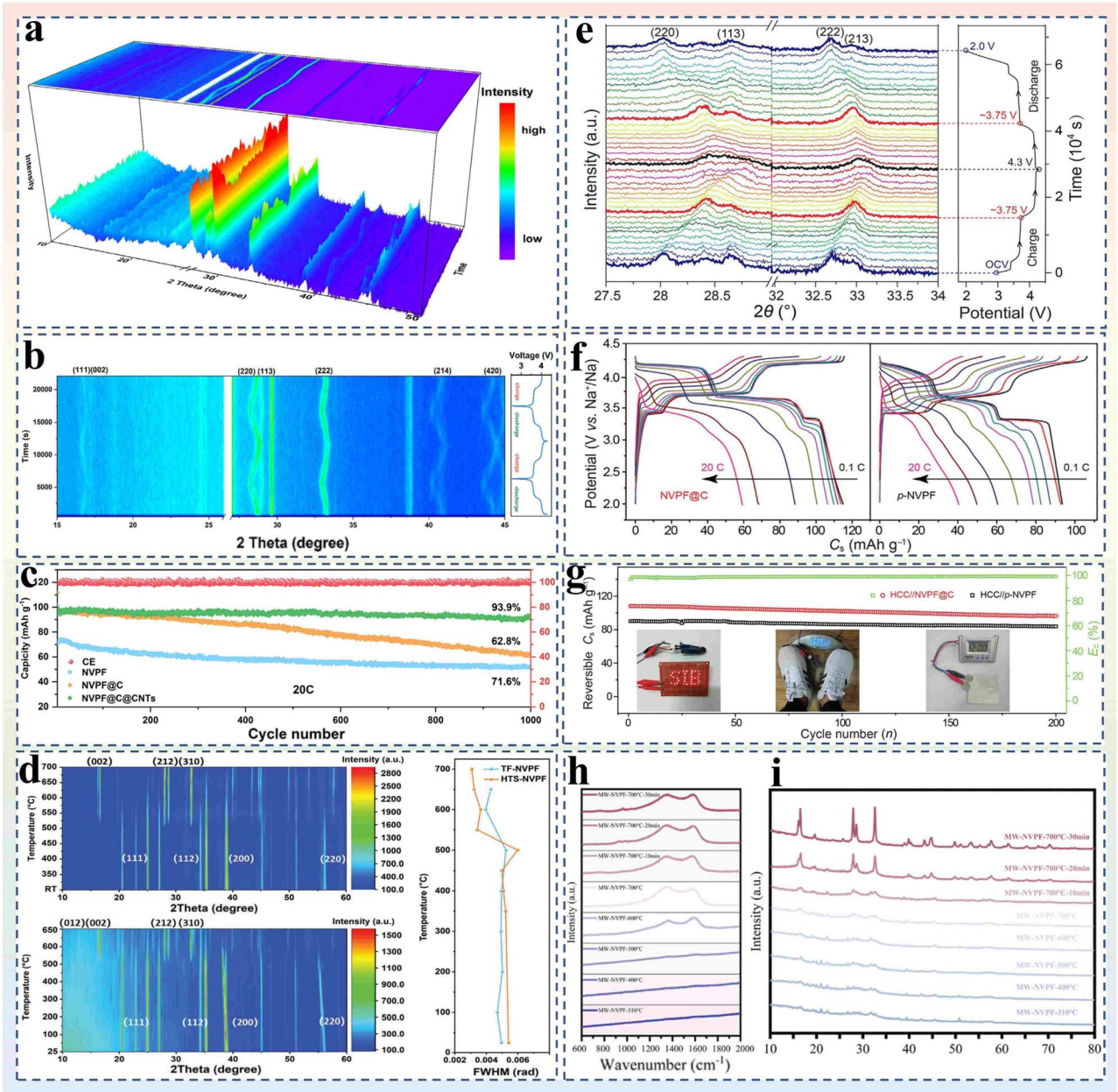

Fig. 5 (a) 3D *in situ* XRD pattern and (b) structural evolution of NVPF@C@CNTs electrodes. (c) Long-term cycling performances and coulombic efficiency of all samples.[86] Copyright 2022, Wiley-VCH. (d) *Ex situ* XRD pattern of HTS-NVPF and *in situ* XRD pattern of TF-NVPF during the heating process; and full width at half maxima of TF-NVPF and HTS-NVPF at different temperatures.[97] Copyright 2024, Wiley-VCH. (e) The partly enlarged *in situ* XRD patterns between 27.5° and 34° with the corresponding GCD curve. (f) Rate capability and the corresponding GCD curves. (g) Cycling performance of SIBs at 0.5C, and the insets show the practical application of HCC//NVPF@C SIFBs.[92] Copyright 2020, Elsevier. (h) Quasi-*in situ* Raman spectral changes. (i) The quasi-*in situ* XRD pattern changes.[67] Copyright 2025, Royal Society of Chemistry.

merging of (222) and (213)) (Fig. 5e). As the voltage is further increased to 4.3 V, the (220) peak is further shifted to a higher angle and then merges with (113) to form a broad peak, which forms a peak located at a high angle of 32.92°. This shows the evolution of the crystal structure of $Na_2V_2(PO_4)_2F_3$ converted to $NaV_2(PO_4)_2F_3$ after the extraction of another Na ion. During the sodiation process carried out from 4.3 V to 2.0 V, the diffraction peaks are well restored to the original state except for a few diffraction intensities. This indicates that the two-electron reaction occurring in the lattice of the electrode material has a high structural reversibility in the extraction/intercalation process of sodium ions at the NVPF@C electrode material. Furthermore, NVPF@C achieved greater specific capacity and improved rate performance compared to NVPF materials without nano-engineered surface modification (Fig. 5f). The full cell assembled with hard carbon also demonstrated potential for application in SIBs (Fig. 5g).

Apart from the above work, NVPF with a uniform carbon coating microstructure was prepared by ultra-fast (40 min) synthesis which used the microwave-assisted solid-phase method by He *et al.*[67] Specifically, the cathode material NVPF-microwave was prepared ultra-fast utilizing a low-cost combination of NH_4F, $NH_4H_2PO_4$, NH_4VO_3, and Na_2CO_3 and employing glycerol as a carbon source. Three key stages were observed during the microwave-assisted synthesis: the initial heating stage (to 700 °C), the intermediate reaction and sintering stage (700 °C for 10–20 min), and the final sintering stage (700 °C to completion) (Fig. 5h and i). The novel microstructures can produce a dense carbon coating and ultimately enhance the cycling performance and high-rate performance of the battery (only a 4.81% decay rate after 100 cycles at 2 C). In addition, Li *et al.* prepared delicate nano-cubic block structures of NVPF without obvious agglomeration traces and individually encapsulated in carbon *in situ* by a simple modified solid-state synthesis process.[98] During the preparation process, paraffin as the dispersant and the surfactant act synergistically to form a quasi-water-in-oil medium. Delicate, stretched carbon films were generated *in situ* on the NVPF surface while modulating particle growth. The experimental results showed that different choices of surfactant types and doses resulted in different microstructural changes. The protective effect by the carbon coating promoted the Na^+ migration and charge transfer kinetics, resulting in good cycling and rate performance of NVPF-NC. Also, the migration kinetics and storage mechanism of the electrode were investigated by other tests and characterization studies.

Even though promising results have been achieved, there are still some limitations in the application of the solid-state method to nano-engineering of NVPF surfaces. Inevitably, elemental fluorine is lost during the reaction process of high temperature solid-state methods, which results in the production of impurities and affects the purity of the samples. Besides, the particle size of the product of the traditional solid-state method is not uniform, which makes it difficult to further carry out accurate secondary micro-regulation of nanostructures. Yet, as the cornerstone process for the future industrialized production of NVPF, the integration of other advanced preparation technologies on the basis of the traditional solid-state method has tremendous potential for application.

3.2 Sol–gel method

The sol–gel method has significant advantages in material homogeneity, compositional regulation and low-temperature synthesis in the preparation of NVPF cathode materials by virtue of its uniquely advantageous liquid-phase reaction mechanism.[87,99–103] Meanwhile, significant breakthroughs have also been made in the surface nanoengineering modification of NVPF cathode materials. Sun *et al.* constructed a bifunctional carbon network consisting of N-doped carbon layers and carbon bridges around NVPF cathode nanoparticles.[104] *In situ* coatings with N-doped carbon frameworks were generated by pyrolysis of polydopamine as well as polytetrafluoroethylene and tightly covered with NVPF. Besides, polytetrafluoroethylene (PTFE) serves as an elemental fluorine reagent. Even if a trace loss of the fluorine element occurs during the synthesis process, the purity of the sample will be guaranteed. As presented in the Fig. 6a, the nanocrystal structure of the prepared material NC/C@NVPF is shown, which has a three-dimensional framework consisting of $[PO_4]$ tetrahedra and $[V_2O_8F_3]$ double octahedra. Na ions occupy interstitial positions between the $[VO_4F_2]$ octahedral units, favoring its migration during ion exchange. Also, transmission electron microscopy (TEM) tests showed nice lattice striations and crystallinity of the material, while it was observed that the NVPF cathode material was uniformly wrapped by nanometer-thick amorphous carbon (Fig. 6b). The presence of pyrrolic nitrogen and pyridinic nitrogen associated with defects was observed by X-ray photoelectron spectroscopy (XPS). Their ability to provide additional sodium storage sites for NVPF nanocrystals facilitates the transport of sodium ions. The cathode material exhibited a high discharge specific capacity of 125.7 mAh g^{-1} at 0.2 C in a half-cell, and an outstanding capacity retention of 92.7% over 300 cycles at 1 C.

Beyond addressing the traditional challenges of NVPF, Hu *et al.* also investigated the issue of cathodic electrolyte interfaces associated with NVPF nanostructures.[105] The research work prepared homogeneous NVPF microspheres (HM-NVPF@CN) assembled from carbon-coated NVPF nanosheets and subsequently constructed a cathodic electrolyte interface layer enriched with inorganic B and F elemental on its surface. In the presence of a carbon coating layer, NVPF nanosheets shorten the diffusive transport paths of Na^+ and e^- and provide more electrochemical reaction sites. The strong protective layer enhances Na^+ transport and inhibits parasitic reactions. The von Mises stress distribution of spherical NVPF and nanosheet-assembled spherical NVPF was also calculated using COMSOL finite element simulations (Fig. 6c). The results show that the constructed unique two-dimensional structure effectively buffers the stress changes induced during volume expansion and ensures that the electrode maintains a relatively structurally stable particle structure during repeated sodium ion extraction/insertion processes. The *ex situ* XRD patterns of the electrodes throughout the cycle in different charging and discharging states show that the shift of the diffraction peaks corresponds to the two-phase reaction of NVPF when the voltage is gradually charged up to 3.8 V (Fig. 6d). When the applied voltage was increased to 4.3 V, the diffraction peaks did not change significantly except for a small angular shift, showing a single-phase solid solution reaction. At the same time, when the battery was discharged back to 2.5 V, all diffraction peaks can be restored to the original state. Based on the calculation, the change in the volume of a single cell during a full charge/discharge cycle cycle is only 0.5%. The results demonstrate the stability of the nanolattice structure of the NVPF electrode material. Finally, the modified electrode showed impressive cycling stability and multiplicative capacity (70 mAh g^{-1}, 80% reversible capacity retention at 10 C after 2000 cycles) (70 mAh g^{-1} at 20 C). The full cell achieves decent rate performance even at 60 °C (72 mAh g^{-1} at 5 C).

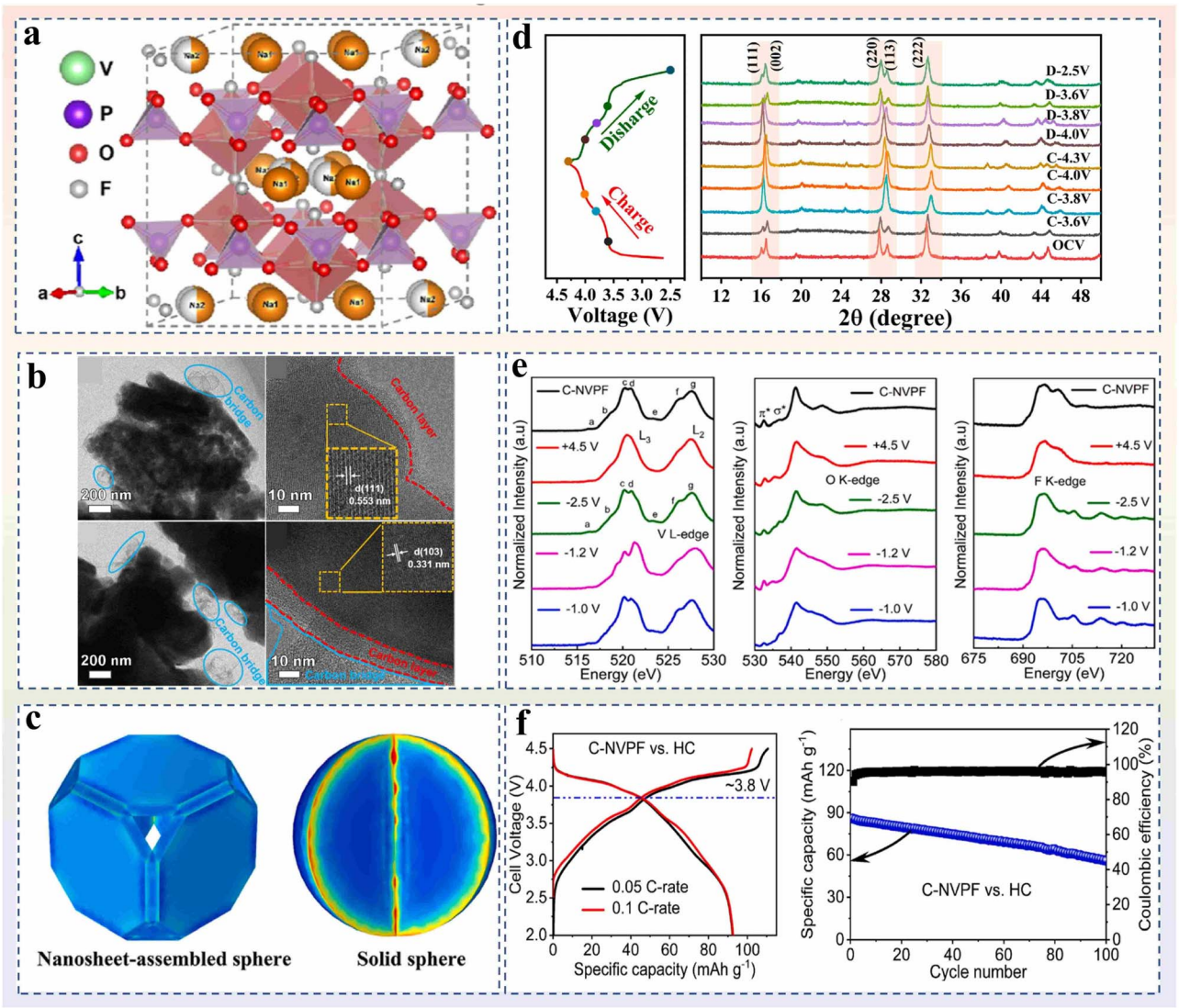

Fig. 6 (a) Crystal structure of NC/C@NVPF. (b) Transmission electron microscopy images of NC@NVPF and NC/C@NVPF.[104] Copyright 2024, American Chemical Society. (c) Finite element simulation models of nanosheet-assembled NVPF spheres and solid NVPF spheres with the von Mises stress distribution. (d) The voltage profile of HM-NVPF@CN-BPG during the whole charge–discharge process and the corresponding *ex situ* XRD patterns of HM-NVPF@CN-BPG at different states.[105] Copyright 2024, Elsevier. (e) Near edge X-ray absorption fine structure of desodiated and sodiated states for the vanadium L_{23}-edge, oxygen K-edge and fluorine K-edge. (f) Charge–discharge profile of C-NVPF *vs.* the HC full cell at different C-rates and cycling stability of C-NVPF *vs.* the HC cell at 0.1 C-rate.[106] Copyright 2025, Elsevier.

To enhance the specific energy of NVPF materials, *in situ* N-doped carbon-coated C-NVPF nanoparticles in mesoporous carbon were synthesized *via* a scalable microwave-assisted sol–gel route.[106] XRD characterization confirmed the successful preparation of pure-phase C-NVPF nanocrystals with P_{42}/mnm spatial punctuation. Confocal Raman spectroscopy confirmed the presence of disordered carbon from the decomposition of the citric acid chelator used in the gelling process. The elements of the NVPF nanomaterials were investigated by XPS. The presence of a higher percentage of pyrrolidine nitrogen enhances the electronic conductivity of the C-NVPF composites due to the presence of lone-pair electrons, which promotes the intrinsic electronic conductivity of the positive electrode. Scanning electron microscopy (SEM) and selected-area electron diffraction characterized the size of NVPF nanoparticles (30–160 nm) and the thickness of the modified carbon coating (6–9 nm). The structural stability of excessively sodiated C-NVPF was investigated using *ex situ* XRD. After 100 charge/discharge cycles at different cutoff voltages, the XRD spectrum of all the cycled electrodes maintained the square crystal structure without the appearance of obvious secondary peaks. The shift in the peak of C-NVPF when cycling below 2.5 V to 1.6 and 1.2 V, however, suggests that the insertion of excess sodium ions resulted in an increase in spacing. Eventually, in the 1.0 V discharge state, the inherent orthogonal distortion leads to a change of the space group to *Cmcm* with the appearance of a new diffraction peak in C-NVPF. Subsequently, to probe oxidation state evolution and local bonding interactions across

varying states of charge, V $L_{2,3}$-edge, O K-edge, and F K-edge near-edge X-ray absorption fine structure measurements were conducted on desodiated and sodiated C-NVPF samples (Fig. 6e). The results of the above studies strongly demonstrate that the electrochemical kinetics of the electrodes changed considerably at different charging and discharging depths. This is largely attributed to the structural-mechanical and thermodynamic variations of the electrode during sodium ion extraction/insertion of C-NVPF. After matching with hard carbon and assembling into a full cell, the C-NVPF electrode exhibited a specific capacity of 95 h g^{-1} and a potential with an average voltage of 3.8 V (Fig. 6f).

The limitations of the sol–gel method are the multi-step process (through sol formation, gelation, drying, sintering, *etc.*) and the costs associated with the raw materials used in the preparation (organic chelating agents, *etc.*). The stability of synthesized samples is strongly influenced by environmental factors and challenges are faced when scaling up industrially. Lastly, incompletely removed hydroxyl groups in the gel may result in the loss of elemental fluorine. Currently, the sol–gel method was mainly applied in laboratory grade preparation and research.

3.3 Hydrothermal method

Like the sol–gel method, in the preparation of NVPF nanocrystals, the hydrothermal method can also provide a liquid-phase reaction environment to provide suitable conditions for the controlled growth of nanograins. The difference is that, in the high-pressure environment provided by the hydrothermal reactor, the nanocrystals easily achieve directional growth, maintaining purity and high crystallinity. The reactor is also equipped with an inert gas environment, which avoids the oxidation of elemental V through a convenient process. The relatively efficient process flow and low energy consumption requirements of the hydrothermal method demonstrate the potential for industrialized production and preparation.[107–110] In this investigation, polyvinyl alcohol modulates the microscopic interaction between NVPF nanoparticles and the nano-protective layer through hydrogen bonding between intrinsic hydroxyl groups and rGO.[111] It was observed by TEM that an amorphous layer about 6 nm thick could be recognized near the NVPF nanoparticles, which could be due to the amorphous carbon produced by polyvinyl alcohol. In the outermost region, several rGO nano-protective layers are observed. It is demonstrated that polyvinyl alcohol effectively bridges NVPF and rGO to produce NVPF@C@rGO structures. In order to reveal the potential ion transport mechanism and nanocrystal structure changes during charging and discharging, *in situ* XRD tests were performed on NVPF@C@rGO and NVPF at 0.5 C (Fig. 7a). It is observed that NVPF@C@rGO exhibits a more symmetrical shift change of diffraction peaks during the test, with most of the peaks returning to their original positions after charging. This indicates a highly reversible extraction-embedding process with a more stable nanocrystal structure compared to the unmodified NVPF material. The XRD data were analyzed by the Rietveld method based on the Bragg equation. During charging, the lattice parameters *a* and *b* gradually decrease, while the value of *c* gradually increases; the opposite change occurs during discharge. Such phase transitions, as shown schematically, also identified more minute changes in the NVPF@C@rGO lattice parameters during charging and discharging (Fig. 7b). Benefiting from the advantages brought by the above studies, the prepared NVPF@C@rGO cathode has exceptional cycling stability and rate performance (cycling capacity of 64 mAh g^{-1} at 100 C and a capacity retention of 98.1% after 700 cycles at 50 C).

To improve all-climate performance for current energy storage batteries, researchers have successfully constructed NVPF cathode materials with two-dimensional reduced graphene oxide and one-dimensional carbon nanotubes covering the surface.[112] Through the simple hydrothermal self-assembly synthesis strategy, excellent electrochemical performance was achieved even with low carbon content in the cathode material and without the addition of additional conductive agents. Benefiting from the unique design of the cathode material structure and the assistance of a multidimensional composite carbon coating, the NVPF cathode exhibits excellent dynamic performance. Furthermore, *ex situ* XRD technology was used to study the structural evolution of the cathode during the first cycle (Fig. 7c). During the charging and discharging process of the electrode, no disappearance of the original diffraction peaks or generation of new diffraction peaks occurred. The slight shift in the diffraction peaks accompanying the insertion and extraction of sodium ions indicates a slight change in battery volume (0.4%). When charging and discharging return to the initial state, the diffraction peaks all return to the initial angle, proving that the structure of the prepared cathode material is super stable. As a result, the zero-strain cathode material demonstrated ultra-high-rate performance (capacity of 101 mAh g^{-1} at 60 C) and excellent cycle stability (capacity retention rate of 88.4% after 6000 cycles at 10 C). Even under test conditions with a wide temperature range of 90 °C, it still demonstrated impressive electrochemical reversible capacity.

Zhang *et al.* developed an efficient hydrothermal method to prepare carbon coated NVPF nanosheets *in situ*.[88] Urea with water-insoluble branched-chain starch and the NVPF precursor was first added to deionized water to form a suspension. After a low-temperature hydrothermal reaction, urea undergoes a hydrolysis reaction to release ammonia. Subsequently, the polymer chains of the branched starch react with amino groups to increase hydrophilicity. The NVPF precursor is similarly dissolved in ammonia, with the final reaction forming a clear solution. Moreover, NVPF nanocrystals tend to form two-dimensional nanosheets along the branched amylose polymer chains after the hydrothermal reaction. Simultaneously branched starch-derived pyrolytic carbon was coated *in situ* on the nanosheets to form a carbon-coated protective layer. XRD, thermogravimetric analysis, Raman spectroscopy and XPS showed the successful preparation of single-phase NVPF nanocrystalline materials with an *in situ* carbon coating layer (Fig. 7d). SEM and TEM as well as the corresponding elemental mapping analyses also well corroborate the above test results, and the samples demonstrate having a three-dimensional crosslinked structure built from interconnected nanosheets. Ultimately, the hydrothermal synthesis produces unique structures that endow the nanomaterials with efficient electron transfer capabilities and sodium storage-related electrochemical properties, in particular,

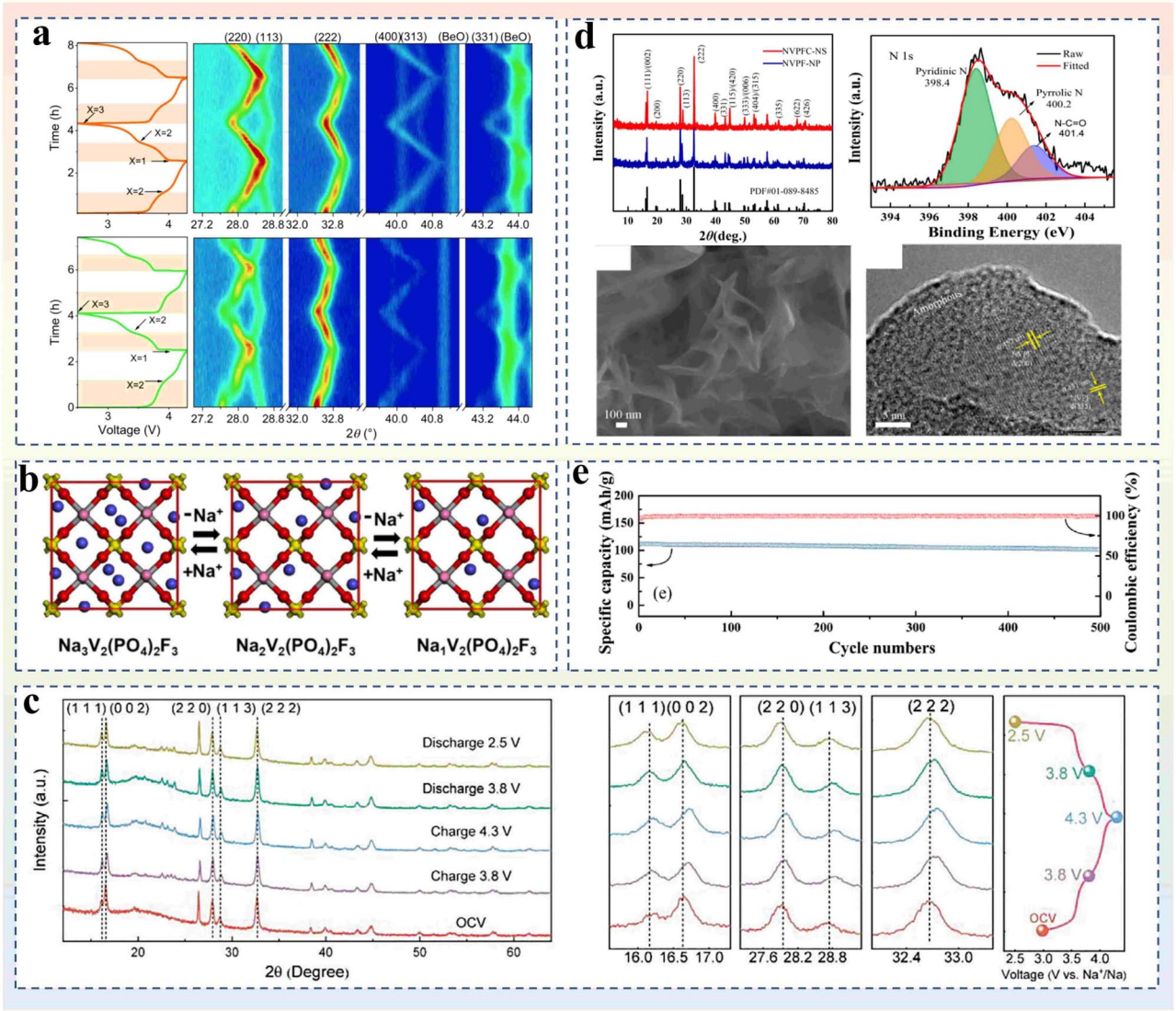

Fig. 7 (a) *In situ* XRD spectra of NVPF@C@rGO and NVPF. (b) Schematic representation of the structural changes of NVPF during the charge–discharge process.[111] Copyright 2024, Elsevier. (c) The XRD curves of NVPF@rGO/CNT at different potential stages.[112] Copyright 2023, Wiley-VCH. (d) XRD patterns, XPS spectrum, SEM image and HRTEM image of NVPFC-NS and NVPF-NP. (e) Cycling performance at 10C.[88] Copyright 2022, American Chemical Society.

a favorable rate performance (93 mAh g^{-1} at 60 C; 51 mAh g^{-1} at 150 C) and long cycle stability (93% capacity retention after 500 cycles at 10 C) (Fig. 7e).

3.4 Other methods

Except for the traditional and widely used synthesis methods mentioned above, as a complementary or auxiliary means, researchers have investigated many novel methods for the preparation of materials.[113–115,119,121] The synergistic effect of multiple synthesis processes is used to compensate for the dilemma faced by a single conventional process in the preparation of materials. A special kind of three-dimensional double carbon network interwoven NVPF nano-microsphere NVPF/CNTs were prepared by spray drying combined with the calcination method by Lei *et al.*[116] By applying a carbon protective layer on the NVPF surface, the electronic conductivity of the NVPF electrode is significantly improved and the occurrence of lattice distortion is effectively suppressed. Test results of material characterization and electrochemical properties demonstrate the successful preparation of NVPF/CNTs electrodes and the effectiveness of the modification means. In order to understand the charge transfer process at the electrodes of NVPF/CNTs, electrochemical impedance spectroscopy (EIS) measurements were performed. EIS curves of NVPF/CNTs in different charging and discharging states, are accompanied by a decrease in the semicircle size in the high-frequency region during the charging process of the battery, and the opposite is true during the discharging process. It is worth noting that the charge transfer resistance decreases only slightly when charging to the first plateau (3.4 V) but decreases dramatically when charging to the second plateau (3.7 V). This indicates that

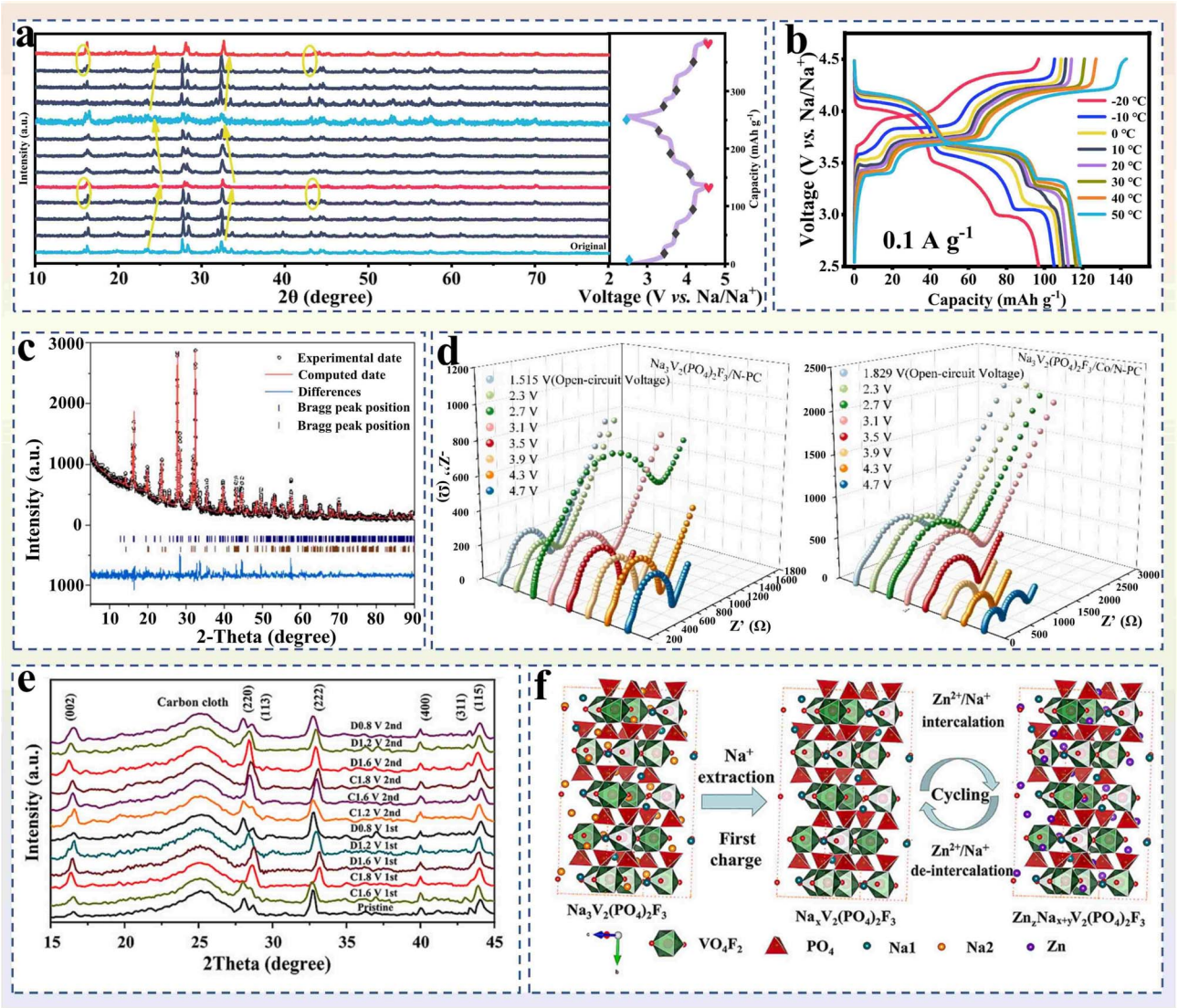

Fig. 8 (a) *Ex situ* XRD patterns of the NVPF/CNTs electrode collected at various voltages states. (b) Charge–discharge curves at different rates.[116] Copyright 2023, Elsevier. (c) XRD patterns of the metal MOF and results of the refined $Na_3V_2(PO_4)_2F_3$/N-PC composite with 5 wt% Co/N-PC content using fullprof. (d) Nyquist diagram of two electrode materials during the charging process.[117] Copyright 2025, Elsevier. (e) *Ex situ* XRD patterns of NVPF@C/CC in the two initial cycles. (f) The storage mechanism illustrations of the NVPF@C/CC electrode.[118] Copyright 2023, Elsevier.

a solid electrolyte interfacial layer is formed between the electrolyte and the electrode during this period, which reduces the interfacial impedance. Regarding the *ex situ* XRD patterns of NVPF/CNTs electrodes during charge/discharge cycling, it was observed that the XRD patterns of NVPF/CNTs were reproducible (Fig. 8a). The test results show that the extraction of sodium ions from the Na1 and Na_2 sites in the cathode material involves a solid solution reaction, and the crystal structure remains stable, ultimately returning to its initial state. This further demonstrates the highly stable crystal structure of the modified electrode during Na^+ extraction/insertion. As the cathode of the SIB, the half-cell demonstrated outstanding discharge performance, great cycle performance, and awesome low-temperature adaptability (Fig. 8b). Plus, the assembled full cell had an energy density of 353.4 Wh kg^{-1} and good cycle performance.

Ma *et al.* synthesized porous nitrogen-doped carbon nano-cube cathodes derived from bimetallic metal–organic framework materials through a process combining spray drying and high-temperature sintering (Fig. 8c),[117] enhancing the electrochemical performance of cathode materials through the synergistic effect between cobalt nanoparticles and carbon coatings. The orbital interaction between heteroatomic cobalt atoms and nitrogen atoms reduces the sodium ion extraction/insertion barrier. In addition, the electron-rich regions in the carbon coating attract sodium ions through electrostatic effects, thereby increasing the storage capacity of sodium ions and the reaction kinetics of the electrode. The Nyquist diagram shows that the addition of the carbon material effectively mitigates the damage caused by the electrolyte to the cathode material, enhances interface stability, and reduces interfacial charge transfer resistance (Fig. 8d). At

a rate of 0.1 C, the initial specific discharge capacity of the composite material reached 126.66 mAh g^{-1} and it retained 91.84% of its capacity after 100 cycles. This work demonstrates that it is feasible to modify NVPF electrode materials by utilizing the unique structure of metal–organic framework materials and converting them into carbon-coated materials. Ling *et al.* prepared highly flexible, three-dimensional porous NVPF cathodes coated with a nanocarbon layer using a crystal template method.[118] Thanks to the superiority of the structural design, the ordered NVPF microporous structure facilitates the rapid diffusion and transport of sodium ions, thereby improving the kinetic performance of the electrode. The uniform carbon coating on the cathode structure, combined with the conductive substrate, provides a convenient path for the continuous transmission of electrons. In addition, the strong chemical bonding between the cathode material and the conductive substrate prevents the active material from falling off and being lost, significantly improving cycle stability. *Ex situ* XRD techniques were used to study the ionic behavior of cathode materials during electrochemical processes (Fig. 8e). Throughout the study, all diffraction peaks in the XRD patterns could be clearly identified and correlated with their corresponding crystal planes. Furthermore, after two cycles, all diffraction peaks returned to their initial states, indicating the high stability of the prepared cathode structure. Additionally, when using the aqueous electrolyte, the NVPF cathode is capable of simultaneously inserting and extracting sodium ions and zinc ions, with the corresponding charge–discharge process and structural evolution shown in Fig. 8f. Consequently, in both SIBs and zinc-ion battery (ZIB) systems, such carefully designed NVPF cathodes have demonstrated outstanding electrochemical performance. This study also suggests a reasonable strategy for utilizing high-energy-density flexible electrodes, overcoming the structural limitations associated with traditional loading on active materials, and further expanding the application scope of flexible energy storage materials in practical applications.

Nanoscale surface modification effectively enhances electronic conductivity and provides protective support for cathode materials. Nevertheless, achieving uniform coatings is hindered by preparation limitations, and this strategy does not fundamentally address the intrinsic conductivity or structural stability of NVPF nanoparticles. Moreover, coating integrity deteriorates under prolonged cycling. Future advances lie in expanding the repertoire of coating materials, by leveraging composite design and synergistic effects among multiple components—ultimately enabling low-cost, easily prepared, and highly stable coatings.

4 Nanostructure tuning

Unlike nano-surface modification, nanostructure tuning gives researchers great scope to tailor the design of nanomaterials, such as defects and crystal structures. The low intrinsic conductivity of NVPF materials could be fundamentally improved by introducing other doping elements. The induced effect from the doping elements also modulates the redox plateau of the cathode. Furthermore, the kinetic performance of the electrodes is ultimately improved by regulating the growth of dominant crystalline surfaces, optimizing the ion nano-transport paths and rational nano-heterostructures. The battery's energy density is also enhanced by tailoring the electrode material's morphology and size for improved charge conduction (Table 2).

4.1 Element doping

The insulating structure [PO_4] leads to significantly poor conductivity of the NVPF nanocrystalline materials, which ultimately affects the rate performance of the electrodes at a high rate. Consequently, the intrinsic electrochemical and kinetic properties of NVPFs could be effectively enhanced by utilizing appropriate elemental doping.[122–128] Elemental doping is categorized into transition metal site doping, alkali metal site doping and polyanion site doping depending on the doping site. Transition metal site doping, as a well-studied modification, partially replaces V^{3+}/V^{4+} by introducing other transition metal ions. Due to the introduction of heterogeneous doping elements, the redox potential of the element V is effectively regulated, the electronic conductivity and ion diffusion rate are improved, and the crystal structure is stabilized. For overcoming the intrinsic deficiencies of NVPF materials by transition metal site doping, Hu *et al.* successfully synthesized Ti-substituted NVPF cathodes by the sol–gel method.[70] Theoretical calculations and comprehensive analytical characterization demonstrate that Ti substitution effectively stabilizes the chemical environment of the F element within the lattice, significantly mitigating the adverse effects of the low-voltage plateau on the electrochemical properties of the materials. By adjusting the energy band structure of the cathode, Ti substitution optimizes the migration path of sodium ions, reduces the diffusion energy barrier of sodium ions and improves the electronic conductivity and the diffusion kinetic performance of sodium ions in the material. DFT theoretical calculations and ultraviolet-visible diffuse reflectance spectroscopy were used to evaluate in detail the effect of Ti elemental substitution on the electronic conductivity. The narrower band gap suggests that the Ti element substitution promotes the electron jump from the valence band to the conduction band, which improves the electronic conductivity of the NVPF nanomaterials. *In situ* XRD tests show that the dopant-modified crystalline material exhibits higher stability under high-voltage conditions, which enables it to maintain its structural stability over a longer period of time, resulting in improved charging and discharging voltages and electrochemical performance. The mechanism of the influence on sodium ion migration from Na2 to Na3 sites in NVPF materials by Ti substitution was also systematically investigated by the climbing image nudged elastic band method (Fig. 9a). The optimized NVPF nanomaterials exhibit excellent cycle stability and multiplicity performance in the full cell. Similarly, Li *et al.* proposed a structural model for Fe-substituted NVPF and investigated its optimal chemical modification stoichiometry.[129] Fe^{3+} is more oxidizing (electron gaining ability) than V^{3+}, which changes the microscopic electronic energy band structure of NVPF nanocrystals. In addition, Fe ions have three more electrons than V ions, introducing new electronic energy levels in the forbidden band and enabling n-type doping. The induced effects of iron ions on the crystal

Table 2 The summarization of electrochemical performance of NVPF-based cathodes by the nanostructure tuning strategy

Material	Preparation method	Electrolyte	Electrochemical performances (discharge capacity, current density, cycles, and capacity retention)	Ref.
NVPF-Ti-0.05	Element doping	1 M $NaClO_4$ in EC/DMC (1 : 1) with 5 wt% FEC	129.1 mAh g^{-1}, 0.2 C, 6000, 81.14%	70
C-NVPF@NC	Dual-modification	1 M $NaClO_4$ in EC/DMC/EMC (1 : 1 : 1) with 5 vol% FEC	121 mAh g^{-1}, 0.2 C, 1000, 78%	75
$Fe_{0.1}$-NVPF@N-CNTs	Dual-modification	1 M $NaClO_4$ in DEC/EC (1 : 1) with 5 vol% FEC	105 mAh g^{-1}, 0.1 C, 1200, 83.38%	77
$Na_3V_{2-x}Cu_x(PO_4)_2F_3$@NC	Dual-modification	1 M $NaClO_4$ in EC/PC (1 : 1) with 5 vol% FEC	117.4 mAh g^{-1}, 0.1 C, 5000, 91.3%	80
NVPF/C-0.03Bi	Element doping	1 M $NaClO_4$ in PC with 2 vol% FEC	110 mAh g^{-1}, 0.1 C, 500, 80%	122
NVAPF-2	Element doping	1 M $NaClO_4$ in PC	106.4 mAh g^{-1}, 10 C, 500, 92.4%	123
NVPF-NS	Element doping	1 M $NaClO_4$ in PC with 5 vol% FEC	68 mAh g^{-1}, 20 C, 1000, 80.7%	124
$K_{0.10}$-NVPF	Element doping	1 M $NaClO_4$ in EC/DEC (1 : 1) with 5 vol% FEC	120.8 mAh g^{-1}, 0.1 C, 500, 97.5%	125
$Na_3V_{1.95}Zr_{0.05}(PO_4)_2F_3$/C	Element doping	1 M $NaClO_4$ in EC/DMC/EMC (1 : 1 : 1) with 2 wt% FEC	121.8 mAh g^{-1}, 0.2 C, 1000, 83.6%	126
HE-NVPF	Element doping	1 M $NaClO_4$ in PC with 5 vol% FEC	118.5 mAh g^{-1}, 0.1 C, 2000, 80.4%	127
$NV_{0.97}Fe_{0.03}PF$/C	Element doping	1 M $NaClO_4$ in EC/DMC (1 : 1)	126.7 mAh g^{-1}, 0.1 C, 300, 87.8%	129
NVMPF	Element doping	1 M $NaClO_4$ in EC/DMC (1 : 1) with 5 wt% FEC	124.5 mAh g^{-1}, 0.5 C, 12 000, 70.5%	130
NVPF-Ru	Element doping	1 M $NaClO_4$ in EC/DEC (1 : 1) with 5 wt% FEC	125.1 mAh g^{-1}, 0.5 C, 2000, 93.6%	89
$N_{0.92}K_{0.08}VPF$/C	Element doping	1 M $NaClO_4$ in PC/EC (1 : 1) with 5 wt% FEC	128.8 mAh g^{-1}, 0.2 C, 5000, 60.2%	131
$Na_{2.9}Li_{0.1}V_2(PO_4)_2F_3$/CNTs-Al(C)	Element doping	1 M $NaPF_6$ in DGDME	75.27 mAh g^{-1}, 50 C, 30 000, 64.1%	132
NVPOF-80	Element doping	1 M $NaClO_4$ in PC/EC (1 : 1) with 5 wt% FEC	68.6 mAh g^{-1}, 100 C, 1300, 98.3%	133
PA-NVPOF	Element doping	1 M $NaClO_4$ in EC/DMC (1 : 1) with 1 wt% FEC	129.5 mAh g^{-1}, 0.1 C, 500, 54.4%	134
NVOPF-PE	Element doping	1 M $NaClO_4$ in PC with 2 vol% FEC	129 mAh g^{-1}, 10 C, 6000, 94.5%	135
$NVPOF-Mg_{0.10}$	Element doping	1 M $NaClO_4$ in PC/EC (1 : 1) with 5 vol% FEC	116 mAh g^{-1}, 10 C, 500, 96.3%	136
$Na_3V_{1.84}Fe_{0.16}(PO_4)_2F_3$	Element doping	1 M $NaClO_4$ in EC/PC (1 : 1) with 5 vol% FEC	57.32 mAh g^{-1}, 10 C, 1000	137
$NVPOFSi_{0.05}$	Element doping	1 M $NaClO_4$ in PC with 5 vol% FEC	75.5 mAh g^{-1}, 30 C, 1000, 100%	138
NVPF@3% CNT	Nanostructure	1 M $NaClO_4$ in EC/PC (1 : 1) with 5 vol% FEC	105 mAh g^{-1}, 0.5 C, 200, 94%	139
MX-5	Nanostructure	1 M $NaClO_4$ in PC	92 mAh g^{-1}, 1 C, 350, 27%	140
NVPF@CNT-1	Nanostructure	1 M $NaClO_4$ in EC/DEC/DMC (1 : 1 : 1) with 5 vol% FEC	113.7 mAh g^{-1}, 1 C, 5000, 77.3%	141
NVPF/NCM811	Nanostructure	0.5 M $NaPF_6$ in PC with 2 vol% FEC	147 mAh g^{-1}, 0.1 C, 200	142
NVP/C@PTFE-4 wt%	Nanostructure	1 M $NaClO_4$ in EC/DEC (1 : 1) with 5% FEC	139.8 mAh g^{-1}, 0.1 C, 1500, 81.3%	90
PB/NV@APT	Nanostructure	1 M $NaClO_4$ in EC/DMC/EMC (1 : 1 : 1) with 2 vol% FEC	124.9 mAh g^{-1}, 100 mA g^{-1}, 500, 78%	143
NFC-2	Nanostructure	1 M $NaClO_4$ in PC/EC (1 : 1) with 5 wt% FEC	114.8 mAh g^{-1}, 20 mA g^{-1}, 10 000, 75.7%	144
NVPF-(002)	Nanostructure	1 M $NaClO_4$ in PC/EC (1 : 1) with 5 vol% FEC	124 mAh g^{-1}, 2 C, 1400, 89%	145
NVPF@3Dc	Dual-modification	1 M $NaClO_4$ in EC/PC (1 : 1) with 2 wt% FEC	131.5 mAh g^{-1}, 0.2 C, 2500, 63.7%	64
NVFNPF4	Dual-modification	1 M $NaClO_4$ in EC/PC (1 : 1) with 2 wt% FEC	115.58 mAh g^{-1}, 0.1 C, 500, 87.79%	146
NVPF-Ca-0.05/C	Dual-modification	1 M $NaClO_4$ in EC/PC (1 : 1) with 5 vol% FEC	124 mAh g^{-1}, 0.1 C, 1000, 70%	147
$NV_{1.98}Cr_{0.02}PF$/C	Dual-modification	1 M $NaClO_4$ in EC/PC (1 : 1) with 5 vol% FEC	91.2 mAh g^{-1}, 30 C, 200, 93.62%	148
NVPF@R3	Dual-modification	1 M $NaClO_4$ in EC/DMC (1 : 1) with 5 vol% FEC	115.8 mAh g^{-1}, 20 C, 1000, 77.29%	149
$Na_3V_{2-x}Cr_x(PO_4)_2F_3$/C	Element doping	1 M $NaClO_4$ in PC with 5 wt% FEC	101.9 mAh g^{-1}, 10 C, 1000, 68.7%	150
$Na_3V_{1.95}Mn_{0.05}(PO_4)_2F_3$@C	Dual-modification	1 M $NaClO_4$ in EC/DMC (1 : 1) with 5 vol% FEC	122.9 mAh g^{-1}, 0.2 C, 500, 88.69%	151
NVPFOy/C	Dual-modification	1 M $NaPF_6$ in EC/DMC (1 : 1) with 2 wt% FEC	—	152
NVSPF/C-0.04	Dual-modification	1 M $NaClO_4$ in PC with 5 vol% FEC	125 mAh g^{-1}, 0.2 C, 1000, 90%	153
$NVPF-Mg_{0.5}$	Dual-modification	1 M $NaClO_4$ in EC/DMC (1 : 1) with 5% FEC	126.8 mAh g^{-1}, 0.1 C, 1000, 70%	154
NKVMPF	Dual-modification	1 M $NaClO_4$ in EC/DMC/DMC (1 : 1 : 1)	124.3 mAh g^{-1}, 0.1 C, 1000, 93.1%	155
$NVZ_{0.03}PF$@C	Element doping	1 M $NaPF_6$ in DGDME	124 mAh g^{-1}, 0.5 C, 2000, 90%	128
NVPF-Br	Element doping	1 M $NaPF_6$ in PC with 2% FEC	169 mAh g^{-1}, 64 mA g^{-1}, 150, 79.29%	156
ME-$NV_{1.2}PF$@CNTs	Dual-modification	1 M $NaClO_4$ in DEC/EC (1 : 1) with 5 vol% FEC	120 mAh g^{-1}, 0.1 C, 3000, 60%	157

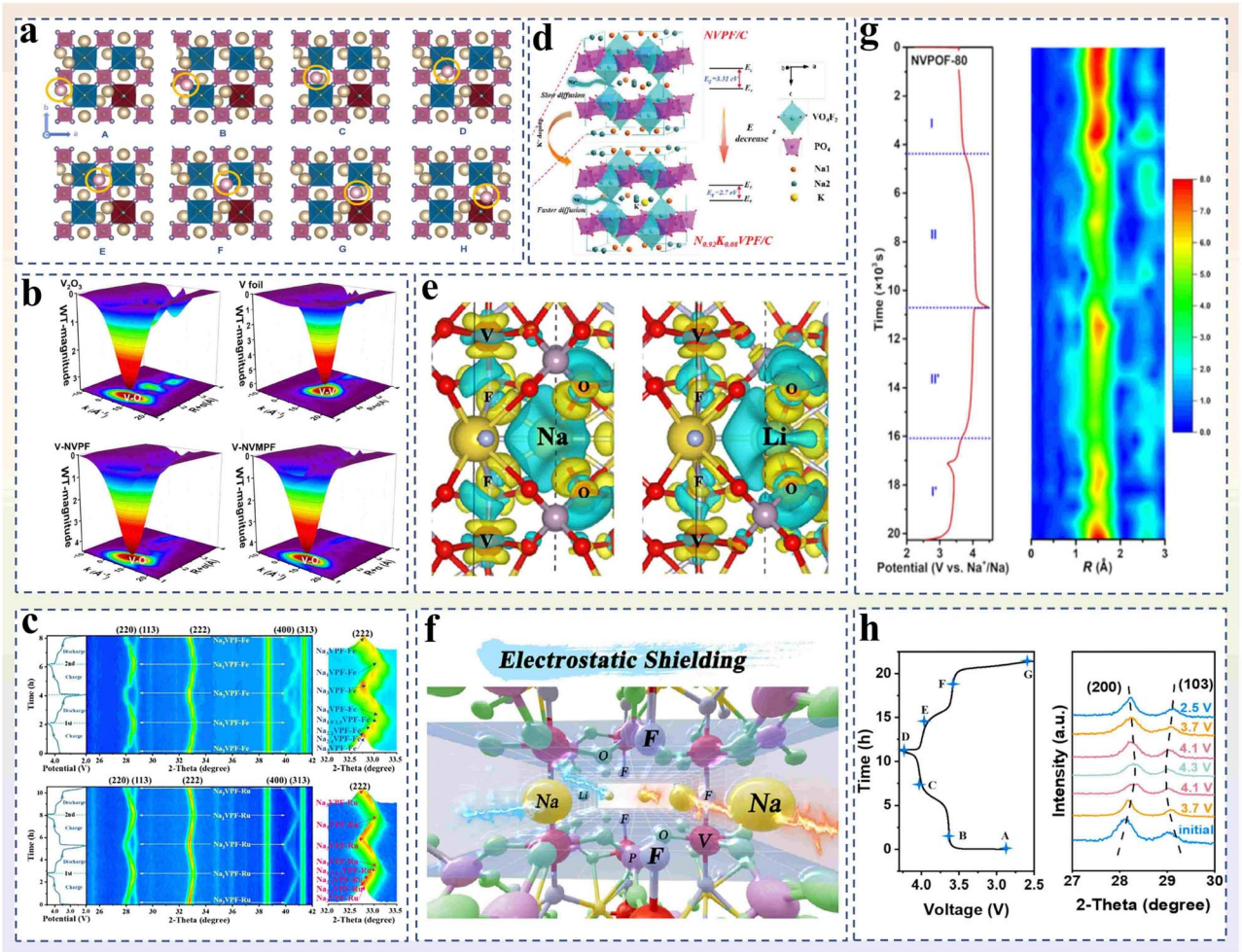

Fig. 9 (a) Na^+ diffusion pathways in NVPF-Ti-0.05.[70] Copyright 2025, American Chemical Society. (b) 3D wavelet analysis of NVMPF.[130] Copyright 2025, American Chemical Society. (c) *In situ* XRD diagram of NVPF-Fe and NVPF-Ru.[89] Copyright 2025, Wiley-VCH. (d) Scheme presenting the NVPF crystal structure, where the Na1 position is occupied by the K^+ cation, giving rise to the reduction of bandgap energy and faster Na^+ diffusion through $N_{0.92}K_{0.08}VPF$.[131] Copyright 2024, Wiley-VCH. (e) Differential charge density for NVPF (left) and 0.1Li-NVPF (right). (f) Electrostatic shielding diagram of 0.1Li-NVPF.[132] Copyright 2025, Wiley-VCH. (g) *Operando* XANES study of NVPOF-80.[133] Copyright 2025, Elsevier. (h) *Ex situ* XRD pattern with time–voltage curves of the (200) and (103) crystal planes for PA-NVPOF evaluated at 0.5 C during initial charging and discharging.[134] Copyright 2025, Elsevier.

structure, morphology, electronic properties and kinetic properties of modified wide forbidden band semiconductors were systematically investigated by using a research method combining DFT theoretical calculations and experimental tests. The comprehensive conclusion concludes that the kinetic properties of electrode materials are mainly influenced by the average particle size distribution of the nanocrystals. And the electronic properties are mainly affected by the enrichment and charge-averaging effects of doped Fe ions, which play a crucial role in the electrochemical performance of cathode materials. The bottleneck of charge transfer resistance and the diffusion coefficient of Na ions in the kinetic properties was further investigated by using *in situ* EIS test results. The sample with the optimal doping concentration achieved the highest specific capacity of 126.7 mAh g^{-1} at a rate of 0.1 C, which is close to the theoretical specific capacity of NVPF (128 mAh g^{-1}) when two Na^+ are extracted from the lattice.

Sun *et al.* proposed a high-entropy doping strategy using low-concentration multielement doping to modulate the morphology, energy band structure and coordination environment of vanadium.[130] Using a combination of systematic characterization and DFT theoretical calculations, the authors have demonstrated that high-entropy doping introduces additional energy levels into the d-orbitals of the transition metal, shrinking the band gap by nearly 1 eV and significantly improving the intrinsic electronic conductivity of the NVPF material. High entropy doping likewise led to the creation of fluorine vacancies, shortening of V–O chemical bonds, rearrangement of sodium ions at the Na3 site and shrinkage of nanoparticle grains. The above changes synergistically reduce the occurrence of deleterious phase transitions in the nanocrystal structure and improve the diffusion kinetics of sodium ions. Specifically, V K-edge X-ray absorption near-edge structure analysis was performed on samples before and after

modification. A comparison reveals that the V K-edge of the nanocrystals after high-entropy doping is significantly shifted towards higher energies, indicating a change in the local electronic structure around the V active center. A significant peak was observed near 1.5 Å, indicating that NVMPF results from a negative displacement of the peak associated with the V–O bond in the *R* space of the M–O first coordination environment. The V–O bond length is shortened after high-entropy doping, which increases the V 3d–O 2p orbital hybridization. The WT peaks of the samples were shifted to higher wave numbers after high-entropy doping compared to those of NVPF, indicating the successful doping of multiple transition metal atoms into the lattice (Fig. 9b). The results of electron paramagnetic resonance and *in situ* mass spectrometry tests indicate that the vacancies around the V site in NVMPF may be derived from elemental fluorine. The *in situ* XRD data demonstrated that the doping of high entropy ions in NVPF materials effectively suppressed the α-phase transition, thus improving the structural stability of NVPF electrodes. DFT theoretical calculations (including differential charge distributions, energy band structures, Na^+ diffusion pathway studies, and the respective diffusion energy barriers) have also been carried out in depth on the NVPF crystal model of the *Amam* space group. Ultimately, the synthesized NVMPF cathode material exhibits remarkable power density, energy density and long-term cycle stability.

In a recent study, a novel strategy of theoretical prediction-assisted chemical synthesis was proposed by Wang *et al.*[89] The changes in the band gap of various transition metal doped modified NVPFs were efficiently predicted and analyzed by means of computational simulations. Furthermore, the experimental results are reverse validated to quickly screen and filter out the suitable doping elements. A series of transition metals with 3d/4d valence electron orbitals were therefore selected and the same stoichiometric ratio was used for V-site doping of NVPF nanocrystals (NVPF-M). By theoretically calculating the differences in the density of states of various modified materials, the most suitable elements are quickly screened out. Particularly, in the elemental doping of Mn, Cu, Cd, Zn, Y, and Ag, there is no significant distribution of electron clouds at the bottom of the conduction band and between the Fermi energy levels of the V atoms, which has a small effect on the electronic structure. In contrast, the doping of Ru, Fe, Ni, Sc, Ti, Cr, Co, Zr, Nb, Mo, Tc, Rh, and Pd decreases the energy gap, which makes it easier to excite electrons from the valence band into the conduction band. Combined with the results of the electron localization function of NVPF-based materials along the (100) plane, Ru, Fe, Ni, Ti, Cr, Mn, Cu, Nb, and Cd were further selected as the representative elements doped in NVPF nanocrystals and experimentally verified (Fig. 9c). Amongst these, NVPF-Ru has the most favorable electrochemical data for the combined results and possesses the greatest application possibilities over a wide range of temperatures. Considering the combination of actual production costs and performance, the NVPF-Fe cathodes are considered to have exceptional application potential.

Like transition metal site doping, Na^+ is partially replaced by other alkali metal ions or alkaline earth metal ions, thus realizing alkali metal site doping of NVPF. The doped NVPF cathode possesses a larger sodium ion transport channel and can increase the conductivity of sodium ions. Moreover, the introduction of additional sodium vacancies in the lattice significantly improves the diffusion coefficient of sodium ions. Dopant ions with stable valence and a suitable radius can also play the role of "pillars" to stabilize the lattice structure and improve the cycling stability. Benefiting from the above advantages, Wu *et al.* introduced K ions as a doping element *in situ* to partially replace sodium ions in the NVPF cathode material (Fig. 9d).[131] The changes in the crystal structure, electronic properties, kinetic properties and electrochemical properties of NVPF after *in situ* substitution of K^+ were investigated. The *in situ* characterization revealed that the addition of heterogeneous potassium ions occupied part of the Na1 site. While the migration kinetics of sodium ions was improved, potassium ions as the "supporting framework" did not participate in the charge/discharge electrochemical behavior of the electrode. Additionally, doping of potassium ions reduces the bandgap energy of the electrode and improves the electronic conductivity. With a suitable doping amount, the larger size of heterogeneous alkali metal ions enlarges the transport channel of sodium ions, which effectively improves the overall electrochemical and kinetic properties of the electrode. Consequently, owing to this effective modification idea, the specific capacity of the prepared anode is as high as 128.8 mAh g^{-1} at 0.2 C, and still exhibits excellent multiplicity performance at 10 C. During the transport of sodium ions in NVPF cathode materials, the strong coulombic attraction of F^- and the electrostatic repulsion of adjacent sodium ions greatly reduce the performance of NVPF electrodes. In response to this situation, Lin *et al.* introduced the lithium element into alkali metal sites to regulate the electronic environment within the sodium ion diffusion channel.[132] Theoretical calculations indicate that lithium doping reduces the electron cloud density around the dangling F^- and alleviates the repulsive force between adjacent sodium ions (especially sodium ions from inactive Na1 sites) through electrostatic shielding effects. This creates a nearly neutral diffusion path, improving the migration ability of sodium ions (Fig. 9e and f). Concurrently, given the similar physical and chemical properties of lithium and sodium, lithium integrates seamlessly into the NVPF crystal lattice without triggering significant crystal phase transitions that could disrupt the stability of the crystal structure. *In situ* XRD technology was employed to reveal the crystal structure evolution of NVPF materials during charging and discharging processes, effectively demonstrating the robust structural stability of the modified cathode material. Lithium doping also disrupts the ordered arrangement of sodium ions, reducing the energy barrier for ion migration. *In situ* electrochemical impedance spectroscopy and relaxation time distribution techniques confirm that the modification reduces charge transfer resistance during sodium ion insertion/extraction. This can be attributed to the formation of a more stable and interface-compatible cathode electrolyte interface (CEI) membrane, which effectively reduces ion transport barriers and improves the kinetic performance of the electrode. Ultimately, the synergistic benefits of the above advantages have resulted in the outstanding electrochemical performance of half-cells and full cells.

In addition to the above two doping sites, further doping at the polyanionic sites likewise improves the electrochemical performance of the NVPF cathode.[135,156] The core idea is to increase the electronic conductivity by anion energy band engineering, and optimizing ion transport channels *via* modulation of lattice size. Vacancies may also be introduced through the charge compensation mechanism after heteroatom doping to modulate the chemical valence state and ultimately increase the kinetic performance of the electrode. Yu *et al.* found that structural deformation of multidimensional sodium ion transport pathways in cathode materials leads to slow sodium ion transport.[133] The authors initially defined the independently accessible sodium ion diffusion pathways in crystal structures as sodium ion diffusion degrees of freedom (df [Na^+]) and explained that higher sodium ion diffusion degrees of freedom represent superior sodium ion transport kinetics. Subsequently, the authors used the critical temperature synthesis method to prepare F-doped $Na_3V_2(PO_4)O_2F$ by performing a small amount of F/O substitution at vacant sites while maintaining the V valence state. By introducing minor perturbations into the cathode crystal structure to align the energy barriers in both directions, the intrinsic arrangement of sodium ions was disrupted, thereby broadening the df [Na^+] of the cathode. Studies using *in situ* synchrotron radiation, various spectroscopic techniques, and density functional theory simulations have shown that, compared to the slow two-phase insertion/extraction process found in traditional cathode materials, the modified cathode material with double df [Na^+] exhibits altered solid solution behavior in the first redox platform, as well as higher bonding relaxation rate in the framework (Fig. 9g). Additionally, the more prominent transition metal redox utilization and six times higher sodium ion diffusion rate have achieved unprecedented sodium storage performance (68.6 mAh g^{-1} capacity at 100 C and 98.3% capacity retention after 1300 cycles at 20 C). Gao *et al.* synthesized layered polyaniline-coated $Na_3V_2(PO_4)O_2F$ nanoparticles through elemental doping at polyanionic sites, achieving this under solvothermal conditions below the temperatures required for high-temperature sintering.[134] *Ex situ* XRD analysis indicates that the prepared cathode material undergoes a two-phase reaction during charging and discharging ($Na_3V_2(PO_4)O_2F \leftrightarrow Na_2V_2(PO_4)O_2F$; $Na_2V_2(PO_4)O_2F \leftrightarrow NaV_2(PO_4)O_2F$) and achieves highly reversible structural evolution (Fig. 9h). The $Na_3V_2(PO_4)O_2F$ cathode obtained through *in situ* aniline polymerization exhibited a high average operating voltage of 3.69 V (*vs.* Na^+/Na), high-rate capability of 65.3 mAh g^{-1} at 10 C, excellent reversible specific capacity of 129.5 mAh g^{-1}, and high energy density of 478 Wh kg^{-1}.

To further enhance the effectiveness of modification strategies, researchers often adopt the method of simultaneously doping polyanion sites with multiple sites to obtain the maximum synergistic effect. Given the dynamic effects of electrostatic interactions and sodium ion ordering on polyanion cathodes, Yu *et al.* decoupled these two intertwined factors and conducted relevant research.[136] This allowed them to clarify the respective roles and dominant factors of each, thereby realizing the electrochemical potential of phosphate-based cathode materials. Researchers synthesized cathode materials doped with Zn^{2+} or Mg^{2+}. Crystal structure characterization and theoretical calculations revealed that introducing a small amount of Zn^{2+} (accounting for 0.6% of the sodium content) into sodium sites, accompanied by sodium vacancies, could form a stable crystal structure. Correspondingly, when Mg^{2+} is co-doped at sodium and vanadium sites at ten times the above Zn^{2+} content, this will introduce additional sodium ions to achieve charge balance. Performance testing shows that Mg^{2+}-doped polyanion cathode materials exhibit a sodium ion diffusion coefficient up to three times higher than that of Zn^{2+}-doped control materials, significantly improving their sodium storage performance, despite the need to overcome a larger ionic repulsion energy barrier. This work confirms that, in such material systems, regulating structural order through doping strategies is an effective way to optimize the defect formation energy of phosphate-based cathode materials, and this advantage can be extended to other polyanion cathode materials. In a similar manner, Wang *et al.* introduced Fe^{3+} and fluoride ions into the polyionic cathode in a quantitative manner and synthesized the cathode material $Na_3V_{1.84}Fe_{0.16}(PO_4)_2F_3$ ($x = 0.16$).[137] The introduction of heterogeneous impurity atoms significantly reduces the original band gap and energy barrier of the cathode material, as confirmed by density functional theory calculations. A series of experiments were conducted to elucidate the sodium storage mechanism associated with the three-phase transition of the prepared nano-positive electrode material. When the material with a doping concentration of $x = 0.16$ is used as the cathode material for sodium-ion batteries, the diffusion coefficient of sodium ions is significantly enhanced, exhibiting lower activation energy. Therefore, the assembled battery has excellent dynamic and electrochemical performance. It takes only 2.39 minutes to fully charge at a current density of 10 C, while maintaining low energy loss in various rigorous self-discharge tests. In addition, the low intrinsic electronic conductivity caused by PO_4^{3-} severely hinders the practical application of NVPF cathodes. Zhou *et al.* simultaneously doped F^- and PO_4^{3-} at the polyanion sites, obtaining $Na_3V_2(PO_4)_{1.95}(SiO_4)_{0.05}O_2F$.[138] Combining theoretical calculations and experimental testing analysis, this dual anion substitution doping strategy optimizes the material's electronic conductivity while widening the sodium ion transport channel, synergistically promoting improvements in ion/charge diffusion kinetics. Plus, the SiO_4^{4-} groups that were added make the crystal structure more stable, which helps with reversible two-electron reactions and boosts energy density by increasing the average discharge voltage. Therefore, the prepared nano-sized cathode material exhibits significantly improved high-rate performance (75.5 mAh g^{-1} at 30 C) and shows almost no capacity decay after 1000 cycles at 10 C. When assembled into a full cell with a hard carbon anode, the cathode achieves high energy density (280 Wh kg^{-1}) and exceptional long-term cycling stability (92.3% capacity retention after 300 cycles at 5 C).

4.2 Nanostructure/crystalline face modulation

As an effective means of nanostructure tuning, the nanolattice structure could be modulated by heterostructure complexation.

This also could be realized by regulating the exposure and growth of the dominant crystalline surfaces. In order to contribute to a better solution to the problems faced by NVPF nanomaterials, the kinetic properties of the electrode materials are improved by means of rational modifications to optimize the electron/charge transport paths, shorten the transport distances and lower the energy barriers.[139–141] The effective exposure and growth of high-energy crystalline surfaces enhances the reaction between suitable chemical bonds and functional groups to promote the generation of dominant structures. Nanostructure optimization might also be used to reduce the bulk strain during ion transport and suppress the generation of vacancies from undesired lattice distortions.

Xie *et al.* composited NVPF with $LiNi_{0.8}Co_{0.1}Mn_{0.1}O_2$ (NCM811), a common LIB cathode, and realized a high-performance cathode material through the nano-structural modulation between the two conformational materials.[142] The modified materials were subjected to *ex situ* XRD testing. Based on the analysis of the plots of the composites at different voltages, we can find that the characteristic diffraction peaks shift from the space group *Amam* to I_4/mmm in the charging state of 4 V. Upon further charging to 4.3 V, the crystal structure was transformed into the $Cmc2_1$ space group (Fig. 10a). A completely opposite diffraction peak shift process was demonstrated upon discharge, proving the structural stability of the nanocrystalline material. Besides, the introduction of NCM811 brings about an earlier voltage shift and improves the discharge plateau voltage of the cathode material. Meanwhile, other test results illustrate that the modified composite material stores and releases more energy during the charging/discharging process, which ultimately leads to an increase in the specific energy of the cathode material. The EIS of the modified cathode is significantly reduced and the diffusion coefficient is improved. The improved kinetics ultimately enhances the rate performance and long-term cycle stability of the battery. Zhao *et al.* introduced polytetrafluoroethylene and $Na_3V_2(PO_4)_3$ into NVPF, thereby forming a two-phase $Na_3V_2(PO_4)_3$/NVPF heterostructure.[90] X-ray absorption fine structure (XAFS) indicates that the prepared composite heterostructure cathode exhibits a lower V valence state, thereby releasing more reversible capacity. The shorter V–O bond allows the VO_6 octahedron to maintain a stable crystal structure. Nuclear magnetic resonance proves that the additional Na sites in NVPF in the cathode are activated, indicating that more active sodium ions participate in

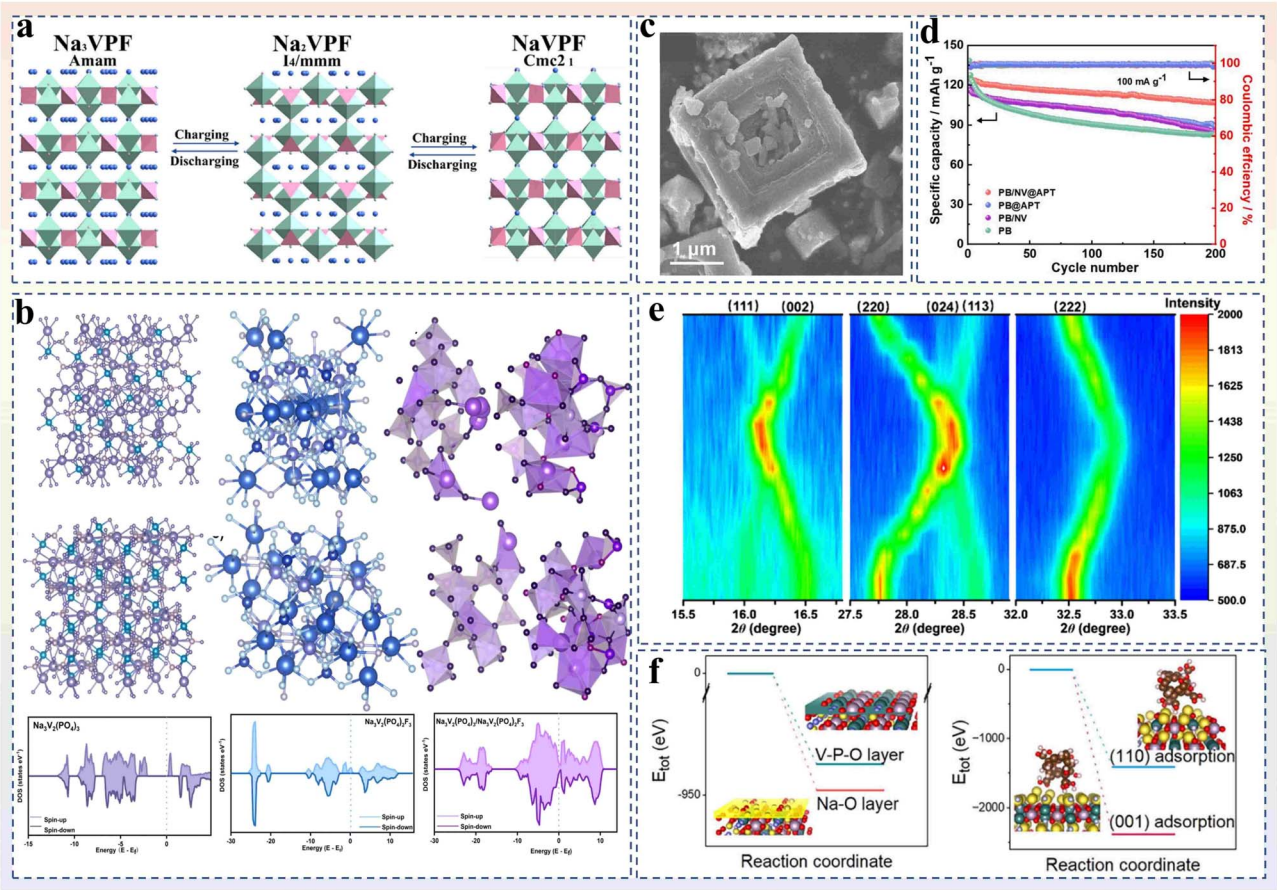

Fig. 10 (a) Structural evolution of NVPF during the charging and discharging processes.[142] Copyright 2025, Elsevier. (b) Schematic crystal structures (top) and density of states (bottom) of $Na_3V_2(PO_4)_3$ (left), $Na_3V_2(PO_4)_2F_3$ (middle) and $Na_3V_2(PO_4)_3$/$Na_3V_2(PO_4)_2F_3$ (right).[90] Copyright 2025, Elsevier. (c) SEM image of PB/NV@APT. (d) Cycle performance of PB, PB@APT, PB/NV, and PB/NV@APT at 100 mA g^{-1} and 1 A g^{-1}, respectively.[143] Copyright 2025, Elsevier. (e) Contour plots of *in situ* XRD results.[144] Copyright 2024, American Chemical Society. (f) Adsorption energy and schematic diagram.[145] Copyright 2024, Royal Society of Chemistry.

the electrochemical reaction, improving the specific capacity of the cathode. The two extended and reversible charging platforms above 3.7 V and a merged discharging platform in the charge–discharge curve also confirm the improvement in specific capacity and energy density. *Ex situ* XRD and XPS were used to comprehensively study the evolution of the crystal structure and charge compensation mechanisms, further demonstrating the advantages of the NVPF composite cathode in terms of high electrochemical reversibility and near-zero structural strain. Meanwhile, *ex situ* high-temperature XRD revealed the intrinsic formation mechanism of the NVP/NVPF heterostructure. Due to the work function difference between $Na_3V_2(PO_4)_3$ and $Na_3V_2(PO_4)_2F_3$, a self-enhanced built-in electric field is constructed at the heterointerface to achieve accelerated transport of electrons and ions. The self-enhanced built-in electric field of the heterostructure, which regulates the multi-electron reaction of the electrode, was also demonstrated by combining density of states theory with various testing and characterization methods (Fig. 10b). As a result, the prepared heterostructure composite NVPF cathode exhibited an ultra-high specific capacity of 139.8 mAh g^{-1} and excellent rate performance and cycling performance.

Wang *et al.* successfully prepared a nanocrystalline material of a Prussian blue composite with NVPF and used it as a cathode for SIBs (PB/NV@APT).[143] Nano-structural modification enhances the average operating voltage of the cathode material and improves the electrochemical performance. SEM and TEM were used by the authors to observe the morphology and microstructure of the prepared nanocrystals. As shown in Fig. 10c, the morphology of PB/NV@APT is a nano-cube with layered hollow cavities. The unique cavity structure provides more channels and active sites for the exchange of sodium ions, thus improving the charging and discharging performance of the positive electrode. Meanwhile, the test results of measured tap density show that the modified nanocrystalline materials exhibit significantly enhanced tap density. This shows that more volume of the active material can be filled in a limited battery space, thus increasing the volumetric energy density of the battery. Owing to the above unique design, the reversible charge/discharge specific capacity and cycle stability of the modified electrode are significantly improved. At a current density of 100 mA g^{-1}, the electrode provides an initial capacity of 124.9 mAh g^{-1} and has a capacity retention of 85.7% after 200 cycles (capacity decay is one-third of that before modification) (Fig. 10d). Also, Kumari *et al.* proposed a method to prepare a high-performance composite cathode by co-sintering NVPF and the sodium super-ionic conductor ($Na_3Zr_2Si_2PO_{12}$, NZSP) at high temperature, which was successfully applied to all-solid-state sodium batteries.[158] The modified composite cathode can establish tight contact between the cathode active substance and the electrolyte while maintaining interfacial stability (chemical, thermal and electrochemical). XRD and SEM confirmed that the heterogeneous composite modified cathode material has no obvious elemental diffusion and has good structural stability. The co-sintering step also significantly reduced the interfacial resistance at the NZSP/NVPF interface. Finally, the design and assembly of the full cell was carried out, and the constructed full cell had 85% capacity retention and 99% coulombic efficiency after 500 cycles at 0.1 C. To address issues such as poor electronic conductivity, slow reaction kinetics, and large volume changes during charging and discharging inherent in NVPF cathodes, Ma *et al.* intentionally added a certain amount of pretreated multi-walled carbon nanotubes during the preparation process.[144] A one-pot solid-state reaction method was used to synthesize a biphasic polyanion phosphate material composed of NVPF and a small amount of NVP. Benefiting from the structural superiority brought about by heterostructure modification, the improved electronic conductivity and kinetic performance of the cathode material achieved remarkable cycle stability and significant charge–discharge performance. The composite electrode exhibits capacities of 114.8 and 78.6 mAh g^{-1} under test conditions of 20 and 5000 mA g^{-1}, respectively, and retains 75.7% of its capacity after 10 000 cycles. *In situ* XRD test findings confirm that the NVPF composite cathode maintains a stable crystal structure during sodium ion insertion and extraction, and its excellent structural reversibility contributes to the electrode's long cycle life (Fig. 10e). Even more importantly, this dual-phase heterogeneous cathode material also exhibits surprising electrochemical performance across a wide operating temperature range of −20 to 50 °C, driving further practical applications.

Furthermore, facilitating the exposure of dominant active crystalline surfaces by means of nano-structural modification is also an effective measure to enhance the performance of NVPF nanocrystal electrodes. Li *et al.* synthesized NVPF with different (002) active surface exposure rates, in which the surface energy is regulated by using carbon clusters as inducers, ultimately controlling the growth rate of different crystal surfaces.[145] The differences in crystal morphology are generally considered to be mainly due to the anisotropy of crystalline materials. During the growth of crystals, the growth rate of crystal faces with high surface energy is faster than that of low surface faces, leading to the optimal growth of crystalline materials. The researchers analyzed the growth mechanism of NVPF nanocrystals under the adsorption of carbon clusters using DFT theoretical calculations with relevant test predictions (Fig. 10f). Further theoretical studies of Na^+ adsorption, diffusion, and storage indicate that the exposed (002) crystal faces have more stable Na^+ storage sites, which results in lower energy barriers for the Na^+ diffusion process. A combined analysis of synchrotron X-ray absorption spectroscopy and electrochemical tests further elucidated the promotion of enhanced Na^+ transport kinetics and associated electrochemical stability.

4.3 Dual-modification strategies

The performance improvement of NVPF nanocrystalline by using single nano-engineering strategies is of limitation. The dual modification approach combining nanoscale surface modification with nano-structural modification provides more flexible design strategies, more significant results and greater application potential.[64,146–152,157] Iron-doped NVPF was prepared by a hydrothermal method by Yang *et al.*[77] The introduction of iron is beneficial in reducing the agglomeration phenomenon of particles and refining the cathode nanoparticles. The transfer of Na^+ was further facilitated, and the irreversible degradation

of the nanocrystal structure was mitigated. Simultaneously, benefiting from the establishment of a three-dimensional carbon framework constructed by using N-doped carbon nanotubes and carbon layers, a protective layer was formed around the NVPF material, which reduces the excessive changes in the lattice volume during the charging and discharging process. The carbon protective layer also acts as a conductive network to further enhance the electron transfer capability of the cathode material (Fig. 11a). Batteries assembled with modified electrodes achieved 98% capacity retention in rate performance tests from 0.1 C to 10 C. Zhou *et al.* proposed a strategy to synthesize copper-substituted NVPFs with a unique yolk–shell structure by the spray-drying method.[80] In parallel, a nitrogen-modified carbon coating (polyvinylpyrrolidone as the carbon source) was applied on the surface of NVPF. Improvement of intrinsic and interfacial conductivity in NVPF nanocrystals was observed by synergizing nanoscale surfaces engineering and nanocrystal structural tuning. The structural evolution of the modified electrode during the electrochemical reaction was investigated in real time using the *in situ* XRD technique (Fig. 11b). The characterization results illustrate the presence of interphase changes in the cathode material during cycling, following a reversible sodium-ion storage and removal mechanism multiphase change, rather than a solid-solution-reaction mechanism. DFT theoretical calculations predict that the substitution of copper introduces new impurity energy levels in the band gap, allowing electrons in the valence band to easily jump to the conduction band, ultimately increasing the intrinsic conductivity of NVPF (Fig. 11c). The optimized cathode with an egg yolk shell structure provides 117.4 mAh g^{-1} at 0.1 C with ultra-high cycling stability.

Guo *et al.* synthesized a series of scandium-doped $Na_3V_{2-x}Sc_x(PO_4)_2F_3/C$ materials using the sol–gel method.[153] This strategy aims to improve the electrochemical performance of NVPF cathodes and modify their surface using citric acid as a chelating agent and carbon source, which improves their

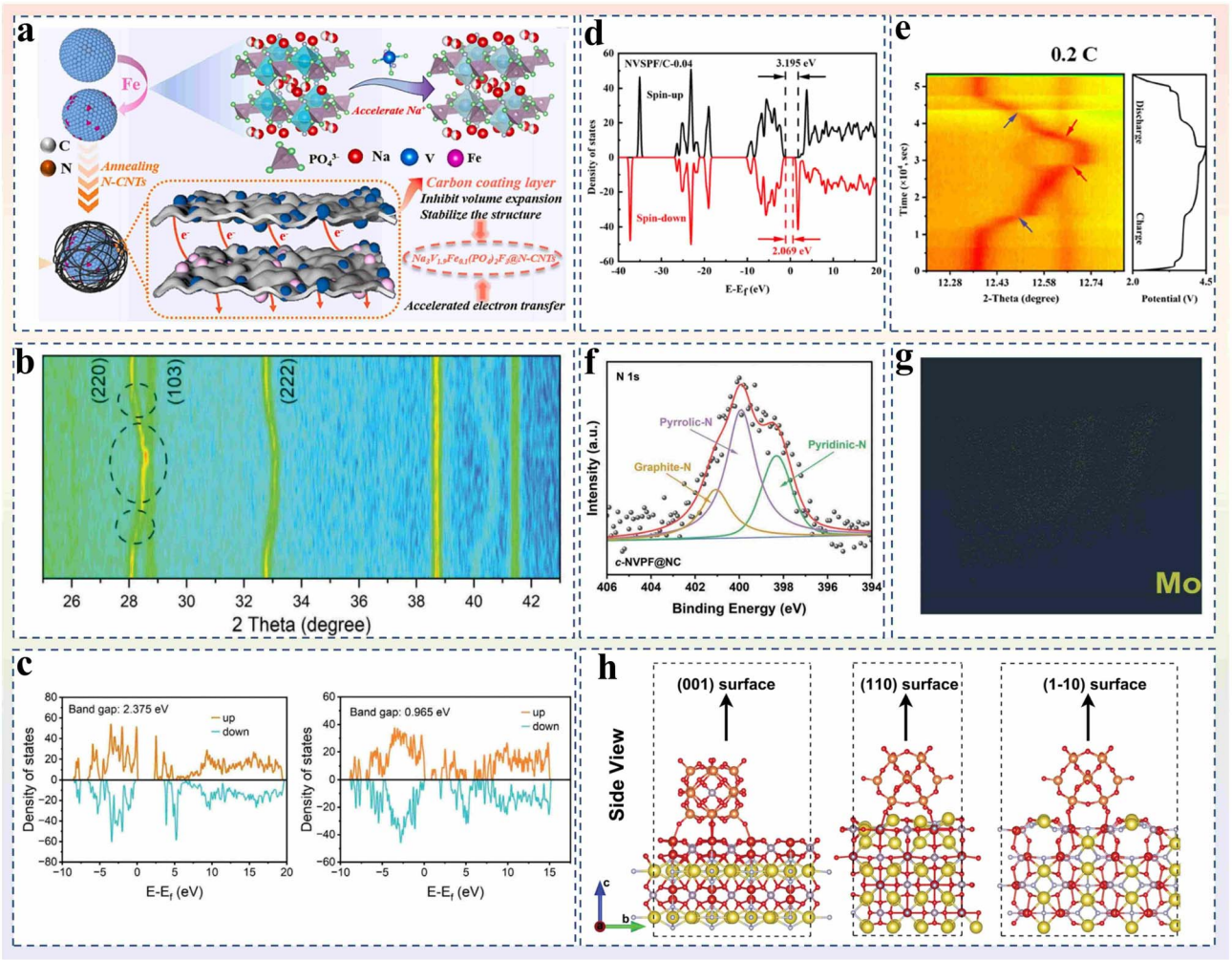

Fig. 11 (a) Synthesis schematic of $Na_3V_{1.9}Fe_{0.1}(PO_4)_2F_3$@N-CNTs.[77] Copyright 2024, Elsevier. (b) *In situ* XRD spectrum of NVPF with copper replacing vanadium element. (c) Density of states of NVPF and modified NVPF.[80] Copyright 2024, Wiley-VCH. (d) Density of states calculations for NVSPF/C-0.04. (e) 2D contour plot showing the evolution of the reflections at around 12° 2θ with the corresponding GCD curve at 0.2.[153] Copyright 2025, American Chemical Society. (f) High-resolution N 1s and (g) Mo fragments obtained by TOF-SIMS. (h) PMA adsorption on the (0 0 1), (1 1 0), and (1–1 0) surfaces.[75] Copyright 2023, Wiley-VCH.

electronic conductivity. Research has found that, compared with V, Sc is more environmentally friendly. As a non-electrochemically active element, Sc partially stabilizes the crystal framework, reduces crystal deformation during the sodium ion insertion/extraction process, improves ion diffusion in the material, and reduces polarization. The optimized NVPF electrodes exhibit favorable electronic conductivity and cycling stability, with the NVSPF/C-0.04 electrode demonstrating the highest discharge specific capacity, remarkable rate performance, and cycling stability. Density functional theory results indicate that the band gap of the modified electrode is significantly reduced, suggesting that the electron transport capability from the valence band to the conduction band in Sc-doped NVPF is significantly enhanced, confirming that Sc doping effectively improves the intrinsic electronic conductivity of the homogeneous phase of NVPF (Fig. 11d). *In situ* XRD data indicate that the modified electrode undergoes a phase transition during charging/discharging at 0.2 and 2 C and reveals the reason for the capacity decline at 5 C (Fig. 11e). Finally, the full battery matched with hard carbon exhibited outstanding discharge specific capacity (112 mAh g^{-1} at 1 C).

The rational use of a variety of modification methods often achieves unexpected results. Liang *et al.* developed a phosphomolybdic acid-assisted hydrothermal synthesis of NVPF.[75] The morphology of NVPF nanocrystals changed with the addition of phosphomolybdic acid as an inducer of crystalline facets under van der Waals forces using phosphomolybdic acid, and the surface was covered with a nitrogen-doped carbon nano-interface layer. XPS spectroscopy revealed distinct N 1s and C 1s peaks, confirming the formation of an N-doped carbon layer on the NVPF electrode (Fig. 11f). Moreover, a three-dimensional view of the modified NVPF was obtained by time-of-flight secondary ion mass spectrometry, showing a large amount of V and Na ions, as well as trace amounts of Mo ions diffusing throughout the entire bulk phase (Fig. 11g). Although the content is low, the presence of Mo is still observed in the test results, indicating that phosphomolybdic acid is evenly distributed in NVPF. The effect of the structure and morphology of NVPF nanoparticles on electrochemical properties was investigated using comprehensive characterization and testing. In addition, the impact of the introduction of phosphomolybdic acid on the molding of NVPF was analyzed using DFT theory calculations (Fig. 11h). It is predicted from the theoretical calculations that the addition of the facet inducer leads to faster NVPF crystal growth due to the increased adsorption energy and increased surface energy. As a result, rectangular NVPF grains with a continuous diffusion path of Na^+ are formed. Also, kinetic performance tests showed that the nano-interfacial layer prepared by the coating process improved the electron and ion transport capacity of the cathode. Ultimately, this combined approach of nanocrystal structure modulation and nano-surface modification yielded enhanced electrochemical properties of the cathode material. Carbon-coated, magnesium ion-doped NVPF (labeled $Na_3V_{2-x}Mg_x(PO_4)_2F_3$@C) was synthesized by a facile sol–gel method by Zhang *et al.*[154] The effects of the modified NVPF crystal structure and electrochemical properties were comprehensively investigated by means of comprehensive characterization experiments and electrochemical tests. The moderate introduction of magnesium ions leads to an equal amount of V^{3+} being compensated for by V^{4+} charge, which improves the extra capacity and voltage plateau of the electrode. In addition, the doping of magnesium ions reduces the aggregation effect during the preparation of the material, shortens the bond lengths of the V–O and V–F bonds, reduces the cell volume, and creates a more stable channel for the transport of sodium ions in NVPF. The synergistic effect of the disordered carbon layer on the surface provides more paths for the transport of sodium ions, improves the electronic conductivity of the surface, effectively reduces the electrode polarization phenomenon and charge transfer impedance during the charging and discharging process, and ultimately enhances the comprehensive performance of the material. The $Na_3V_{1.95}Mg_{0.05}(PO_4)_2F_3$@C sample has a specific capacity of 126.8 mAh g^{-1} at 0.1 C and an impressive 96.72% capacity retention after 100 cycles. At 10 C, the initial discharge capacity is 102.3 mAh g^{-1}, with 70% retention after 1000 cycles and an overall cycle life of over 2000 cycles. Wang *et al.* introduced potassium and magnesium elements in NVPF nanocrystalline particles possessing nitrogen-doped carbon protective coatings using a binary co-doping strategy.[155] Materials modified with nanoscale interfacial layers not only form a porous structure but also introduce additional defects and active sites. This modification improves the reaction kinetics and simplifies the electrochemical process by increasing electrolyte interactions through the enlarged specific surface area. A two-element doping strategy targeting NVPF nanocrystals acts on both alkali and transition metal sites. The introduction of potassium ions with a larger radius enlarges the transport channel for sodium ions, which facilitates the transport of sodium ions and improves the reaction kinetics. The substitution of magnesium ions in the V sites creates holes and improves the electronic conductivity of the material. Meanwhile, the inactive magnesium ions significantly inhibit the occurrence of lattice distortion and improve the cycling stability of the electrode.

The integrated design of nanoscale interfacial and structural modification offers a promising route for addressing the inherent challenges of NVPF electrodes. On one hand, refined nanostructuring shortens ion transport distances. On the other hand, interfacial coatings optimize charge transfer, reduce fluorine loss, and suppress side reactions. Together, these modifications stabilize the lattice structure, accommodate nanoscale volume fluctuations, and improve overall cathode stability. Nevertheless, critical obstacles persist: kinetic limitations impede Na1 site activation essential for enhanced energy density; irreversible phase transitions driven by high-valence vanadium upon deep desodiation remain unaddressed; and the economic viability of exogenous modifications must be carefully evaluated.

5 Summary and prospects

In summary, various advanced nanotechnologies were employed to promote the interfacial stability, bulk structure and electrochemical performance of polyanionic cathodes for

SIBs, contributing to great progress from the perspectives of both basic research and industrial applications in this field, which can be well evidenced by the increasing publications in the past few decades (Fig. 12a).[159–161] We further conducted research hotpot analysis by selecting core keywords in public databases, typically including nanotechnology engineering, cathode materials, polyanionic phosphates and electrochemical performance parameters related to SIBs (Fig. 12b), which confirms the extensive research interests and will expand research direction space in the future.

Specifically, polyanionic NVPF serving as a cathode can deliver a high working voltage and large reversible capacity, and is regarded as one of the most promising cathodes for SIBs. However, the intrinsic structure deficiency, low electronic conductivity, sluggish Na^+ kinetics, structural deterioration and serious side-reactions during high-cut-off-voltage cycling finally contribute to unsatisfactory rate capability and cycling stability.[162] It is of significant importance to overview the previous research progress and current application prospects of NVPF. Therefore, we systematically reviewed the intrinsic structure properties, synthesis routes, the remaining challenges and the nanoengineering modification strategy of NVPF-based cathodes toward practical SIBs. We especially focus on nanostructure design, physical characterization, electrochemical mechanisms, and practical application, which can render an elucidation of the relationship between the structure and performance and advance commercialization of NVPF cathodes. Meanwhile, for nanotechnology engineering, through rational multidimensional nanoscale electronic structure regulation, conductive network construction, and micro-nano structure design, scientists have made progress in addressing key challenges with NVPF, including its poor intrinsic electronic conductivity and structural irreversibility. The purpose of this review is to identify the commonalities and special features of these outstanding achievements and to inspire more researchers to conduct relevant research. Despite some exciting breakthroughs having been achieved, three perspectives are presented from the perspective of nanotechnology engineering to further improve the comprehensive performance of NVPF cathodes for practical SIBs in the future (Fig. 13).

(1) *Advanced auxiliary research tools*: at present, the research approach of combining theoretical calculations and experimental testing analysis has become widely used. Therefore, more advanced research tools are needed to conduct in-depth research on NVPF materials, thereby solving key issues related to electrode materials and improving their overall performance. The development of advanced research tools for the future broadly includes multidimensional dynamic characterization techniques, multiscale computational simulations, and machine learning-driven multidirectional design.

Innovations in multidimensional dynamic characterization techniques mainly include *in situ* structural analysis techniques and dynamic visualization engineering of three-dimensional structures and element distribution, for example, by combining *in situ* XRD, *in situ* TEM, and *in situ* selected area electron diffraction analysis to conduct in-depth research on the actual structural evolution process of NVPF cathode materials under operating conditions. Concurrently, *in situ* spectroscopic techniques such as *in situ* Raman spectroscopy and *in situ* solid-state nuclear magnetic resonance spectroscopy provide detailed analysis of changes in functional groups and chemical bonds during nanoengineering modifications. The further development of X-ray computed tomography and X-ray energy-dispersive imaging techniques has also advanced researchers' understanding of nanoscale structural evolution and elemental valence state changes within electrodes.

With the deepening development of simulation computing capabilities, multi-scale simulation methods have become a key

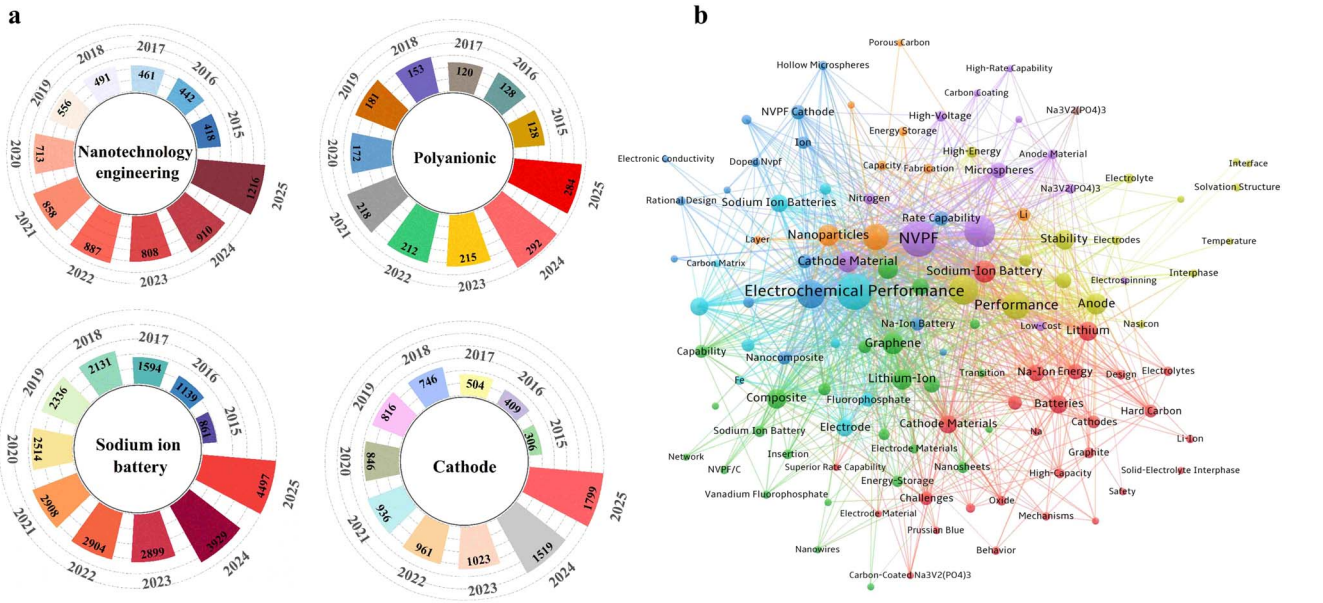

Fig. 12 (a) A statistical chart showing the number of publications in the relevant field over the past 10 years. (b) Research hotspots in the NVPF cathode of SIBs.

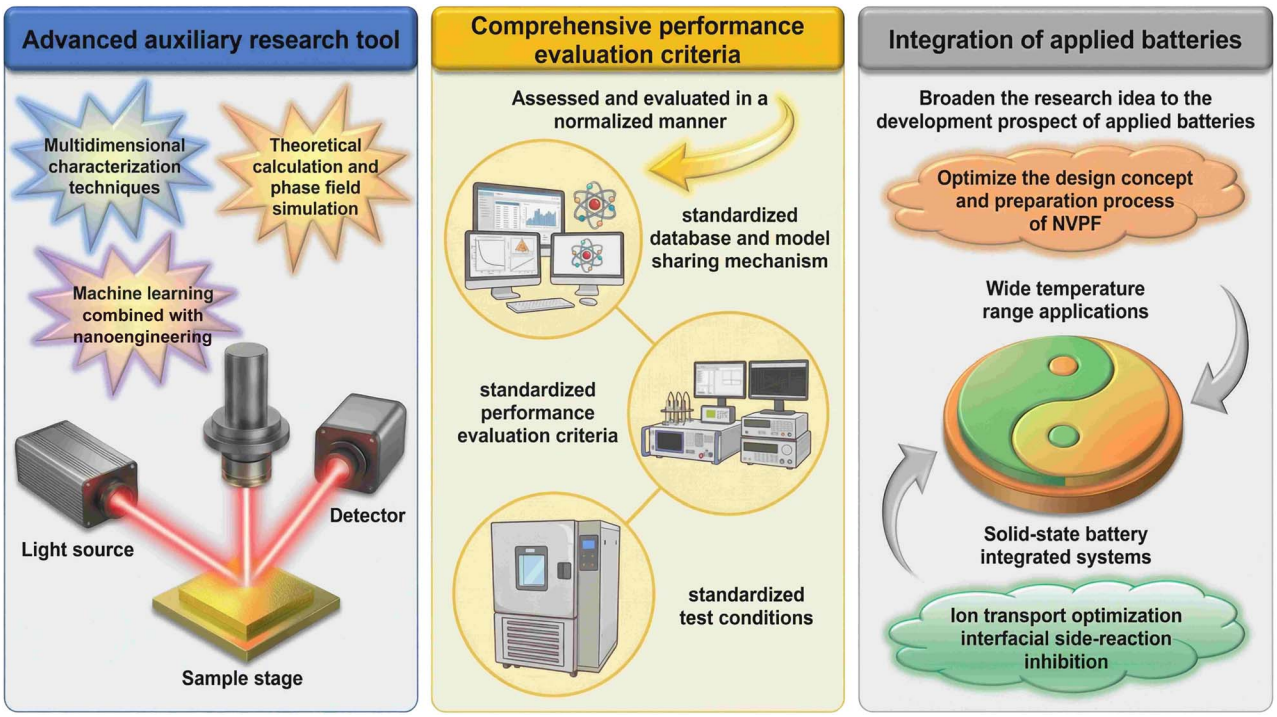

Fig. 13 Future outlook for NVPF nanotechnology engineering development: examples and schematic diagrams (left, center, and right represent advanced auxiliary research tools, comprehensive performance evaluation criteria, and integration of applied batteries, respectively).

tool for revealing the intrinsic characteristics and performance optimization mechanisms of NVPF materials. The core of this method lies in the deep integration of atomic-scale calculations and macroscopic phase field simulations. By connecting density functional theory, first-principles molecular dynamics, and phase field simulations, it is possible to predict the changes in NVPF electrodes from the atomic orbital to the macroscopic structural stress in a manner that is closer to reality. Thus, it is possible to verify or predict the results of subsequent experimental tests, thereby achieving more effective NVPF cathode nanoengineering modification.

Besides, the traditional "trial and error" research model is being replaced by big data-driven research, and machine learning is driving closed-loop optimization from theoretical prediction to experimental verification in the nanoengineering design of NVPF materials. By establishing a materials genome engineering network, high-throughput screening will be achieved from "input feature values" to "performance result predictions," ultimately realizing "reverse analysis and multi-directional design," which will greatly improve the efficiency of scientific research work. Furthermore, by optimizing algorithms and adjusting spatial parameters in combination with active learning strategies, the material synthesis pathway is ultimately optimized, enabling high-efficiency synthesis pathway analysis with "intelligent navigation". In summary, the development of advanced research tools is profoundly transforming the research paradigm of NVPF and other materials, enhancing the depth and scope of research.

(2) *Comprehensive performance evaluation criteria*: in the study of NVPF cathodes, there are phenomena such as "differences in electrolyte systems, differences in voltage windows and test conditions, differences in the threshold settings of specific parameters in the material characterization process, and arbitrariness in full cell matching". In response to the issues of fragmented testing methods, poor comparability of experimental data, and an incomplete evaluation system in the aforementioned basic scientific research, it is necessary to establish standardized comprehensive performance evaluation criteria for related research to better apply NVPF cathodes in future actual production.

Specifically, for the electrolyte systems that are currently being studied (ester electrolytes, ether electrolytes, and new fluorinated solvents), it is necessary to establish a unified performance comparison benchmark. In addition, the type of solvent in the electrolyte, the concentration of sodium salt, and the proportion of additives also have a significant impact on battery performance. Research on different electrolytes for different applications can also be managed using standardized databases, which will facilitate further studies on NVPF-based sodium-ion batteries in the future. Also, the voltage window and test temperature benchmarks should be set in a standardized way. As we know, the charge–discharge behavior of electrode materials like NVPF is really sensitive to voltage and temperature. For battery testing, parameters like "voltage window, temperature gradient, and high-rate polarization compensation" need a benchmark to guide future performance comparison studies. At the same time, electrochemical and other basic test program parameters also require a standardized protocol to guide research, thereby making the data obtained more comparable, for example, in constant current charge–

discharge tests in electrochemical testing, the requirements for setting the cycle activation stage and cycle stage, in electrode structure characterization, the critical point of structural phase transition, the threshold for fluorine loss, and parameters for structural integrity after cycling, *etc.* The matching of the full battery is highly dependent on the choice of the anode. For the type of anode, the choice of anode precursor, the pre-sodiation process, and the control of the N/P ratio all require a standardized scheme for effective full battery performance evaluation. Only by setting standardized test conditions or standardized performance evaluation standards can the true effective performance of NVPF-type batteries be more clearly reflected.

Furthermore, establishing standardized databases and model sharing mechanisms will also help accelerate the industrialization process. For example, a dedicated database for NVPF materials could be constructed, including a "material gene" library, performance degradation charts, and failure case analysis data collection. Simultaneously, performance prediction models based on standardized data collection will be developed to enable prediction and analysis of the results of NVPF cathode material nano-interface modification and nanostructure modification, thereby further improving the research efficiency of scientists. In this way, the industrialization assessment system and standard formulation will be promoted.

(3) *Integration of applied batteries*: except for focusing on improving the intrinsic properties of NVPF-type cathode materials, it is also necessary to broaden the research scope to include the development of application-oriented batteries (including solid-state batteries, wide-temperature-range batteries, and multi-scenario integrated applications), thereby achieving a transition from modified nanotechnology to solving macro-level scientific problems. In integrated solid-state battery systems, contact issues at solid–solid interfaces (electrode interface–electrolyte interface) have long been a major challenge for researchers. Poor physical contact between solid interfaces leads to a shift from the original "surface contact" to partial "point contact" on the electrode side. The micron- and nanometer-scale gaps between interfaces result in the formation of uneven inert layers at the electrode interface, which negatively affects the electrochemical performance of the battery. Furthermore, the expansion coefficients of the two solid interfaces are typically mismatched. This leads to issues such as interface separation during cycling, which causes battery failure. So, for the future development of solid-state batteries, it's really important to optimize the composite electrolyte and interface layer together and control the ion behavior at different scales (like controlling the electric field and ion concentration gradient).

The design strategies for wide-temperature-range batteries mainly include improving the intrinsic stability of materials, matching the interface chemistry of wide-temperature-range electrolytes, and studying the failure mechanisms and regeneration strategies at extreme temperatures. Currently, NVPF materials are constrained by both ion diffusion retardation and decreased interface stability at low temperatures. First, further improving the intrinsic structural stability (low temperature/high temperature) of NVPF electrode materials through appropriate nanoengineering modification is the fundamental way to enhance their wide temperature range application. Second, attention should also be paid to the interface chemistry matching with wide temperature range electrolytes, and the relationship between the physical and chemical properties of the interface CEI and its electrochemical performance should be studied. Finally, the failure mechanism at extreme temperatures and the regeneration/repair strategies for failed cathode materials should also be given attention.

Further development of NVPF electrodes should also consider their application in multi-dimensional integrated application systems. NVPF electrodes modified through nanoengineering offer advantages such as high voltage, long cycle life, and economic versatility. As a supplementary energy storage device, NVPF electrodes will help promote the development of grid-level energy storage systems, special power supplies (for special vehicles, aerospace applications, *etc.*), and economical electric vehicles.

In the future, the nanotechnology engineering of NVPF cathodes will be guided by the principles of "atomic-level precision control, multi-nano-scale coordination, deepened understanding of mechanisms, and scalable application. The practical application of NVPF cathodes from laboratory research to actual implementation should be advanced. Furthermore, the universal application of nanotechnology engineering to other energy storage fields should be extended, adapting to local conditions to achieve more breakthroughs.

Author contributions

Jiahao Chen: conceptualization, literature curation, writing – original draft. Xingjie Wu: literature curation, methodology, data analysis. Zhiyong luo: methodology. Xinxian Ren: data analysis. Junhao Chen: methodology. Minjie Chen: project administration, data analysis. Chunliu Xu: manuscript revision, funding acquisition, supervision. Yao Xiao: supervision, manuscript revision. Weiqing Yang: supervision, funding acquisition.

Conflicts of interest

The authors declare no conflict of interest.

Data availability

No primary research results, software or code have been included and no new data were generated or analyzed as part of this review.

Acknowledgements

The authors acknowledge the financial support provided by the National Natural Science Foundation of China (22309203 and 52372228), the Sichuan Science and Technology Program (2025ZNSFSC0364), the Fundamental Research Funds for the Central Universities (2682025CX145), the China Postdoctoral Science Foundation funded Project (2025T180291 and 2024M762671), and the Student Research Training Program (SRTP) Project (202510613060).

References

1 M. Zheng, Y. You and J. Lu, Understanding materials failure mechanisms for the optimization of lithium-ion battery recycling, *Nat. Rev. Mater.*, 2025, **10**, 355–368.

2 H. Ji, J. Wang, J. Ma, H. M. Cheng and G. Zhou, Fundamentals, status and challenges of direct recycling technologies for lithium ion batteries, *Chem. Soc. Rev.*, 2023, **52**, 51.

3 J. Fan, C. Liu, N. Li, L. Yang, X. G. Yang, B. Dou, S. Hou, X. Feng, H. Jiang and H. Li, Wireless transmission of internal hazard signals in Li-ion batteries, *Nature*, 2025, **641**, 639–645.

4 S. Wang, S. Chen, X. Liu, G. Feng, B. Zhang, W. Xing, Y. Xiao, H. Liu and W. Xiang, Revisiting high-valence dopant mechanisms in Ni-rich cathodes: cation ordering dominates over morphological alignment for enhanced stability, *Chem. Sci.*, 2026, **17**, 3212–3223.

5 D. Lu, R. Li, M. M. Rahman, P. Yu, L. Lv, S. Yang, Y. Huang, C. Sun, S. Zhang and H. Zhang, Ligand-channel-enabled ultrafast Li-ion conduction, *Nature*, 2024, **627**, 101–107.

6 S. Tu, B. Zhang, Y. Zhang, Z. Chen, X. Wang, R. Zhan, Y. Ou, W. Wang, X. Liu, X. Duan, L. Wang and Y. Sun, Fast-charging capability of graphite-based lithium-ion batteries enabled by Li_3P-based crystalline solid–electrolyte interphase, *Nat. Energy*, 2023, **8**, 1365–1374.

7 X. Jia, C. Liu, Z. G. Neale, J. Yang and G. Cao, Active Materials for Aqueous Zinc Ion Batteries: Synthesis, Crystal Structure, Morphology, and Electrochemistry, *Chem. Rev.*, 2020, **120**, 7795–7866.

8 R. Usiskin, Y. Lu, J. Popovic, M. Law and J. Maier, Fundamentals, status and promise of sodium-based batteries, *Nat. Rev. Mater.*, 2021, **6**, 1020–1035.

9 Y. Li, Q. Zhou, S. Weng, F. Ding, X. Qi, J. Lu, Y. Li, X. Zhang, X. Rong and Y. Lu, Interfacial engineering to achieve an energy density of over 200 Wh kg^{-1} in sodium batteries, *Nat. Energy*, 2022, **7**, 9.

10 Y. Wang, X. Chen, J. Liu, D. Qi, H. Hu, H. Jiang, Y. Huang, P. Yan and Y. Xiao, Dual-functional nanoengineering *via* molecular pillaring and conductive hybridization for high-performance aqueous zinc-ion batteries, *Chem. Sci.*, 2026, DOI: 10.1039/D5SC09804A.

11 P. Poizot, J. Gaubicher, S. Renault, L. Dubois, Y. Liang and Y. Yao, Opportunities and Challenges for Organic Electrodes in Electrochemical Energy Storage, *Chem. Rev.*, 2020, **120**, 6490–6557.

12 C. Gervillié-Mouravieff, C. Boussard-Plédel, J. Huang, C. Leau, L. A. Blanquer, M. B. Yahia, M. L. Doublet, S. T. Boles, X. H. Zhang and J. L. Adam, Unlocking cell chemistry evolution with operando fibre optic infrared spectroscopy in commercial Na(Li)-ion batteries, *Nat. Energy*, 2022, **7**, 1157–1169.

13 J. He, A. Bhargav, L. Su, J. Lamb, J. Okasinski, W. Shin, A. Manthiram and F. Khan, Tuning the solvation structure with salts for stable sodium-metal batteries, *Nat. Energy*, 2024, **9**, 446–456.

14 C. Bommier, D. Mitlin and X. Ji, Internal Structure - Na Storage Mechanisms - Electrochemical Performance Relations in Carbons, *Prog. Mater. Sci.*, 2018, **97**, 170–203.

15 C. Wu, W. Huang, Y. Zhang, Q. Chen, L. Li, Y. Zhang, X. Wu and S. L. Chou, Revisiting the critical role of metallic ash elements in the development of hard carbon for advancing sodium-ion battery applications, *eScience*, 2025, **5**, 100371.

16 J. Wang, Y. F. Zhu, Y. Su, J. X. Guo, S. Chen, H. K. Liu, S. X. Dou, S. L. Chou and Y. Xiao, Routes to high-performance layered oxide cathodes for sodium-ion batteries, *Chem. Soc. Rev.*, 2024, **53**, 72.

17 Y. J. Guo, R. X. Jin, M. Fan, W. P. Wang, S. Xin, L. J. Wan and Y. G. Guo, Sodium layered oxide cathodes: properties, practicality and prospects, *Chem. Soc. Rev.*, 2024, **53**, 47.

18 E. Gabriel, C. Ma, K. Graff, A. Conrado, D. Hou and H. Xiong, Heterostructure engineering in electrode materials for sodium-ion batteries:Recent progress and perspectives, *eScience*, 2023, **5**, 100139.

19 C. Xu, J. Chen, G. Feng, Z. Chen, W. Yang, C. Yang, O. Shmatova, Y. S. Hu and J. Zhao, A novel KTP-type $NaTiPO_4F$ electrode material for high-performance Na-ion batteries, *Energy Storage Mater.*, 2025, **76**, 104156.

20 P. Yang, Z. Wu, Y. Liang, H. Chen, C. Lin, J. Qiu, J. Meng, Y. He and S. Zhang, Engineering ion transport in all-solid-state sodium-ion batteries: fundamentals, strategies, and perspectives, *Prog. Mater. Sci.*, 2025, **154**, 101503.

21 B. Nykvist, On par with lithium-ion, *Nat. Energy*, 2025, **10**, 285–286.

22 J. Y. Hwang, S. T. Myung and Y. K. Sun, Sodium-ion batteries: present and future, *Chem. Soc. Rev.*, 2017, **46**, 3529–3614.

23 S. Guo, Y. Sun, P. Liu, J. Yi, P. He, X. Zhang, Y. Zhu, R. Senga, K. Suenaga, M. Chen and H. Zhou, Cation-mixing stabilized layered oxide cathodes for sodium-ion batteries, *Sci. Bull.*, 2018, **63**, 376–384.

24 X. Fangxi, Z. Lei, Y. Chao, J. Mietek and Q. Shi-Zhang, The Application of Hollow Structured Anodes for Sodium-Ion Batteries: From Simple to Complex Systems, *Adv. Mater.*, 2018, **31**, 1800492.

25 C. Vaalma, D. Buchholz, M. Weil and S. Passerini, A cost and resource analysis of sodium-ion batteries, *Nat. Rev. Mater.*, 2018, **3**, 18013.

26 Y. Liu, J. Li, Q. Shen, J. Zhang, P. He, X. Qu and Y. Liu, Advanced characterizations and measurements for sodium-ion batteries with NASICON-type cathode materials, *eScience*, 2022, **2**, 10–31.

27 T. Jin, H. Li, K. Zhu, P.-F. Wang, P. Liu and L. Jiao, Polyanion-type cathode materials for sodium-ion batteries, *Chem. Soc. Rev.*, 2020, **49**, 2342–2377.

28 C. Xu, W. Hua, Q. Zhang, Y. Liu, R. Dang, R. Xiao, J. Wang, Z. Chen, F. Ding and X. Guo, Sufficient Utilization of Mn^{2+}/Mn^{3+}/Mn^{4+} Redox in NASICON Phosphate Cathodes towards High-Energy Na-Ions Batteries, *Adv. Funct. Mater.*, 2023, **33**, 10.

29 S. Jamil, Y. Feng, M. Fasehullah, G. Ali, B. Wu, Y. Guo, B. Jabar, A. Mansoor, Y. Niu and M. Xu, Stabilizing

anionic redox in Mn-rich P2-type layered oxide material by Mg substitution, *Chem. Eng. J.*, 2023, **471**, 144450.
30 J. Choe, J. M. Yuk and F. Khan, Capturing and reducing defects, *Nat. Energy*, 2023, **8**, 1063–1064.
31 Y. Jin, P. M. L. Le, P. Gao, Y. Xu, B. Xiao, M. H. Engelhard, X. Cao, T. D. Vo, J. Hu, L. Zhong, B. E. Matthews, R. Yi, C. Wang, X. Li, J. Liu and J.-G. Zhang, Low-solvation electrolytes for high-voltage sodium-ion batteries, *Nat. Energy*, 2022, **7**, 718–725.
32 Y. Fang, L. Xiao, Z. Chen, X. Ai, Y. Cao and H. Yang, Recent Advances in Sodium-Ion Battery Materials, *Electrochem. Energy Rev.*, 2018, **1**, 294–323.
33 J. Niu, J. Dong, X. Zhang, L. Huang, G. Lu, X. Han, J. Wang, T. Gong, Z. Chen, J. Zhao and G. Cui, Correction: Sodium cluster-driven safety concerns of sodium-ion batteries, *Energy Environ. Sci.*, 2025, **18**, 3418.
34 B. Yang, Y. Wang, R. Zheng, W. Yang, Y. Li, T. Li, K. Li, A. Hu, J. Long and S. Ding, Conformational Engineering of Solvent Molecules for High-Voltage and Fast-Charging Lithium Metal Batteries, *Angew. Chem., Int. Ed.*, 2025, **64**, e202508486.
35 S. Li, Y. Heng, Z. Gu, X. Wang, Y. Liu, X. Zhang, Z. Sun, D. Liu, B. Li and X. Wu, Anion-based electrolyte chemistry for sodium-ion batteries: fundamentals, advances and perspectives, *Chem. Sci.*, 2026, **17**(1), 137–150.
36 Q. Ling, D. Chen, X. Zhu, Y. Zhu, Z. Hong, J. Liu, Q. Sun, Y. Niu, Y. Sun, P. Wang and Y. Xiao, Probing Local Asymmetric Site Anchored Anion Based on Multifunctional Polymer Electrolyte for Sustainable Solid-State Sodium-Metal Battery, *Adv. Mater.*, 2026, **38**(3), e14352.
37 C. Xu, W. Hua, G. Feng, Z. Chen, R. Xiao, Q. Zhang, W. Yang, C. Yang, J. Zhao and Y.-S. Hu, Guiding Design of Mn-Rich Phosphate Cathodes with Less Intrinsic Antisite Defects, *Angew. Chem., Int. Ed.*, 2025, **64**, e202502758.
38 S. Su, Q. Ling, Y. Li, Y. Yan, Y. Zhu and Y. Xiao, Lattice-coherent interface-reinforced sodium-layered oxide cathodes, *Chem. Sci.*, 2025, **16**, 22852–22869.
39 S. He, R. Zhang, X. Han, Y. Zhou, C. Zheng, C. Li, X. Xue, Y. Chen, Z. Wu and J. Gan, Unraveling 3d Transition Metal (Ni, Co, Mn, Fe, Cr, V) Ions Migration in Layered Oxide Cathodes: A Pathway to Superior Li-Ion and Na-Ion Battery Cathodes, *Adv. Mater.*, 2025, **37**, 2413760.
40 Q. Jiangfeng, W. Chen, C. Yuliang and M. Zifeng, Yunhui and Huang, Prussian Blue Cathode Materials for Sodium-Ion Batteries and Other Ion Batteries, *Adv. Energy Mater.*, 2017, **8**, 1702619.
41 C. Xu, R. Xiao, J. Zhao, F. Ding, Y. Yang, X. Rong, X. Guo, C. Yang, H. Liu and B. Zhong, Mn-Rich Phosphate Cathodes for Na-Ion Batteries with Superior Rate Performance, *ACS Energy Lett.*, 2022, **7**, 97–107.
42 X. Jia, Q. Peng, Y. Liu, D. Chen, J. Wang, J. Li, Y. Zhu, N. Xu, L. Kong, H. Liu, G. Zhang, Z. Jian, C. Cheng, H. Dong, L. Zhang, Y. Sun, S. Chen, X. Guo, S. Dou and Y. Xiao, Design principles of practical industrial-scale layered oxide cathodes with air/water stability for sustainable sodium-ion batteries, *Nat. Commun.*, 2025, **16**, 10477.
43 Y. Liu, W. Li and Y. Xia, Recent Progress in Polyanionic Anode Materials for Li (Na)-Ion Batteries, *Electrochem. Energy Rev.*, 2021, **4**, 447–472.
44 Z. Ahsan, Z. Cai, S. Wang, M. Moin, H. Wang, D. Liu, Y. Ma, G. Song and C. Wen, Recent Development of Phosphate Based Polyanion Cathode Materials for Sodium-Ion Batteries, *Adv. Energy Mater.*, 2024, **14**, 2400373.
45 M. Du, K. Li, N. Yu, Z. L. Hao, J. Z. Guo, H. J. Liang, Z. Y. Gu, X. H. Zhang, K. Y. Zhang and Y. Liu, Ultrafast Preparation of High-Entropy NASICON Cathode Enables Stabilized Multielectron Redox and Wide-Temperature (50-60°C) Workability in Sodium-Ion Batteries, *Adv. Mater.*, 2025, **37**, 2418219.
46 C. Liu, K. Chen, H. Xiong, A. Zhao, H. Zhang, Q. Li, X. Ai, H. Yang, Y. Fang and Y. Cao, A novel $Na_8Fe_5(SO_4)_9$@rGO cathode material with high rate capability and ultra-long lifespan for low-cost sodium-ion batteries, *eScience*, 2024, **4**, 100186.
47 G. Su, Y. Wang, J. Mu, Y. Ren, P. Yue, W. Ji, L. Liang, L. Hou, M. Chen and C. Yuan, Insights into Tiny High-Entropy Doping Promising Efficient Sodium Storage of $Na_3V_2(PO_4)_2O_2F$ toward Sodium-Ion Batteries, *Adv. Energy Mater.*, 2025, **15**, 2403282.
48 P. Moreau, D. Guyomard, J. Gaubicher and F. Boucher, ChemInform Abstract: Structure and Stability of Sodium Intercalated Phases in Olivine $FePO_4$, *Chem. Mater.*, 2010, **22**, 4126–4128.
49 L. Zhu, S. Xiang, M. Wang, D. Sun, X. Zhang, L. Fu, X. Huang, Y. Tang, Q. Zhang and H. Wang, Lattice Regulation Boosts Working Voltage and Energy Density of $Na_{3.12}Fe_{2.44}(P_2O_7)_2$ Cathode for Sodium-Ion Batteries, *Adv. Funct. Mater.*, 2025, **35**, 2419611.
50 Z. Jing, M. Mamoor, L. Kong, L. Wang, B. Wang, M. Chen, F. Wang, G. Qu, Y. Kong, D. Wang, X. He, C. Wang, X. Zhang, Y. Zhang, G. Wang and L. Xu, Rational Design of Cobalt-Based Prussian Blue Analogues *via* 3 d Transition Metals Incorporation for Superior Na-Ion Storage, *Angew. Chem., Int. Ed.*, 2025, **64**, e202423356.
51 H. Fu, X. Wang, J. Yang, Z. Wu, H. Ren, J. Ji, M. Shi and E. H. Ang, In situ surface manipulation Mn-based Prussian blue analogues with enhanced redox chemistry and ion diffusion toward high-energy-density aqueous sodium-ion batteries, *Chem. Sci.*, 2026, **17**(2), 968–976.
52 C. Xu, L. Zhou, T. Gao, Z. Chen, X. Hou, J. Zhang, Y. Bai, L. Yang, H. Liu and C. Yang, Development of High-Performance Iron-Based Phosphate Cathodes toward Practical Na-Ion Batteries, *J. Am. Chem. Soc.*, 2024, **146**, 9.
53 C. Xu, J. Zhao, E. Wang, X. Liu, X. Shen, X. Rong, Q. Zheng, G. Ren, N. Zhang and X. Liu, A Novel NASICON-Typed $Na_4VMn_{0.5}Fe_{0.5}(PO_4)_3$ Cathode for High-Performance Na-Ion Batteries, *Adv. Energy Mater.*, 2021, **11**, 2100729.
54 J. M. L. Meins, M. P. Crosnier-Lopez, A. Hemon-Ribaud and G. Courbion, Phase Transitions in the $Na_3M_2(PO_4)_2F_3$ Family (M=Al^{3+}, V^{3+}, Cr^{3+}, Fe^{3+}, Ga^{3+}): Synthesis, Thermal,

Structural, and Magnetic Studies, *J. Solid State Chem.*, 1999, **148**, 260–277.

55 R. A. Shakoor, D. H. Seo, H. Kim, Y. U. Park and K. Kang, A combined first principles and experimental study on $Na_3V_2(PO_4)_2F_3$ for rechargeable Na batteries, *Mater. Chem.*, 2012, **22**, 20535–20541.

56 H. Arraghraghi, M. Häfner and M. Bianchini, Computational design of phosphate fluoride cathode materials for Na-based batteries, *J. Mater. Chem. A*, 2025, **13**, 35521–35532.

57 W. Song, X. Cao, Z. Wu, J. Chen and X. Ji, Investigation of the Sodium Ion Pathway and Cathode Behavior in $Na_3V_2(PO_4)_2F_3$ Combined *via* a First Principles Calculation, *Langmuir*, 2014, **30**, 12438–12446.

58 K. Lin, Q. Liu, Y. Zhou, H. Chen, J. Liu, J. Z. Zhao and X. Hou, Fluorine substitution and pre-sodiation strategies to boost energy density of V-based NASICON-structured SIBs: Combined theoretical and experimental study, *Chem. Eng. J.*, 2023, **463**, 12.

59 Z. Liu, Y. Y. Hu, M. T. Dunstan, H. Huo, X. Hao, H. Zou, G. Zhong, Y. Yang and C. P. Grey, Local Structure and Dynamics in the Na Ion Battery Positive Electrode Material $Na_3V_2(PO_4)_2F_3$, *Cheminform*, 2014, **45**, 2513–2521.

60 Y. Gao, H. Zhang, X. H. Liu, Z. Yang, X. X. He, L. Li, Y. Qiao and S. L. Chou, Low-Cost Polyanion-Type Sulfate Cathode for Sodium-Ion Battery, *Adv. Energy Mater.*, 2021, **11**, 2101751.

61 C. Xu, J. Zhao, Y. A. Wang, W. Hua, Q. Fu, X. Liang, X. Rong, Q. Zhang, X. Guo and C. Yang, Reversible Activation of V^{4+}/V^{5+} Redox Couples in NASICON Phosphate Cathodes, *Adv. Energy Mater.*, 2022, **12**, 2200966.

62 J. Guo, P. Wang, X. Wu, X. Zhang, Q. Yan, H. Chen, J. Zhang and Y. Guo, High-Energy/Power and Low-Temperature Cathode for Sodium-Ion Batteries: *In Situ* XRD Study and Superior Full-Cell Performance, *Adv. Mater.*, 2017, **29**, 1701968.

63 G. Yan, S. Mariyappan, G. Rousse, Q. Jacquet, M. Deschamps, R. David, B. Mirvaux, J. W. Freeland and J. M. Tarascon, Higher energy and safer sodium ion batteries *via* an electrochemically made disordered $Na_3V_2(PO_4)_2F_3$ material, *Nat. Commun.*, 2019, **10**, 585.

64 X. Chen, Q. Wu, P. Guo and X. Liu, Rational design of two dimensional single crystalline $Na_3V_2(PO_4)_2F_3$ nanosheets for boosting Na^+ migration and mitigating grain pulverization, *Chem. Eng. J.*, 2022, **439**, 135533.

65 P. Serras, V. Palomares, A. Goñi, G. D. M. Izaskun, P. Kubiak, L. Lezama and T. Rojo, High voltage cathode materials for Na-ion batteries of general formula $Na_3V_2O_{2x}(PO_4)_2F_{3-2x}$, *J. Mater. Chem.*, 2012, **22**, 22301–22308.

66 R. A. Shakoor, D.-H. Seo, H. Kim, Y.-U. Park, J. Kim, S.-W. Kim, H. Gwon, S. Lee and K. Kang, A combined first principles and experimental study on $Na_3V_2(PO_4)_2F_3$ for rechargeable Na batteries, *J. Mater. Chem.*, 2012, **22**, 20535–20541.

67 F. He, J. Kang, R. Wang, Z. Li, H. Li, B. Zhong, F. Wan, Z. Wu and X. Guo, Rapid and efficient microwave-assisted solid-phase synthesis of $Na_3V_2(PO_4)_2F_3$ and exploration of the synthesis process, *Chem. Commun.*, 2025, **61**, 6623–6626.

68 L. Li, Y. Xu, X. Sun, R. Chang, Y. Zhang, X. Zhang and J. Li, Fluorophosphates from solid-state synthesis and electrochemical Ion exchange: $NaVPO_4F$ or $Na_3V_2(PO_4)_2F_3$?, *Adv. Energy Mater.*, 2018, **8**, 1801064.

69 M. Wang, X. Huang, H. Wang, T. Zhou, H. Xie and Y. Ren, Synthesis and electrochemical performances of $Na_3V_2(PO_4)_2F_3$/C composites as cathode materials for sodium ion batteries, *RSC Adv.*, 2019, **9**, 30628–30636.

70 Q. Hu, M. Sun, Y. Zha, G. Zhao, H. Tang, L. Yang, M. Yang, B. Pang, Y. Sun and H. Guo, Ti Substitution Strategy Improves Electrochemical Performance of $Na_3V_2(PO_4)_2F_3$ Cathode, *ACS Energy Lett.*, 2025, **10**, 1840–1850.

71 L. Li, J. Zhao, H. Zhao, Y. Qin, X. Zhu, H. Wu, Z. Song and S. Ding, Structure, composition and electrochemical performance analysis of fluorophosphates from different synthetic methods: is really $Na_3V_2(PO_4)_2F_3$ synthesized?, *J. Mater. Chem. A*, 2022, **10**, 8877–8886.

72 W. Liu, H. Yi, Q. Zheng, X. Li and H. Zhang, Y-Doped $Na_3V_2(PO_4)_2F_3$ compounds for sodium ion battery cathodes: electrochemical performance and analysis of kinetic properties, *J. Mater. Chem. A*, 2017, **5**, 10928–10935.

73 C. Guo, J. Yang, Z. Cui, S. Qi and S. Chen, In-situ structural evolution analysis of Zr-doped $Na_3V_2(PO_4)_2F_3$ coated by N-doped carbon layer as high-performance cathode for sodium-ion batteries, *J. Energy Chem.*, 2021, **65**, 514–523.

74 M. Peng, X. Wang and G. Guo, Synthesis of nano-$Na_3V_2(PO_4)_2F_3$ cathodes with excess Na^+ intercalation for enhanced capacity, *Appl. Mater. Today*, 2020, **19**, 100554.

75 K. Liang, H. Zhao, J. Li, X. Huang, S. Jia, W. Chen and Y. Ren, Engineering Crystal Growth and Surface Modification of $Na_3V_2(PO_4)_2F_3$ Cathode for High-Energy-Density Sodium-Ion Batteries, *Small*, 2023, **19**, 2207562.

76 C. Yangsheng, C. Xinxin, L. Zhigao, F. Guozhao and L. Fei, Caging $Na_3V_2(PO_4)_2F_3$ microcubes in cross-linked graphene enabling ultrafast sodium storage and long-term cycling, *Adv. Sci.*, 2018, **5**, 1800680.

77 J. Yang, N. Liu, G. Jiang, W. Sheng, X. Zheng, Z. Bai and X. Jiang, Synthesis and investigation of sodium storage properties in $Na_3V_{1.9}Fe_{0.1}(PO_4)_2F_3$@N-CNTs cathode material for sodium ion batteries, *Chem. Eng. J.*, 2024, **485**, 149834.

78 X. Zhai, X. Chen, Q. Zhang, Y. Wu, X. Wang, H. Dai, J. Chen, C. Shang and D. Liu, Temperature-dependent defect evolution and electrochemical performance enhancement of $Na_3V_2(PO_4)_2F_3$, *J. Alloys Compd.*, 2023, **952**, 170001.

79 C. Shen, H. Long, G. Wang, W. Lu, L. Shao and K. Xie, $Na_3V_2(PO_4)_2F_3$@C dispersed within carbon nanotube frameworks as a high tap density cathode for high-performance sodium-ion batteries, *J. Mater. Chem. A*, 2018, **6**, 6007–6014.

80 Q. Zhou, Y. Wang, R. Ou, X. Ding, Y. Xin, F. Wu and H. Gao, Yolk-Shell Construction of $Na_3V_2(PO_4)_2F_3$ with Copper Substitution Microsphere as High-Rate and Long-Cycling Cathode Materials for Sodium-Ion Batteries, *Small*, 2024, **20**, 2310699.

81 Z. Hu, R. Zhang, C. Fan, X. Liu, P. Gao, W. Zhang, Z. Liu, S. Han, J. Liu and J. Liu, Synergistic Effect, Structural and Morphology Evolution, and Doping Mechanism of Spherical Br-Doped Na, *Small*, 2022, **18**, e2201719.
82 C. Xu, J. Zhao, C. Yang and Y. S. Hu, Polyanionic Cathode Materials for Practical Na-Ion Batteries toward High Energy Density and Long Cycle Life, *ACS Cent. Sci.*, 2023, **9**, 1721–1736.
83 Z. Liu, Y.-Y. Hu, M. T. Dunstan, H. Huo, X. Hao, H. Zou, G. Zhong, Y. Yang and C. P. Grey, Local Structure and Dynamics in the Na Ion Battery Positive Electrode Material $Na_3V_2(PO_4)_2F_3$, *Chem. Mater.*, 2014, **26**, 2513–2521.
84 L. Li, N. Zhang, Y. Su, J. Zhao, Z. Song, D. Qian, H. Wu, M. Tahir, A. Saeed and S. Ding, Fluorine Dissolution-Induced Capacity Degradation for Fluorophosphate-Based Cathode Materials, *ACS Appl. Mater. Interfaces*, 2021, **13**(20), 23787–23793.
85 L. Deng, F. D. Yu, Y. Xia, Y. S. Jiang and Z. B. Wang, Stabilizing Fluorine to Achieve High-Voltage and Ultra-Stable $Na_3V_2(PO_4)_2F_3$ Cathode for Sodium Ion Batteries, *Nano Energy*, 2020, **82**, 105659.
86 J. Gao, Y. Tian, L. Ni, B. Wang, K. Zou, Y. Yang, Y. Wang, C. E. Banks, D. Zhang and K. Zhou, Robust Cross-Linked $Na_3V_2(PO_4)_2F_3$ Full Sodium-Ion Batteries, *Energy Environ. Mater.*, 2024, **7**, e12485.
87 C. Sun, L. L. Zhang, X. Q. Xiong, Z. R. Deng, H. B. Sun and X. L. Yang, Electronic/Ionic Dual Functional Layer-Coated $Na_3V_2(PO_4)_2F_3$ Cathode with High Sodium Storage Performance, *ACS Sustain. Chem. Eng.*, 2024, **12**, 10892–10904.
88 Y. Zhang, W. Song, Y. Tang, D. Jia and Y. Huang, Amylopectin-Assisted Fabrication of *In Situ* Carbon-Coated Na, *ACS Appl. Mater. Interfaces*, 2022, **14**, 40812–40821.
89 L. Wang, J. Wang, H. Chen, H. Dong, H. Wang, Y. Wang, Y. Xiao, J. Wang and S. Chen, Fast Screening Suitable Doping Transition Metals to $Na_3V_2(PO_4)_2F_3$ for Sodium-Ion Batteries with High Energy Density in Wide-Temperature Range, *Adv. Mater.*, 2025, **37**, 2505093.
90 Y. Zhao, B. Wang, Q. Huang, C. Liu, Y. Pan, L. Guo and Y. Chen, Trace polytetrafluoroethylene constructing $Na_3V_2(PO_4)_3/Na_3V_2(PO_4)_2F_3$ heterostructure with multi-electron reaction and self-enhanced built-in electric field, *Energy Storage Mater.*, 2025, **81**, 104462.
91 K. Missaoui, K. Ferchichi, N. Amdouni, J. L. Gómez-Cámer, C. Pérez-Vicente, A. Bonilla, D. Cosano, L. Caballero and G. F. Ortiz, Polyaniline-Coated $Na_3V_2(PO_4)_2F_3$ Cathode Enables Fast Sodium Ion Diffusion and Structural Stability in Rechargeable Batteries, *ACS Appl. Mater. Interfaces*, 2024, **16**, 50550–50560.
92 Z. Gu, J. Guo, Z. Sun, X. Zhao, W. Li, X. Yang, H. Liang, C. Zhao and X. Wu, Carbon-coating-increased working voltage and energy density towards an advanced $Na_3V_2(PO_4)_2F_3$@C cathode in sodium-ion batteries, *Sci. Bull.*, 2020, **65**, 702–710.
93 P. Zhu, W. Peng, H. Guo, X. Li, Z. Wang, D. Wang, J. Duan, J. Wang and G. Yan, Toward High-Performance Sodium Storage Cathode: Construction and Purification of Carbon-Coated $Na_3V_2(PO_4)_2F_3$ Materials, *J. Power Sources*, 2022, **546**, 231986.
94 J. Zhang, C. Zhang, Y. Han, X. Zhao, W. Liu and Y. Ding, A surface-modified $Na_3V_2(PO_4)_2F_3$ cathode with high rate capability and cycling stability for sodium ion batteries, *RSC Adv.*, 2024, **14**, 13703–13710.
95 F. Li, Y. Zhao, L. Xia, Z. Yang, J. Wei and Z. Zhou, Well-dispersed $Na_3V_2(PO_4)_2F_3$@rGO with improved kinetics for high-power sodium-ion batteries, *J. Mater. Chem. A*, 2020, **8**, 12391–12397.
96 G. Minart, L. Croguennec, F. Weill, C. Labrugère-Sarroste and J. Olchowka, Increasing Tap Density of Carbon-Coated $Na_3V_2(PO_4)_2F_3$ *via* Mechanical Grinding: Good or Bad Idea?, *ACS Appl. Energy Mater.*, 2024, **7**, 11334–11342.
97 Z. Song, Y. Liu, Z. Guo, Z. Liu, Z. Li, J. Zhou, W. Liu, R. Liu, J. Zhang and J. Luo, Ultrafast Synthesis of Large-Sized and Conductive $Na_3V_2(PO_4)_2F_3$ Simultaneously Approaches High Tap Density, Rate and Cycling Capability, *Adv. Funct. Mater.*, 2024, **34**, 2313998.
98 Y. Li, X. Liang, G. Chen, W. Zhong and J. Hu, In-situ constructing $Na_3V_2(PO_4)_2F_3$/carbon nanocubes for fast ion diffusion with high-performance Na^+-storage, *Chem. Eng. J.*, 2019, **387**, 123952.
99 K. Liang, H. Zhao, J. Li, X. Huang and Y. Ren, High-performance $Na_3V_2(PO_4)_2F_3$ cathode obtained by a three-in-one strategy for self-sodium compensation, interface modification, and crosslinked carbon coatings, *Appl. Surf. Sci.*, 2023, **615**, 156412.
100 M. Wang, Y. Wang, Y. Xin, Q. Liu, F. Wu and H. Gao, Nitrogen-Doped Carbon Coated $Na_3V_2(PO_4)_2F_3$ Derived from Polyvinylpyrrolidone as a High-Performance Cathode for Sodium-Ion Batteries, *ACS Appl. Energy Mater.*, 2023, **6**, 4453–4461.
101 X. Yu, T. Lu, X. Li, J. Qi, L. Yuan, Z. Man and H. Zhuo, Ionic Liquid-Acrylic Acid Copolymer Derived Nitrogen-Boron Codoped Carbon-Covered Na, *Langmuir*, 2022, **38**, 7815–7824.
102 C. Sun, L. L. Zhang, Z. R. Deng, B. Yan, L. Gao and X. L. Yang, PTFE-derived carbon-coated $Na_3V_2(PO_4)_2F_3$ cathode material for high-performance sodium ion battery, *Electrochim. Acta*, 2022, **432**, 141187.
103 X. Zhang, H. Tian, Y. Cai, L. Wang, X. Yao and Z. Su, Effects of nitrogen and sulfur atom regulation on electrochemical properties of $Na_3V_2(PO_4)_2F_3$ cathode material for Na-ion batteries, *Ceram. Int.*, 2022, **48**, 36129–36135.
104 C. Sun, L.-L. Zhang, Z.-R. Deng, H.-B. Sun and X.-L. Yang, Achieving High-Performance $Na_3V_2(PO_4)_2F_3$ Cathode Material through a Bifunctional N-Doped Carbon Network, *ACS Appl. Mater. Interfaces*, 2024, **16**, 35179–35189.
105 Y. Hu, P. Chen, F. Liu, X. Cheng, Y. Shao, P. Lu, H. Zhang, S. Li, F. Huang and Y. Jiang, Dual-anion ether electrolyte enables stable high-voltage $Na_3V_2(PO_4)_2F_3$ cathode under wide temperatures, *J. Power Sources*, 2024, **602**, 234405.
106 P. L. M. Kanta, M. Venkatesh, S. Nandy, K. H. Chae, N. L. Priya, S. K. Yadav, R. Gopalan and B. Das,

Outstanding specific energy achieved *via* reversible cycling of V^{4+}/V^{2+} redox couple in N-doped carbon coated $Na_3V_2(PO_4)_2F_3$: An ex-situ XRD, XPS and XAS study, *Energy Storage Mater.*, 2025, **48**, 101802.

107 W. Zhu, K. Liang and Y. Ren, Modification of the Morphology of $Na_3V_2(PO_4)_2F_3$ as Cathode Material for Sodium-ion Batteries by Polyvinylpyrrolidone, *Ceram. Int.*, 2021, **47**, 17192–17201.

108 M. Qin, N. Qin, M. Lei, D. Ji, W. Liu, X. Cao, G. Fang and S. Liang, Construction of $Na_3V_2(PO_4)_2F_3$@C/CNTs nanocomposites with three-dimensional conductive network as cathode materials for sodium-ion batteries, *J. Electroanal. Chem.*, 2022, **920**, 116613.

109 J. Ou, H. Wang, H. Deng, B. Li and H. Zhang, Hydrothermally prepared composite of $Na_3V_2(PO_4)_2F_3$ with gelatin and graphene used as a high-performance sodium ion battery cathode, *J. Alloys Compd.*, 2022, **926**, 166857.

110 Y. Mao, X. Zhang, Y. Zhou and W. Chu, Microwave-assisted Synthesis of Porous Nano-sized $Na_3V_2(PO_4)_2F_3$@C Nanospheres for Sodium Ion Batteries with Enhanced Stability, *Scripta Mater.*, 2020, **181**, 92–96.

111 S. Xu, Y. Zhu, X. Li, Y. Wang, D. Yan, X. Niu, J. Jiang, R. Wu and J. S. Chen, PVA-regulated construction of 3D rGO-hosted $Na_3V_2(PO_4)_2F_3$ for fast and stable sodium storage, *J. Energy Chem.*, 2024, **99**, 100–109.

112 C. Shi, J. Xu, T. Tao, X. Lu, G. Liu, F. Xie, S. Wu, Y. Wu and Z. Sun, Zero-Strain $Na_3V_2(PO_4)_2F_3$@Rgo/CNT Composite as a Wide-Temperature-Tolerance Cathode for Na-Ion Batteries with Ultrahigh-Rate Performance, *Small Methods*, 2024, **8**, 2301277.

113 M. Liang, W. Li, Y. Yang, H. Li, J. Liang, C. Lin, X. Meng, J. Liu, Z. Shi and L. Liu, Carbon Nanofiber/$Na_3V_2(PO_4)_2F_3$ Particle Composites as a Self-Standing Cathode for High-Voltage Flexible Sodium-Ion Batteries, *ACS Appl. Nano Mater.*, 2023, **6**, 22275–22282.

114 W. Zhan, C. Fan, W. Zhang, G. Yi, H. Chen, S. Han and J. Liu, Ultra-long cycle life and high rate performance subglobose $Na_3V_2(PO_4)_2F_3$@C cathode and its regulation, *Int. J. Energy Res.*, 2020, **44**, 6608–6622.

115 R. Guo, W. Li, M. Lu, Y. Lv, H. Ai, D. Sun, Z. Liu and G. C. Han, $Na_3V_2(PO_4)_2F_3$@bagasse carbon as cathode material for lithium/sodium hybrid ion battery, *Phys. Chem. Chem. Phys.*, 2022, **24**, 5638–5645.

116 L. Lei, K. Sun, Z. Hongwei, C. Wang and T. Wei, Large scale preparation of $Na_3V_2(PO_4)_2F_3$ with cross-linked double carbon network for high energy density sodium ion batteries at -20°C, *J. Energy Storage*, 2024, **78**, 109923.

117 J. Ma, W. Li, X. Lan, Z. Liu, F. Zhou, M. Lu and G. C. Han, Co/N-doped carbon-coated $Na_3V_2(PO_4)_2F_3$ cathode for SIB *via* a bimetallic MOF template, *Inorg. Chem. Commun.*, 2025, **179**, 114849.

118 R. Ling, S. Zhao, C. Yang and W. Qi, Three-dimensional ordered microporous $Na_3V_2(PO_4)_2F_3$@C/Carbon cloth as High-rate and stable flexible cathodes for Na-ion and Zn-ion batteries, *Appl. Surf. Sci.*, 2023, **620**, 156875.

119 S. Z. Lv, L. R. Liu, Y. Q. Zheng, J. Liu, Y. W. Wang, J. J. Hou, Z. H. He, A. M. Lv, L. Deng and L. Zhao, Fluorine-compensated $Na_3V_2(PO_4)_2F_3$ cathode for long-term durable sodium ion batteries, *J. Power Sources*, 2025, **656**, 238074.

120 Y. Pi, J. Xiao, L. Cheng, H. Cheng, X. Deng, Y. Ke, X. Yang and Q. An, Stress-Induced Dual-Carbon Coating of $Na_3V_2(PO_4)_2F_3$ Cathode for Sodium-Ion Batteries, *Batter. Supercaps*, 2026, **9**(1), e202500325.

121 K. Missaoui, K. Ferchichi, N. Amdouni, J. L. Gómez-Cámer, C. Pérez-Vicente, A. Bonilla, D. Cosano, Á. Caballero and G. F. Ortiz, Polyaniline-Coated $Na_3V_2(PO_4)_2F_3$ Cathode Enables Fast Sodium Ion Diffusion and Structural Stability in Rechargeable Batteries, *ACS Appl. Mater. Interfaces*, 2024, **16**, 50550–50560.

122 Z. Bai, A. Wang, Y. Wang, N. Wang and Y. Chai, Regulation of the electrochemical performance of $Na_3V_2(PO_4)_2F_3$ as an Na storage material through electron redistribution by Bi-doping, *J. Power Sources*, 2025, **642**, 236941.

123 S. M. Wang, J. Q. Li, L. Xu, M. J. Sun, W. J. Huang, Q. Liu, F. T. Ren, Y. J. Sun, L. Y. Duan and H. Ma, Manipulation of $Na_3V_2(PO_4)_2F_3$ *via* aluminum doping to alter local electron states toward an advanced cathode for sodium-ion batteries, *Rare Met.*, 2024, **43**, 4253–4262.

124 Z. Y. Gu, Y. L. Heng, J. Z. Guo, J. M. Cao, X. T. Wang, X. X. Zhao, Z. H. Sun, S. H. Zheng, H. J. Liang and B. Li, Nano self-assembly of fluorophosphate cathode induced by surface energy evolution towards high-rate and stable sodium-ion batteries, *Nano Res.*, 2023, **16**, 439–448.

125 J. Zhang, Y. Lai, P. Li, Y. Wang, F. Zhong, X. Feng, W. Chen, J. Liu, X. Ai, H. Yang and Y. Cao, Boosting Rate and Cycling Performance of K-doped $Na_3V_2(PO_4)_2F_3$ Cathode for High-Energy-Density Sodium-Ion Batteries, *Green Energy Environ.*, 2022, **7**, 1253–1262.

126 M. Wang, K. Wang, X. Huang, T. Zhou, H. Xie and Y. Ren, Improved sodium storage properties of Zr-doped $Na_3V_2(PO_4)_2F_3$/C as cathode material for sodium ion batteries, *Ceram. Int.*, 2020, **46**, 28490–28498.

127 Z. Gu, J. Guo, J. Cao, X. Wang, X. Zhao, X. Zheng, W. Li, Z. Sun, H. Liang and X. Wu, An Advanced High-Entropy Fluorophosphate Cathode for Sodium-Ion Batteries with Increased Working Voltage and Energy Density, *Adv. Mater.*, 2022, **34**, 2110108.

128 R. A. P. Camacho, Y. Zhao, X. Wang, Q. Wang, L. Shen, J. Gu, M. Gao and L. Lu, Lattice engineering of Zn-doped $Na_3V_2(PO_4)_2F_3$ for high-rate, wide-temperature sodium-ion batteries, *J. Power Sources*, 2025, **660**, 238519.

129 L. Li, Y. Xu, R. Chang, C. Wang and X. Ding, Unraveling the Mechanism of Optimal Concentration for Fe Substitution in $Na_3V_2(PO_4)_2F_3$/C for Sodium-Ion Batteries, *Energy Storage Mater.*, 2021, **37**, 325–335.

130 M. Sun, Y. Sun, H. Ma, S. Wang, Q. Liu, G. Zhao, L. Duan, Q. Hu, Q. An, K. Zeng, W. Huang, X. Zou, Y. Yang and H. Guo, High-Entropy Doping Enabling Ultrahigh Power Density for Advanced Sodium-Ion Batteries, *ACS Nano*, 2025, **19**, 18386–18396.

131 Q. Wu, Y. Ma, S. Zhang, X. Chen, J. Bai, H. Wang and X. Liu, Achieving a Rapid Na^+ Migration and Highly Reversible Phase Transition of NASICON for Sodium-Ion Batteries with Suppressed Voltage Hysteresis and Ultralong Lifespan, *Small*, 2024, **20**, 2404660.

132 J. Lin, X. Shi, J. Xu, L. Shao and Z. Sun, Enabling Accelerated Na^+ Dynamics Through Li-Induced Electrostatic Shielding for High-Performance $Na_3V_2(PO_4)_2F_3$ Cathode, *Adv. Energy Mater.*, 2025, **15**, 2501979.

133 H. Yu, J. Wang, H. Jing, C. Wu, E. Hu, S. Xi, X. Wang, Z. Fang, X. Wu, Q. Liang, W. Qi, Q. Yan, H. Wang and C. Du, Broadening the Na^+ diffusion degree of freedom to unlock a rapid sodium storage potential in fluorophosphate cathode, *Sci. Bull.*, 2025, **70**, 3361–3370.

134 K. Gao, Q. Hu, G. Han, Y. Xia, J. Liao and J. Yao, Polyaniline lamellated $Na_3V_2(PO_4)_2O_2F$ with fast kinetics toward high-performance sodium-ion batteries, *Chem. Eng. J.*, 2025, **511**, 162163.

135 C. Xu, Q. Fu, W. Hua, Z. Chen, Q. Zhang, Y. Bai, C. Yang, J. Zhao and Y. Hu, Overcoming Kinetic Limitations of Polyanionic Cathode toward High-Performance Na-Ion Batteries, *ACS Nano*, 2024, **18**, 18758–18768.

136 H. Yu, H. Jing, Y. Gao, X. Wang, Z. Gu, L. Li, J. Wang, S. Wang, X. Wu, W. Qi, Q. Liang and C. Du, Unlocking the Sodium Storage Potential in Fluorophosphate Cathodes: Electrostatic Interaction Lowering *Versus* Structural Disordering, *Adv. Mater.*, 2025, **37**, 2400229.

137 X. Wang, Q. Wang, J. Zhang, Y. Ma, M. Huang and X. Liu, Vanadium-site multivalent cation doping strategy of fluorophosphate cathode for low self-discharge sodium-ion batteries, *J. Energy Chem.*, 2025, **102**, 365–376.

138 H. Zhou, Z. Cao, Y. Zhou, J. Li, Z. Ling, G. Fang, S. Liang and X. Cao, Unlocking rapid and robust sodium storage of fluorophosphate cathode *via* multivalent anion substitution, *Nano Energy*, 2023, **114**, 108604.

139 Q. Zhang, X. G. Sun and K. Liu, Synergistic Coupling Effect of Electronic Conductivity and Interphase Compatibility on High-Voltage $Na_3V_2(PO_4)_2F_3$ Cathodes, *ACS Sustain. Chem. Eng.*, 2023, **11**, 12992–13001.

140 B. Moossa, J. J. Abraham, A. M. Ahmed, R. Kahraman, S. Al-Qaradawi and R. A. Shakoor, Synergistic effect of NASICON $Na_3V_2(PO_4)_2F_3$ and 2D MXene for high-performance symmetric Sodium-ion batteries, *Mater. Res. Bull.*, 2025, **182**, 113173.

141 L. Li, Y. Qin, S. Zhang, H. Zhao, J. Zhao, X. Li, J. Zhao, H. Wu, Y. Su and S. Ding, Ion transport through carbon nanotubes enable highly crystalline $Na_3V_2(PO_4)_2F_3$ cathode for ultra-stable sodium-ion storage, *J. Power Sources*, 2023, **576**, 233226.

142 Y. Xie, Y. Yang, S. Chen, Y. Huang, Z. Chen, X. Wu, L. Zhu, R. Zeng and Z. Yuan, $Na_3V_2(PO_4)_2F_3/LiNi_{0.8}Co_{0.1}Mn_{0.1}O_2$ composite as cathode for practical Li–Na hybrid ion batteries, *J. Power Sources*, 2025, **639**, 236659.

143 C. Wang, L. Zhang, X. Fu, C. Sun, H. Sun and X. Yang, Synergistic modification of hollow-layered iron-based Prussian blue cathode material by embedding $Na_3V_2(PO_4)_2F_3$ particles and coating aminated perylene tetracarboxylic dianhydride layers, *Appl. Surf. Sci.*, 2025, **689**, 162476.

144 W. Ma, Y. Zhou, X. Zhao, X. Cao, P. Wu, X. Zhu, S. Wei, K. Sun, H. Zhou and Y. Zhou, Ultra-Fast-Charging, Long-Duration, and Wide-Temperature-Range Sodium Storage Enabled by Multiwalled Carbon Nanotube-Hybridized Biphasic Polyanion-Type Phosphate Cathode Materials, *ACS Appl. Mater. Interfaces*, 2024, **16**, 34819–34829.

145 Z. Li, L. Qiu, P. Li, H. Liu, D. Wang, W. Hua, T. Chen, Y. Song, F. Wan and B. Zhong, Exposing the (002) active facet by reducing surface energy for a high-performance $Na_3V_2(PO_4)_2F_3$ cathode, *J. Mater. Chem. A*, 2024, **12**, 7777–7787.

146 S. Mahato and K. Biswas, Boosting sodium-ion battery performance with vanadium substituted Fe, Ni dual doped fluorophosphate cathode over a wide temperature range, *J. Power Sources*, 2025, **626**, 235734.

147 D. A. Puspitasari, J. Patra, R. F. H. Hernandha, Y. S. Chiang, A. Inoishi, B. K. Chang, T. C. Lee and J. K. Chang, Enhanced Electrochemical Performance of Ca-Doped $Na_3V_2(PO_4)_2F_3$/C Cathode Materials for Sodium-Ion Batteries, *ACS Appl. Mater. Interfaces*, 2024, **16**, 496–506.

148 C. Cai, Q. Liu, Z. Hu, S. Chen, W. Zhang, Z. Wang, J. Liu and C. Fan, Construction of superior performance $Na_3V_{2-x}Cr_x(PO_4)_2F_3$/C cathode by homovalent doping strategy toward enhanced sodium ion storage, *J. Power Sources*, 2023, **571**, 233080.

149 Y. Zhang, J. Xun, K. Zhang, B. Zhang and H. Xu, 2D-lamellar stacked $Na_3V_2(PO_4)_2F_3@RuO_2$ as a high-voltage, high-rate capability and long-term cycling cathode material for sodium ion batteries, *J. Mater. Chem. A*, 2022, **10**, 11163–11171.

150 X. Yi, H. Luo, Y. Zhou, S. Feng, J. Wang, Z. Wang, J. Duan, D. Wang, H. Guo and G. Yan, Effect of Cr^{3+} doping on the electrochemical performance of $Na_3V_2(PO_4)_2F_3$/C cathode materials for sodium ion battery, *Electrochim. Acta*, 2023, **437**, 141491.

151 Y. Zhang, S. Guo and H. Xu, Synthesis of uniform hierarchical $Na_3V_{1.95}Mn_{0.05}(PO_4)_2F_3@C$ hollow microspheres as a cathode material for sodium-ion batteries, *J. Mater. Chem. A*, 2018, **6**, 4525–4534.

152 C. Pablos, J. Olchowka, E. Petit, G. Minart, M. Duttine, F. Weill, C. Masquelier, D. Carlier and L. Croguennec, Thermal Stability of $Na_{3-x}V_2(PO_4)_2F_{3-y}O_y$: Influence of F^- for O^{2-} Substitution and Degradation Mechanisms, *Chem. Mater.*, 2023, **35**, 4078–4088.

153 S. Guo, J. Peng, N. Sharma, J. Pan, Y. Liao, X. An, H. Li, Z. Ge, C. Zhou and W. L. Tan, Optimizing Sc-Doped $Na_3V_2(PO_4)_2F_3$/C as a High-Performance Cathode Material for Sodium-Ion Battery Applications, *Chem. Mater.*, 2025, **37**, 1500–1512.

154 Y. Zhang, Y. Hu, T. Feng, Z. Xu and M. Wu, Mg-doped $Na_3V_{2-x}Mg_x(PO_4)_2F_3@C$ sodium ion cathodes with enhanced stability and rate capability, *J. Power Sources*, 2024, **602**, 234337.

155 J. Wang, Q. Liu, S. Cao, H. Zhu and Y. Wang, Boosting sodium-ion battery performance with binary metal-doped $Na_3V_2(PO_4)_2F_3$ cathodes, *J. Colloid Interface Sci.*, 2024, **665**, 1043–1053.

156 C. Sankalpita, W. Ziliang, K. Arun, P. Arad, T. Sarah, Y. Reut, P. Ilana, M. Ayan and N. Malachi, Boosting sodium-ion mobility in $Na_3V_2(PO_4)_2F_3$ through anion engineering with Br substitution, *J. Mater. Chem. A*, 2025, **13**, 33294–33304.

157 J. Yang, N. Liu, G. Jiang, H. Peng, K. Mi, N. Wang, Z. Bai and X. Jiang, Medium-Entropy Engineering Enhances Na^+/Electron Transport in $Na_3Fe_{0.1}Mn_{0.2}Co_{0.2}Ni_{0.3}V_{1.2}(PO_4)_2F_3$@CNTs Cathode for Sodium-Ion Batteries, *Adv. Sci.*, 2025, **12**, e07806.

158 P. Kumari, A. Kumar, H. Lohani, A. Ahuja, A. Sengupta and S. Mitra, Impact of Composite Cathode Architecture Engineering on the Performance of All-Solid-State Sodium Batteries, *ACS Appl. Mater. Interfaces*, 2025, **17**(21), 30793–30805.

159 H. Hu, X. Lin, S. Tong, T. Wang, P. Wang, Z. Zhou, X. Yan, M. Jia, Y. Niu and X. Zhang, Revisiting the honeycomb-ordered Ni-Sb layered oxides and unraveling the pivotal role of Jahn-Teller effect towards robust structure sodium-ion batteries, *Energy Storage Mater.*, 2025, **79**, 104319.

160 J. Fan, J. Cao, J. Liu, M. Xu and Y. Niu, Role of tin doping in $Na_4VMn(PO_4)_3$ for sodium-ion batteries, *Energy Storage Mater.*, 2025, **78**, 104245.

161 Y. Jiang, R. Wang, P. Xiong, Y. Liu, H. Li, L. Zhang, Y. You and C. Zhang, A solid dual-salt plastic crystal electrolyte enabling rapid ion transfer and stable interphases for high-performance solid-state sodium ion batteries, *Chem. Sci.*, 2026, DOI: 10.1039/D5SC09186A.

162 E. Wang, C. Xu, M. Chen, W. Hua, X. Liu, Y. Liu, Z. Wu, Y. Xiao, W. Yang, X. Guo and W. Chen, Superstructure Engineering Enables NASICON-Type Phosphate Cathodes with Increased Working Voltage and Energy Density, *Adv. Mater.*, 2025, **37**, e12435.